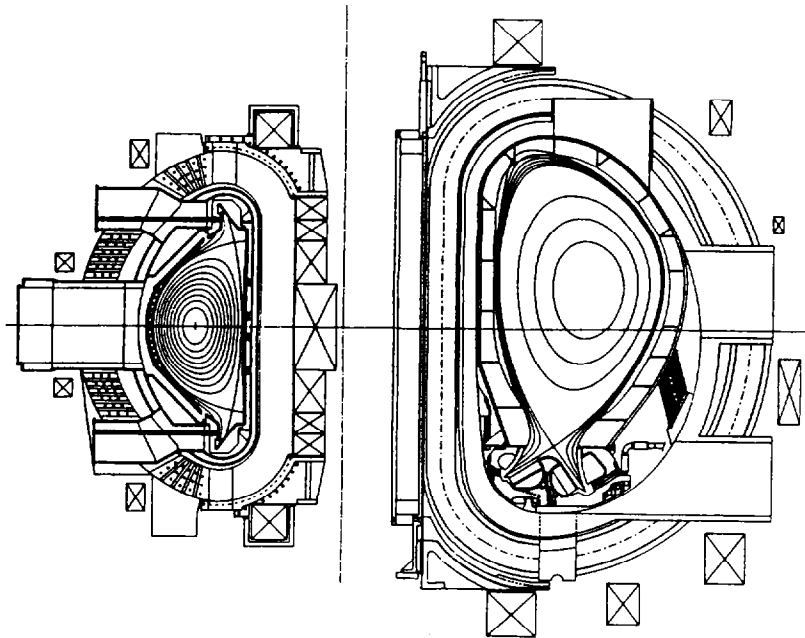


Technical and Cost Assessment of the PCAST Machine

Final Report



PCAST

ITER

Volume I

Introduction

Chapter 1.0 Physics Basis

prepared by
PCAST Study Group
December, 1995

91-951208-MIT/DBMontgomery-01

Technical and Cost Assessment of the PCAST Machine

Final Report

Volume I

Introduction

Chapter 1.0 — Physics Basis

Chapter 2.0 — Trade Studies

Contents

<u>Section</u>	<u>Title</u>	<u>Author(s)</u>	<u>Page</u>
	Introduction	J. A. Schmidt	1
1.0	Physics Basis		
	Physics Design Overview	G. H. Neilson, R. Goldston	7
1.2.1	ITER Physics Guidelines and Basis	N. Uckan	36
1.2.2	Steady-State Ignition and High-Q Scenarios	W. Nevins	41
1.2.3.a	Neutral Beam Injection	C. C. Tsai, D. Mikkelsen	57
1.2.3.b	Ion Cyclotron Heating System	D. W. Swain, D. B. Batchelor, M. D. Carter	66
1.2.4	Plasma Shaping Experimental Basis	E. Lazarus	84
1.2.5.a	Poloidal Field System Design	R. Bulmer	89
1.2.5.b	Fast Position Control	C. Kessel	101
1.2.5.c	Plasma Initiation	P. W. Wang	104
1.2.5.d	Reference Discharge Simulation	C. Kessel	109
1.2.6	Divertors and First Wall	D. Hill	125
1.2.7	Physics Basis: Diagnostics	K. Young	137
2.0	Trade Studies	W. Reiersen, J. Galambos	148
2.1	Comparison of the ITER and PCAST Devices	W. Reiersen, J. Galambos	148
2.2	Sensitivity Studies Around the "Optimized" PCAST Design Point	W. Reiersen, J. Galambos	154
2.3	Conclusions	W. Reiersen, J. Galambos	162
Appendix A	Supercode Physics and Engineering Rules and Cost Scalings	W. Reiersen, J. Galambos	164

INTRODUCTION

The Office of Fusion Energy requested that a three month study be undertaken to explore the recommendations made by PCAST for a reduced scope ITER mission. The PCAST suggested that a device with a mission of ignition for moderate burn time could address the physics of burning plasmas at lesser cost than the present ITER mission. If such a machine were to have a substantially reduced cost relative to ITER, PCAST reasoned that full partnership by the US might be feasible under present flat budget projections.

The ground rules established for the study included the use of "ITER Physics" and the desire to scale costs from "ITER estimates" when ever possible.

The study was chartered to develop a design to meet the reduced mission and compare its construction cost with ITER. In addition the study explored the cost and performance sensitivity to variations in design approach and physics performance. To better understand the cost of such a project in US terms, the design example was also to be estimated in a Total Project Cost format.

It is traditional to approach a study of this nature by performing trade-off studies using a systems code approach, and to select an optimized baseline design based on these results. The time limitation for this study, however, required that a parallel approach be taken in which a "design example" was chosen at the start, allowing more detailed engineering and costing to proceed in parallel with the systems code work. The systems code results could then

be used to illustrate the performance and cost sensitivity to perturbations around the chosen example. These perturbations include optimization of the design point (for example, changes in aspect ratio or TF/CS envelope trade-offs), changes in burn time, and changes in the choice of cost scaling factors.

The study has been carried out by a team drawn from MIT, PPPL, ORNL, LLNL, and GA, and has been funded at the 2.5 Professional Man Year level. The study is documented as a stand alone Executive Summary, and as a detailed report.

Mission

The Scientific Mission of the PCAST Machine is to explore the physics of ignition and burn control in a DT tokamak plasma on shorter time scales than those for ITER, and therefore represents a sub-set of the ITER mission. The more limited mission omits any requirements for nuclear fluence, and the engineering qualification of prototypical reactor subsystems, for example, the superconducting magnets.

We have taken a goal of a 120 second burn time for our design example, on the basis that it provides sufficient time to explore burn dynamics where helium accumulation and exhaust are critical issues. We recognize that substantially longer burn times would be required to reach equilibrated burn conditions, or to fully explore performance optimization by current profile control, but find such a requirement incompatible with the spirit of the reduced cost targets sought by PCAST.

Machine

The parameters for the 5.0 meter major radius design example selected are listed in Table 1, together with ITER parameters.

Table 1. Design Example	ITER	PCAST 5
Toroidal Field (T)	5.7	7.0
Elongation (k95)	1.6	1.75
Triangularity (delta95)	0.24	0.45
Plasma Current (MA)	21.0	15.3
Major Radius (m)	8.14	5.00
Minor Radius (m)	2.8	1.5
Fusion Power (MW)	1,500	400
Beta Normal (%-m-T/MA)	2.3	1.5
Fraction of Greenwald Limit	1.6	0.8
Helium confinement time	51	44
Tau-skin [Mikkelsen,91] (sec)	323	105
Installed Auxiliary Power (MW)	100	60
Number of Pulses	12,000 *	5,000

* Basic Performance Phase

The machine configuration chosen for the design example is shown in **Figure 1**, and is compared with ITER in **Figure 2**. All coils use copper conductors cooled to cryogenic temperature. The TF coils are cased, and are bucked against the Central Solenoid. The basic support structures are patterned after ITER, with upper and lower crowns and intercoil structures between the outer legs supporting the out-of-plane loads.

The PCAST Machine utilizes stronger shaping than the ITER machine to increase the plasma current capacity at a 5.0 meter radius. The value chosen would still be considered relatively moderate, and as it lies within the existing database, we considered it to meet the spirit of "ITER Physics" rules. In our initial scoping studies, we noted that shaping offered the highest potential for reduction in machine size of any of the variables studied.

We recognized that strong shaping can have a negative impact on the cost of out-of-plane structures, design requirements for the central solenoid and control power (and cryogenic refrigeration in the case of superconducting coils.) We believe, however, that certain aspects of the PCAST Machine make it less vulnerable to these negatives. We have found, for example, that the radial build of the tokamak core configured to meet the PCAST burn time of 120 seconds leads to a copper TF magnet that can accommodate more out-of-plane loads than a configuration that meets the ITER superconducting TF requirements. In addition the reduced neutron fluence of the PCAST device relative to ITER leaves available the option of installing control coils inside the vacuum vessel to control highly shaped plasmas. The vacuum vessel is also fitted closely to the plasma on the outboard side, providing the passive stabilization needed to control the vertical instability.

The plasma configuration utilizes a double null divertor, with a “long vee” shape similar to ITER. Projected heat loads are in the range of 4-6 MW/m², requiring no special heat reduction techniques in the divertor.

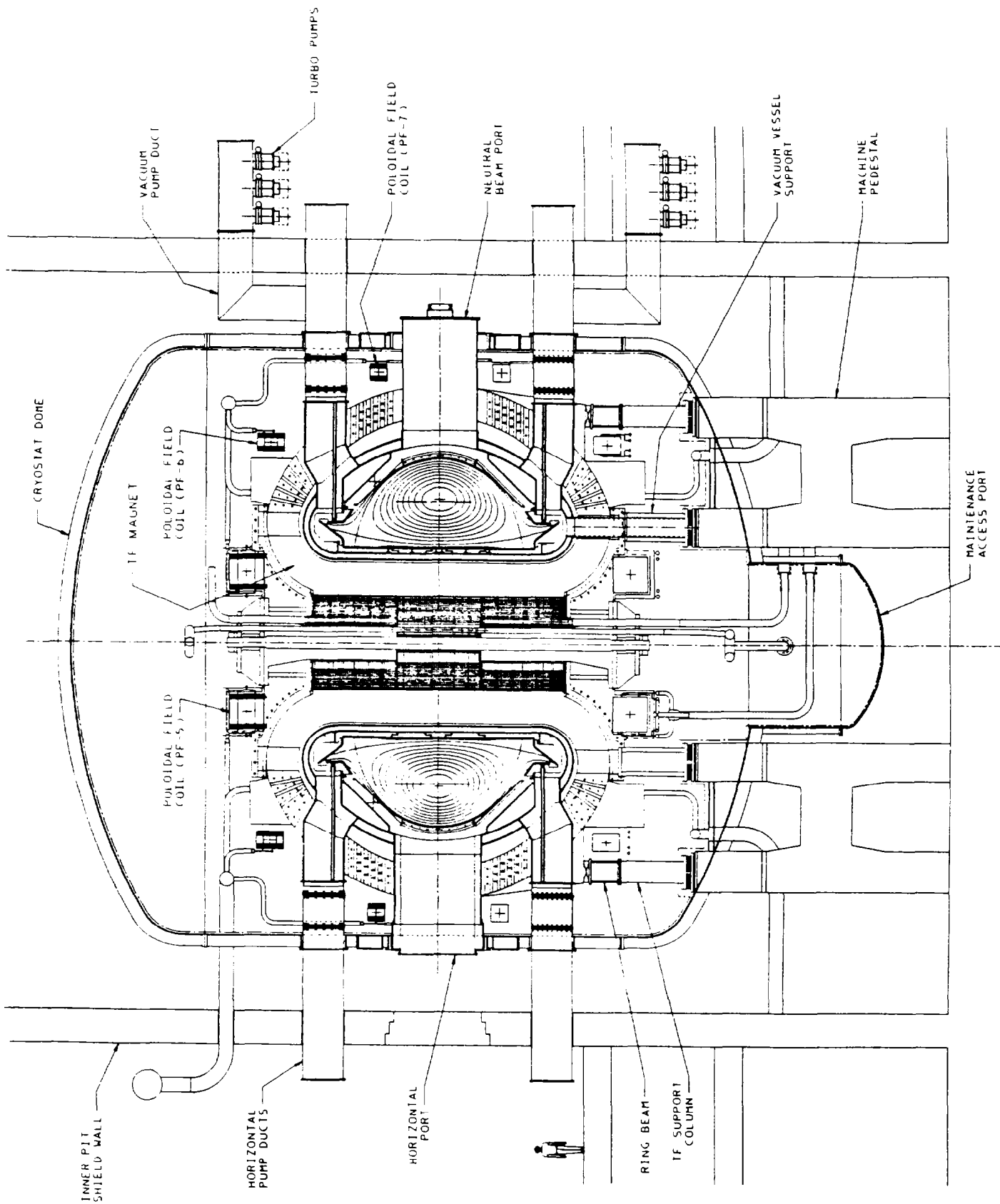
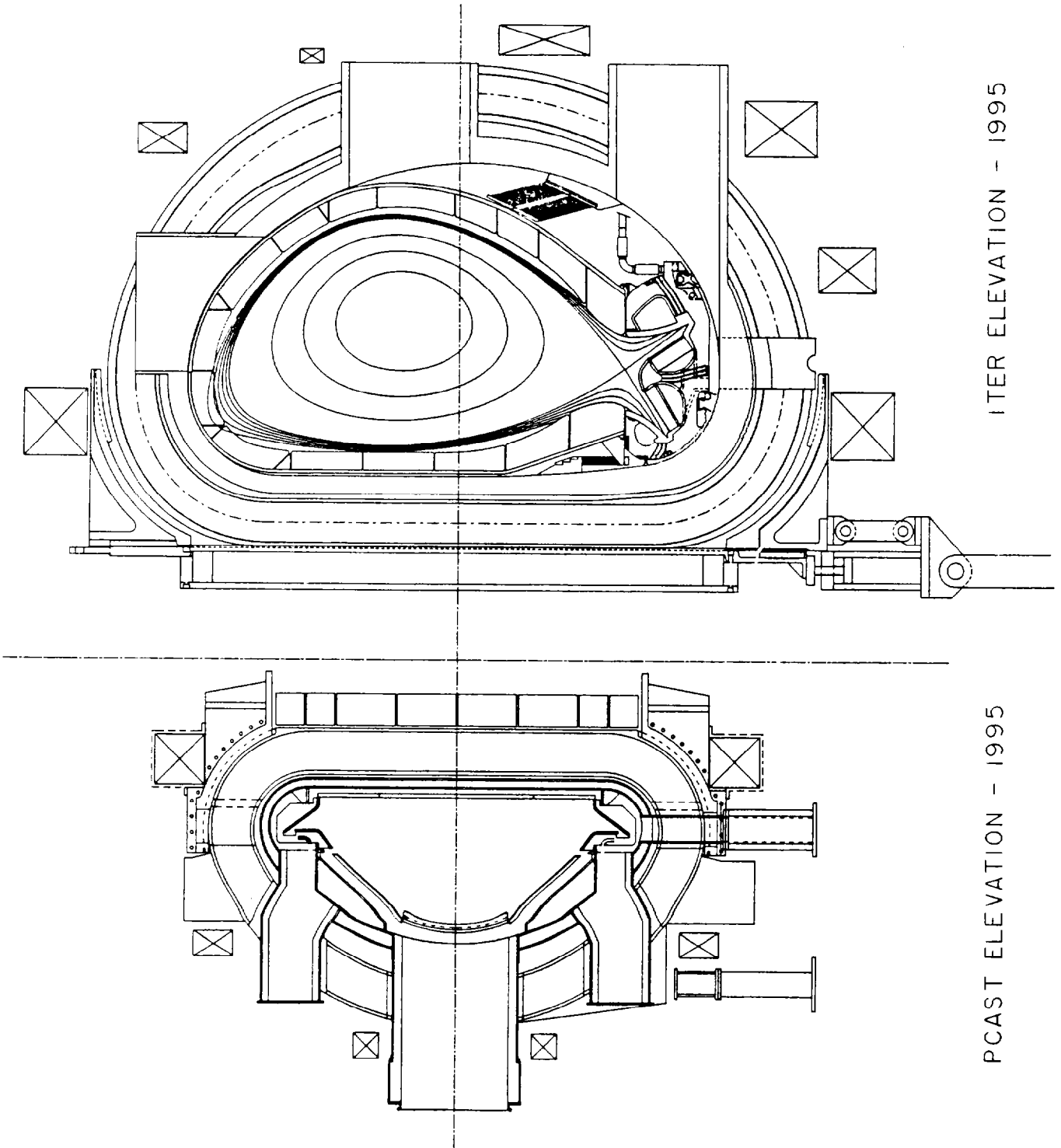


Figure 1. PCAST Device Elevation View



ITER ELEVATION - 1995

PCAST ELEVATION - 1995

Figure 2

1.1. Physics Design Overview

G. H. Neilson (ORNL) and R. J. Goldston (PPPL)

The design of the PCAST machine has been developed using the ITER design as a starting point, then making design changes consistent with the reduced PCAST mission. The ITER physics guidelines serve as the basis for the PCAST machine physics requirements. A range of design choices is available within the framework of these guidelines and, wherever possible, we have chosen in such a way as to minimize the cost while preserving full mission capability. The requirements, physics guidelines, and resulting design choices are described in this section. Detailed physics analysis supporting certain critical design aspects are presented in the next section.

1.1.1. Machine Size Considerations

The selection of the main tokamak parameters (size, magnetic field strength, and fusion power) is the critical decision affecting the cost and fusion performance of a burning-plasma machine. The main differences between the PCAST and ITER missions are 1) the reduction in pulse length for burning-plasma studies from $\sim 1,000$ s to ~ 100 s and 2) the deletion of the nuclear testing mission, which eliminates the requirements for high instantaneous neutron wall load (1 MW/m^2 in ITER) and lifetime fluence ($\sim 0.2 \text{ MW-yr/m}^2$ for ITER's Basic Performance Phase alone). It is important to understand the logic of how this narrowing of the ITER mission translates to a smaller machine.

Shortening the pulse length makes copper magnets a viable option. Because copper magnets are more tolerant of nuclear heating than superconductors, the inboard shield thickness can be significantly reduced to only that required to ensure survival of the magnet insulators at a reduced lifetime fluence level ($\sim 0.015 \text{ MW-yr/m}^2$, more than an order of

magnitude less than ITER's). In ITER the distance between the inner leg of the toroidal field coil and the plasma is 1.37 m, while the same distance in the PCAST machine is only 0.65 m. Most of this 0.72-m difference is due to the elimination of the blanket and a reduction in the shield thickness that results from the change in the mission and reduction in fluence. In the PCAST machine the aspect ratio is slightly higher ($R_0/a=3.3$ vs. 2.9) than in ITER, as is the toroidal field at the coil (12.3 T vs. 11.6 T). These differences combine with the reduced coil-plasma spacing to increase the toroidal field on axis from 5.7 T in ITER to 7.0 T in the PCAST machine.

For the PCAST design we have adopted a more strongly shaped plasma cross section, namely $(\kappa_{95}, \delta_{95}) = (1.75, 0.45)$, than ITER's (1.6, 0.24), although it is more weakly shaped than the ITER CDA design (2.0, 0.4). Strong plasma shaping is often adopted in tokamak design to increase beta limits or facilitate advanced-tokamak operation; however these were not direct considerations in the PCAST design, where the objective was simply to minimize the size of the machine at fixed ignition margin.

While the choice of shape is not restricted by ITER physics guidelines, it is linked to engineering design choices for the magnets, control coils, and divertors. With the PCAST shape, the central solenoid must be segmented into several independently-powered coils in order to supply the required equilibrium field pattern. This results in strong out-of-plane loads on the toroidal field coils. To meet the burn time goal of 120 s, the PCAST tokamak core includes a thick cross-section, copper toroidal field (TF) coil that can accommodate greater out-of-plane loads than the ITER superconducting TF coil design. In addition the reduced neutron fluence of the PCAST device relative to ITER leaves available the option of installing control coils inside the vacuum vessel to provide fast position control (both radial and vertical) of highly shaped plasmas. (In a reactor such coils would be placed behind the blanket, if not the shield.) The vacuum vessel is also fitted closely to the plasma

on the outboard side, providing the passive stabilization needed to control the vertical instability. A double-null divertor configuration is used to reduce the heat and particle loads on the short inner divertor leg associated with high triangularity. These features are incorporated in the engineering design of the PCAST machine.

The relaxation of power-density requirements in the PCAST mission and the properties of the H-mode confinement scaling (Section 1.2.1) allow the ignition figure-of-merit $I_p A$ to be reduced. For traditional confinement scalings (in which τ_E exhibits a $P^{-1/2}$ dependence), the ignition margin scales roughly as $M_{ig} \propto (I_p A)^2$, with no dependence on fusion power density. Under ITER's H-mode scaling (in which τ_E decreases more strongly with power, namely $\propto P^{-2/3}$), the ignition margin scaling becomes approximately $M_{ig} \sim (I_p A)^2 \left(\frac{R_0^2 B_T^2 n \kappa}{P} \right)^{1/3}$. Reductions in wall loading ($\sim P/R_0^2$) and increases in toroidal field, density, and elongation make it possible to match ITER's ignition margin with a factor 0.84 reduction in $I_p A$.

The impact of strong shaping, reduced shield thickness, and reduced fusion power on machine size can be clearly seen. The major machine parameters are related through the safety factor (q_{95}), which is kept fixed at 3.0, the ITER design limit. Using the ITER formula for q_{95} , this relationship can be expressed as:

$$q_{95} = \frac{5 B_T R_0}{I_p A} S = 3 \quad (1)$$

Here, we use a shape parameter S which is the product of two factors, one (S_ϵ) which depends on the inverse aspect ratio ϵ ($\equiv A^{-1}$) and another ($S_{\kappa\delta}$) that depends on plasma cross section shape, described by its elongation (κ_{95}) and triangularity (δ_{95}):

$$\begin{aligned}
S &= S_\epsilon S_{\kappa\delta} \\
S_\epsilon &= \frac{\epsilon(1.17 - 0.65\epsilon)}{(1 - \epsilon^2)^2} \\
S_{\kappa\delta} &= \frac{1 + \kappa_{95}^2(1 + 2\delta_{95}^2 - 1.2\delta_{95}^3)}{2}
\end{aligned} \tag{2}$$

The significance of S as an experimental performance indicator and the validity of q_{95} and S as design variables are discussed in Section 1.2.4. Combining (1) and (2) at constant q_{95} , we see that the machine size scales as:

$$R_0 \sim \frac{I_p A}{B_T S_\epsilon S_{\kappa\delta}} \tag{3}$$

The stronger shape adopted for the PCAST design increases $S_{\kappa\delta}$ by a factor 1.30 over the present ITER (Figure 1a.), and thus contributes to a factor 0.77 reduction in R_0 at fixed B_0 . Within the constraints of ITER physics guidelines, plasma cross section shaping offers significant potential for reducing the machine size, a topic that is further investigated in the trade studies (Section 2.0).

The reduction in blanket/shield thickness creates a gap in the radial build that can be used to improve the performance of other components. The optimum use of this space must take several factors into consideration; such optimization is addressed in Section 2.0. For the illustrative design, the change in aspect ratio from 2.9 to 3.3 reduces S_ϵ by a factor 0.84 (Fig. 1b.), while the toroidal field on axis increases by a factor 1.23, and the required $I_p A$ decreases by a factor 0.84. These effects combine through Eq. (3) to produce a factor $0.81 = \left(\frac{0.84}{1.23 \times 0.84} \right)$ reduction in R_0 .

In summary, the PCAST mission permits the ITER design to be changed in ways that allow significant reductions in its size. We have used simple arguments here to show that, for the same safety factor and ignition margin as ITER, the major radius can be reduced by about 40%, from 8.1 m to 5.0 m. This conclusion has been confirmed by the detailed engineering and physics analyses supporting the PCAST illustrative design, and by system code analyses that find an optimum design point very close to that of the illustrative design.

1.1.2. Major Parameters and Plasma Configuration

The design point for the PCAST machine was chosen to provide the same ignition margin as ITER based on ITER physics guidelines. Requirements determined only by the engineering-test aspects of the ITER mission, such as the neutron fluence, fusion power, and pulse length, were relaxed as much as possible in order to reduce the cost.

The machine and reference operating parameters for the PCAST illustrative design are listed in Table 1, along with corresponding parameters for ITER. A fixed-profile model based on the ITER physics guidelines (Section 1.2.1) was used to analyze plasma performance. The fusion power is calculated by integrating an accurate expression for the DT fusion reaction rate over the plasma profiles. The reference operating point for the PCAST machine is that which produces the specified fusion power (400 MW) at the minimum value of the ITER93H ELM-free confinement multiplier (C_{93H}) and no auxiliary heating (ignition). The machine is sized so that it ignites with the same value of C_{93H} (0.77), the same value of edge safety factor (3.0), and the same H-mode profile shape assumptions ($\alpha_T=1.0$, $\alpha_n=0.1$) as ITER. An impurity concentration $n_{Be}/n_e=0.03$ is assumed in evaluating both machines. (In actuality the PCAST machine design assumes carbon first walls, while ITER uses a combination of beryllium, carbon, and tungsten. Materials choices are likely to evolve in either case.) The global helium particle confinement time τ_{He}^* is assumed to be equal to $10\tau_E$, in accordance with ITER guidelines. This

determines the helium concentration n_{He}/n_e , which is calculated to be about the same (0.10) in both machines. In this manner, the PCAST machine is designed for the same ignition margin as ITER based on a common set of assumptions. Next we consider the differences.

As discussed in the previous subsection, the PCAST machine has a higher toroidal field on axis, a higher aspect ratio, and a more strongly shaped plasma cross section than ITER. These changes were made in an effort to reduce the machine size. Possibilities for further design optimization are addressed in the section on trade studies. Those studies show that the illustrative design point is close to the optimum one.

The PCAST pulse length is determined by burning-plasma physics and control considerations, rather than fluence requirements. The governing time scale is that for helium accumulation, since the transport of helium ash out of the core plasma and its exhaust through the divertor system are critical physics issues for fusion reactors. Optimizing the startup trajectory as ash accumulates and maintaining an operating point with an equilibrated ash concentration are critical issues for burn control. A burn time of 120 s (approximately $3\tau_{\text{He}}^* = 30\tau_E$) was adopted as a design goal for the PCAST machine. This provides enough time for a well-controlled transition from an ohmically heated state to an ignited state followed by a period of steady-state burn, as discussed in Section 1.2.5.d. The pulse length is about one skin time (~ 100 s); longer pulse lengths for current-profile control experiments would be possible at reduced field.

While the two machines have the same ignition margin by design, they differ in terms of their margins with respect to other physics operating limits. We consider these next. An operating margin, as defined by ITER, should be greater than unity.

Beta. The ITER guidelines specify the beta limit as $\beta_N \leq 2.5$ [see Table 1 for definitions and units]. The beta margin M_β , defined as $2.5/\beta_N$, is about 1.1 in ITER and 1.6 in PCAST.

L-H Transition. Adequate power must be provided for transition from L to H-mode. The transition to the H-mode in the double-null PCAST machine could be made in an unbalanced single-null configuration, in order to minimize the required power. The scaling of the transition power has recently been re-evaluated by the ITER Confinement Modeling and Databases Expert Group. Enough data are now available to permit a free fit to the transition database, giving $P_{L-H} = 1.7(n_{20})^{0.81} B_T^{0.66} R_0^{1.19} a^{0.87} \kappa^{0.46}$. Under this scaling the power required for transition to the H-mode at a density of $5 \times 10^{19} \text{ m}^{-3}$ is 26 MW, well below the auxiliary power capability of 60 MW, giving a fairly comfortable margin $P_{\text{aux}}/P_{L-H} = 2.31$. For ITER this margin is 1.39. If the earlier “ASDEX” scaling is used, the PCAST device has a margin of only 1.0, while that of ITER is 0.70. The margin for either machine can be improved by considering that there is likely to be a favorable scaling with species (as there is from H to D) and that some fusion power is to be anticipated in even in low density L-mode.

H-L Transition. The ITER guidelines require that the power loss across the separatrix P_{sep} be high enough to prevent H-to-L-mode back-transitions. The power threshold for such transitions is rather uncertain, but is currently assumed to be about one-half the L-to-H transition threshold at the operating point, i.e. $P_{H-L} = 0.5 \times P_{L-H}$. Since ASDEX-Upgrade experimental data indicate that the reverse transition power is insensitive to the direction of the grad-B drift, we anticipate that this same formula will hold in the double-null configuration. Under the free-fit scaling the margin for H-L transitions in the PCAST device, defined as $(P_\alpha - P_{\text{bremss}})/P_{H-L}$, is 1.57, while the margin for ITER is 2.51. If we instead used the “ASDEX” scaling, this margin would be 1.06 for ITER but only 0.54 for the PCAST reference operating point.

While the new, more reliable, scaling indicates that PCAST has the required margin, we have investigated alternate scenarios within the operating space of the PCAST machine which increase the margin to unity under the older scaling in Section 1.2.2. There are various solutions available; one example is to operate in a driven mode ($Q=40$) with ~10 MW of auxiliary heating power. To ensure that the PCAST machine can accommodate such operating points, the internal hardware is specified to handle 100 MW of thermal losses (80 MW of alpha, plus 20 MW of auxiliary heating).

Density. First we consider the empirically-based upper limit for high-confinement H-mode operation, the “Greenwald” limit $[n_{20}] < I_p / \pi a^2$. The H-mode database indicates that most H-mode tokamaks can operate successfully at densities close to this limit, but have exceeded it in the H-mode only by the use of deeply penetrating pellet injection. The “Greenwald margin” (ratio of the Greenwald limit to $[n_{20}]$) is 0.6 in ITER and 1.3 in PCAST. The demonstration of reliable H-mode operation at densities well above the Greenwald limit has therefore been identified as a high-priority physics research and development need for ITER.

The ITER guidelines specify another upper density limit, namely the theoretically-predicted Borass limit, which depends on the average power density across the separatrix, the plasma configuration, the ratio $n_{sep}/\langle n \rangle$, and other parameters. Assuming $n_{sep}/\langle n \rangle = 0.4$ and 50% divertor radiation, then the “Borass margin” (ratio of the Borass limit to n_{sep}) would be ~1.3 in ITER and ~1.0 in PCAST. Small adjustments in the operating density or edge profile could be made, if necessary, to provide a margin greater than unity if desired.

Divertor power handling. The power-handling situations in ITER and PCAST are quite different. A figure of merit which characterizes divertor operating conditions is the ratio

P_{loss}/R_0 , which is 26 MW/m for ITER's reference ignited single-null divertor scenario and only 11 MW/m for PCAST's double-null scenario. For comparison, a typical value for DIII-D is 12 MW/m. To handle its heat loads, ITER relies on significant extrapolations in divertor physics performance from present experiments. Advanced operating scenarios must be developed for ITER (and also for power reactors) to disperse the heat loads and still be compatible with the desired core conditions and pumping. The ITER Physics guidelines specify radiative or dynamic gas target divertor operation to detach from the divertor targets and reduce the peak heat fluxes on divertor structures to 5 MW/m². The PCAST machine, on the other hand, has about the same peak target heat flux (~6 MW/m² is predicted), but operates in an attached, high-recycling divertor mode typical of present machines. Little or no extrapolation in divertor physics performance is required in the PCAST machine as a prerequisite for studying burning plasmas. Nonetheless, it is designed to be able to continue the needed physics research and development in this area. The PCAST machine has a long-vee divertor shape similar to ITER's (with about the same ratio of poloidal length to minor radius), is equipped with gas injectors to control divertor conditions, and can be modified to test different configurations or materials during the experimental phase. The accurate and flexible shape control of the PCAST device should permit precise positioning and control of the divertor channel.

Toroidal Field Ripple. ITER guidelines specify limits on the toroidal field ripple of 2% at the outer edge of the plasma and 0.1% in the center. The PCAST device satisfies these requirements with 1.8% at the edge and 0.1% in the center.

1.1.3. Reference Operating Scenario

The PCAST machine operates in a pulsed mode, with the plasma current inductively driven by the poloidal field system throughout the pulse.¹ Here we describe an idealized operating scenario used to determine design requirements for the magnet, power, heating, and fueling systems. Detailed simulations are discussed in Sections 1.2.5.c and 1.2.5.d.

Initial magnetic field conditions are established by first raising the toroidal magnetic field to its design value, a process that takes about two minutes. As the toroidal field (TF) approaches flattop, the poloidal field (PF) coil currents are energized, reaching an initial bias condition just as the TF reaches flattop. A poloidal back-bias flux of over 100 webers exists in the bore of the tokamak at this instant, while the transverse fields in the vacuum vessel are very low. The PF currents are then reduced in a predetermined manner, creating a rising toroidal electric field in the plasma region. A breakdown condition is assumed to be satisfied when the loop voltage reaches 15 V and a large transverse field null exists in the vacuum vessel. Thereafter the plasma current (I_p) begins to rise, while the PF currents continue to decay as they inductively raise the plasma current and maintain the plasma in a stable positional equilibrium. When I_p reaches a level of 100-250 kA, the PF coil voltages have decayed to the point where active feedback control of the discharge can be established, marking the end of the initiation phase. Analyses described in Section 1.2.5.c show that the initiation phase lasts about 1 s from the time the PF coils begin to discharge.

As the current is raised, the plasma is simultaneously moved from the outboard edge to the center of the chamber and expanded to an elongated shape, resting on the outer limiters. A diverted condition is attained after about 10-15 seconds and a full current “Start of

¹ Noninductive scenarios could be tested using the planned heating systems or upgrades but do not drive design requirements or cost of the illustrative machine. Such scenarios are discussed in Section 1.2.2.

Flattop” (SOF) condition after about 25 seconds. During this ramp-up phase, the poloidal flux in the transformer passes through zero and reverses direction, almost reaching full forward bias by SOF. Only Ohmic heating is applied during this phase. The plasma current profiles are determined by the I_p ramp-up rate (0.6 MA/s) and current diffusion. The discharge simulations suggest that this phase may need to be extended by 5-10 s in order to increase the internal inductance slightly as q passes through 4, but alternative growth scenarios may also be used to increase l_i , if this proves necessary.

The SOF plasma density is about $0.3 \times 10^{20} \text{ m}^{-3}$, high enough to stop the tangentially-injected 500-keV beam neutrals. Heating power ($\leq 60 \text{ MW}$) and fuel ($\leq 6.1 \times 10^{21} \text{ s}^{-1}$) are then applied in such a manner as to first effect a transition into the H-mode and then raise the plasma temperature and density to a “Start of Burn” (SOB) condition that matches the reference operating point described in Section 1.1.2. In order to avoid an overshoot in fusion power production before the helium ash accumulates to its steady-state value, the density and/or the DT fuel mixture must be increased in a gradual manner to limit the reactivity. The heating phase is assumed to last 15 s ($\sim 3\tau_E$). After SOB, the auxiliary heating is assumed to be turned off, and an ignited burn condition is maintained for the next 120 s. (The capability to maintain 20 MW of auxiliary heating for driven operation is also available). The fueling rate is reduced to that required to balance particle losses due to transport and burnup ($2.1 \times 10^{21} \text{ s}^{-1}$), thereby sustaining the burn point. Poloidal flux is consumed at the low rate (0.1 V assumed) required to sustain the current at ignition temperature. By “End of Burn” (EOB), the transformer is fully forward-biased. In the shutdown phase, the plasma is extinguished in a controlled manner first bringing down the plasma density to reduce the alpha heating and then dropping the plasma current as the toroidal field decays. Preliminary discharge simulation studies (Section 1.2.5.d) support this scenario, although the full range of start-up, shut-down, and burn-control options remains to be explored.

2) three independently-driven pairs of ring coils. Each pair is up-down symmetric about the midplane. The segmentation of the central solenoid is needed to achieve the strong plasma shaping used in the PCAST design, while ITER with its weaker shape can use a monolithic solenoid consisting of a single coil.

The PF system provides over 200 volt-seconds of poloidal flux to meet the inductive initiation and current-drive requirements for the Reference Operating Scenario of Section 1.1.3. It also provides the equilibrium fields necessary to control shape and position within ± 1 cm throughout the pulse. Once the plasma becomes diverted, the major and minor radii are then held at their reference values and the outer strike points (the intersections of the outer separatrix with the divertor target) are held at a controlled location near the divertor gap. Small adjustments in the plasma elongation and triangularity are made as necessary to keep the +3-cm surface within the first wall envelope. The physics design of the PF coils to meet these requirements is discussed in detail in Section 1.2.5.a.

For initial breakdown a loop voltage of 15 V is applied, coincident with the occurrence of a large field null ($|B_{\perp}| \leq 2.5$ mT within a 0.5-m radius circle centered at $R=6$ m). The induced eddy currents in the vacuum vessel are taken into account in establishing the initial bias currents. The PF coil and power supply requirements for plasma initiation are described in Section 1.2.5.c.

Internal coils are used to control the vertical position of the elongated plasma, in conjunction with the vacuum vessel, which acts as a passive stabilizer. The coils are located on the plasma side of the outboard vacuum vessel wall extensions, and behind the first wall. The coils and their power supplies are designed to shift the plasma vertically by 2 cm with minimal excursions and to control a randomly-fluctuating vertical position with 1 cm root-mean-square displacement and a bandwidth ($\Delta\omega$) equal to the growth rate of the

vertical instability. Similar coils are used for fast radial position control, which is advantageous for maintaining a good impedance match with the ICRF wave launchers. They can maintain the plasma radial position in the presence of simulated ELMs characterized by an abrupt 20% loss of plasma stored energy every 0.5 s. The required electrical characteristics for these coils are discussed in Section 1.2.5.b..

1.1.6. Heating System Configuration and Requirements

An auxiliary plasma heating system is provided to heat the plasma to ignition temperatures and to supplement the alpha heating in driven scenarios. The total heating power (60 MW) is sufficient to reach the L-H mode transition threshold at target plasma line-averaged densities up to $0.5 \times 10^{20} \text{ m}^{-3}$. In near-ignition scenarios, the maximum auxiliary heating power is needed only during the heating and fueling phase; it is reduced to 20 MW or less during the burn phase. The heating system is capable of operating for the full pulse length at full power to test the divertor targets at ignition-level heat loads prior to activation of the machine. The arrangement of heating systems (including upgrade provisions) is shown in Fig. 3. We have assumed that the heating configuration will include 30 MW of neutral beam injection (NBI) and 30 MW of ion-cyclotron range-of-frequencies (ICRF) radiofrequency heating. These two technologies should provide the operational flexibility required to optimize startup and burn-control scenarios.

The NBI system includes three 10-MW, 500-keV neutral beams (similar to the JT-60U systems, but modified for longer pulse lengths), injecting tangentially with a tangency radius of 4 m ($R_0 - 2a/3$, as planned for ITER). The combination of two co-injectors and one counter-injector provides a net momentum input for driving toroidal rotation so as to avoid locked modes. The beams are installed on special access ports (Fig. 3) and are arranged to avoid impingement on sensitive internal structures. A fourth beam (counter-injected) can be readily accommodated as an upgrade, and its trajectory is included in

Fig. 3. Neutral beam coupling issues and a description of the system design are presented in Section 1.2.3.a.

The ICRF system includes two adjacent multi-strap wave launchers, each coupling 15 MW of RF power to the plasma in the ~60-110 MHz frequency range. Two or more discrete operating frequencies would be available in this range to provide options for ion and electron heating and operation over a range of toroidal field strengths. A third port is available to accommodate a third RF launcher identical to the first two. The ICRF physics design and system design are discussed in Section 1.2.3.b.

Many heating upgrade or reconfiguration options are available if the needs of the experimental program should change. The availability of additional port capacity has already been noted. The neutral beams could be upgraded to deliver ~40% more power by installing a plasma neutralizer (which would have to be developed). The ICRF launcher rating could be increased if reliable operation at higher RF voltages proves feasible. Other types of RF launchers could be substituted in order to change to different operational scenarios (e.g., current-drive) or frequency ranges (e.g., lower hybrid or electron cyclotron). Advanced-tokamak operating scenarios that use current profile control to improve plasma performance can be tested at extended pulse length (at reduced fields) as described in Section 1.2.2. The heating system upgrades to meet the requirements of these scenarios can be accommodated.

1.1.7. Fueling Requirements and Tritium Inventory

Plasma fueling will be supplied by means of gas, neutral-beam, and pellet injection. Gas injectors capable of injecting H, D, and impurity gases will be installed in the main plasma region and the divertor region. They will be used to prefill the chamber prior to initiation, to control the density profile in the edge plasma and scrapeoff channel, and to

control divertor conditions. Deuterium and impurity injection in the divertor will be needed to optimize scenarios for exhausting energy and momentum and controlling impurities.

At the reference operating point, the core electron inventory is about 6×10^{22} . To supply these particles in the 15 s allotted for the heating/fueling phase would require a core fueling rate of about 4×10^{21} atoms/s. At full power, the neutral beams would nominally supply only 4×10^{20} atoms/s of DT fuel (assuming 30 MW of neutrals, all injected at 500 keV), or only ~10% of the fueling requirement. The rest must be supplied by pellet injection. During flattop, the DT burnup rate with 400 MW of fusion power is about 2.8×10^{20} atoms/s. The global particle loss rate is estimated to be 1.8×10^{21} atoms/s, assuming $\tau_p = 2\tau_E$, and $\tau_p^* = 8\tau_E \approx 35$ s (i.e., a global recycling coefficient of 0.75 with active pumping). So the steady fueling requirement to offset both burnup and losses is 2.1×10^{21} atoms/s. (Note that the neutral beam source is not so large as to over-fuel the core, even if it were operated at full power throughout the burn.) The peak fueling rate, which occurs at the end of the fueling phase, is the sum of the density buildup and maintenance rates, 6.1×10^{21} atoms/s.

The PCAST design includes a pellet injector system installed in a radial port and capable of injecting D or T at a rate of 2.1×10^{21} atoms/s throughout the flattop, and at higher rates for short times for initial densification (with additional margin as needed to allow for fueling inefficiencies and wall effects). Shallow fueling is considered adequate for efficient fueling and density profile control, so present-day injector technology (~1 km/s) should suffice. The total fuel injected into the core plasma per pulse is the sum of the initial charge (6×10^{22}) plus maintenance fuel (2.1×10^{21} atoms/s times 120 s) for a total of 3.1×10^{23} atoms.

Since the entire plasma-facing area inside the vacuum vessel is assumed to be covered with carbon-based materials, tritium retention must be considered. Assuming a 50:50 mixture of DT fuel is injected, we would expect to inject a total of 1.6×10^{23} tritons per pulse. Experience on TFTR (which also has nearly complete carbon wall coverage) suggests that an upper bound on the long-term in-vessel tritium retention is about 50%. This includes the effect of routine plasma and wall-conditioning operations similar to what would be experienced in PCAST, except for high-temperature (350 C) bakeout which is available in PCAST but not in TFTR. Thus it is conservative to assume 50% retention, or 0.8×10^{23} tritons (0.4 g or 4,000 Ci) retained per pulse in PCAST.

No site limit for releasable tritium has been established for ITER, but U.S. safety experts have suggested 1 kg as an appropriate goal. For a physics machine with greatly reduced duty factor like the PCAST machine, however, a lower limit might be more reasonable, e.g. 100 g. With such a limit, it would be necessary to undertake special tritium-removal operations (e.g., helium-oxygen discharge cleaning or controlled air exposure) about every 250 pulses (nominally 50 operating days). We conclude that, while the in-vessel tritium retention is enough to require a removal capability, such operations would not have a burdensome impact on the experimental program.

1.1.8. Diagnostic Requirements

The diagnostic requirements for the PCAST machine are essentially the same as ITER's. The overall diagnostic performance requirements are:

- To provide real-time signals needed for machine protection and plasma control.
- To provide data that can be used for optimizing the machine operation for optimum performance.
- To provide data needed for understanding the important physical mechanisms that may limit performance.

The PCAST machine design provides exceptionally good access for diagnostics through numerous large radial ports, both on the midplane and in the divertor regions. Vertical ports would also be provided for cross-sightline access into the divertor. At the same time, the presence of internal structures (e.g., divertors) and shielding cause significant access limitations, in spite of very large ports. Also, the diagnostics must be designed to operate in an environment in which both the instantaneous and time-integrated neutron fluxes are high (3.5×10^{17} n/m²/s and 2.1×10^{23} n/m², respectively, at the plasma surface). This affects the choice of materials and use of shielding. High operating temperatures (up to 1200 C on divertor target surfaces) and conditioning temperatures (350 C bakeout) are important design considerations for many diagnostics. The strategy for successful implementation of the PCAST diagnostics would include two key elements: 1) a design approach that ensures that the diagnostics are well integrated with the design of the tokamak and facility, and 2) an aggressive research and development program on radiation effects on diagnostic components.

The arrangement of diagnostics around the PCAST machine is shown in Figs. 3 and 4. Details of the PCAST diagnostic system are described in Section 1.2.7.

1.1.9. Power and particle handling requirements

Thermal energy losses from the plasma are handled by the plasma-facing components (PFC), which include the divertors, toroidal limiters, and poloidal limiters. The configuration and material requirements for these structures were described briefly in Section 1.1.4. Here we briefly outline their performance requirements. Physics analysis to translate these requirements to detailed loads is presented in Section 1.2.6 and a detailed description of the design is given in Chapter 3.0.

The PFC system is required to handle a total of 100 MW of power for the burn phase of the pulse. This corresponds to a $Q=20$ driven scenario with 80 MW of alpha-particle heating power (400 MW of fusion power), and 20 MW of auxiliary heating power. Heat loads to individual structures are governed by power-balance assumptions that partition the losses among the various loss mechanisms (i.e., radiation and charged-particle flows) and structures (limiters and divertor targets) for a range of conditions.

The main particle handling requirements are to exhaust the helium ash from fusion reactions and the DT fuel lost from the plasma. With 400 MW of fusion power, alpha particles are produced at a rate of $1.4 \times 10^{20} \text{ s}^{-1}$. Helium must be exhausted at this same rate, or $0.5 \text{ Pa}\cdot\text{m}^3\text{s}^{-1}$ (4 torr-l/s). The helium concentration in the core plasma is about 10%. The concentration in the divertor is further reduced by a factor of 0.2, according to ITER Expert Group recommendations, so we expect the DT fuel exhaust rate to be about 50 times the helium exhaust rate, or $\sim 7 \times 10^{21} \text{ s}^{-1}$, or about $12 \text{ Pa}\cdot\text{m}^3\text{s}^{-1}$ (100 torr-l/s) of molecular DT. This is over three times the core fueling rate, providing an ample envelope for gas fueling to control conditions in the SOL and divertor. Assuming a duct entrance pressure of 0.25 Pa (2 mtorr), we require a pumping speed of $50 \text{ m}^3/\text{s}$. This requirement is quite modest compared to the conductance provided by the large PCAST radial pump ducts, and can be satisfied with an inexpensive external pumping system.

The PCAST machine will be routinely bakeable to 350 C to desorb hydrogenic species and impurities from the carbon surfaces. Glow discharge cleaning in He will be employed to condition the walls between shots. As discussed earlier, a tritium removal procedure such as helium-oxygen glow will be available to control in-vessel inventories.

1.1.10. Neutron handling requirements

At 400 MW of fusion power, the PCAST machine produces 14-MeV neutrons at a rate of $1.4 \times 10^{20} \text{ s}^{-1}$, or 320 MW of neutron power. The instantaneous neutron wall load is about 0.8 MW/m^2 , based on a plasma surface area of 400 m^2 . The elimination of nuclear testing from the PCAST mission eliminates ITER's 1 MW/m^2 wall load requirement. The integrated wall load ("fluence") over the life of the machine is 0.015 MW-yr/m^2 ($2.1 \times 10^{23} \text{ n/m}^2$), assuming 5,000 full-power pulses of 120 s duration. This an order of magnitude less fluence than ITER expects (0.2 MW-yr/m^2) in the Basic Performance Phase alone.

Although the PCAST neutron handling requirements are greatly reduced compared to ITER's, they still impact the design in a major way. The most sensitive element is the magnet insulation, so a shield is needed to attenuate the neutron flux enough to ensure the integrity of the insulator for the life of the machine. Most of the instantaneous neutron energy is absorbed by the shield, which is integrated with the vacuum vessel structure, and removed by cooling water during a pulse. However, some heat is deposited in the coils and therefore affects the coil cooling and power supply requirements. Degradation in the performance of carbon plasma-facing components is an issue, but not a severe limitation on the lifetime of such components (Section 3.0/WBS 1.7). The activation of the vacuum vessel and other structures is such that a full remote maintenance capability is required.

1.1.11. Disruption handling requirements

Disruptions are a major structural design driver for the PCAST machine, as for any high-performance tokamak. Following ITER guidelines, we assume that the thermal quench duration could be as short as 1 ms. The typical current quench duration is specified as 25 ms for ITER, with a range of 10-300 ms. The TPX project assumed a time-varying current-decay rate such that the peak decay rate was about twice the time-averaged rate,

based on clear evidence from the DIII-D experimental data base. For the PCAST machine, we combine the ITER guidelines with the TPX refinements, for an average decay rate of 1 MA/ms (15 ms decay time) and a peak decay rate of 2 MA/ms. A decay time shorter than ITER's is appropriate based on the smaller machine size; decay times in Alcator C-Mod ($a=0.23$ m) are as short as 1 ms. However, the exact scaling of decay rates with machine dimensions is still uncertain.

Halo currents are assumed to be as high as 40% of the pre-disruption plasma current, according to ITER guidelines, though 20% is regarded as typical. A similar, two-tier specification was adopted for TPX (40% worst-case, 33% typical), with corresponding assumptions on toroidal asymmetry (2:1 worst-case, 1.5:1 typical). For static stresses, the structural design of the plasma-facing components is governed by the worst-case assumptions. Halo currents up to 40% of the pre-disruption plasma current and toroidal peaking factors up to 2:1 have been assumed for the PCAST machine.

These disruption specifications (along with those pertaining to runaway-electron characteristics) strongly impact the design of the plasma-facing components, internal control coils, radiofrequency launch structures, and the vacuum vessel. The extensive analysis of disruption scenarios for the BPX and TPX projects has been used for guidance in sizing these components for the PCAST machine.

1.1.12. Number of pulses

The ITER physics guidelines call for a total ~12,000 pulses for the Basic Performance Phase (BPP). About half of these pulses are for fluence accumulation (for engineering tests) and steady-state explorations, in preparation for the Extended Performance Phase. These needs are not applicable to the mission of the PCAST machine. The PCAST machine is designed for a total of 5,000 *full-performance* pulses with a maximum of 5 such pulses

in an operating day. These affect the design of the magnets and other structures where the allowables are modified by fatigue considerations. They also determine the lifetime neutron yield, which is important for sizing the shield to ensure the integrity of the magnet insulator. The daily requirement determines the size of the cryogenic system. These requirements provide an operating envelope that is sufficient to commission the machine and accomplish the PCAST mission. It is likely that detailed operational plan would trade some of the full-performance pulses for a larger number of reduced-field pulses with pulse lengths both shorter and longer than the reference pulse length, which could be accommodated within the design envelope specified here.

1.1.13. Summary

The PCAST machine offers a very attractive set of capabilities for physics research on burning plasmas. In order to maintain ignition and study burn control in the presence of fuel dilution caused by accumulated helium ash, it has substantial plasma performance. Its pulse length and operating space provide a wide range of ignited and driven modes that can be used to study burn control dynamics. Little or no advancement over present-day divertor operation is required to handle the heat loads associated with the design scenarios; however the machine is well-suited to continue the divertor physics research and development required for power reactors. Flexibility in the heating and divertor systems is available to accommodate the uncertainties in predicting plasma performance and operational limits, or to undertake advanced missions (e.g., the development of steady-state burning-plasma scenarios) that would enhance its contributions to fusion. A new generation of fusion diagnostics would provide an unprecedented set of capabilities for understanding, optimizing, and controlling fusion plasmas.

Table I. ITER Physics Guidelines

Characterization of confinement:

Reference assumption for energy confinement: ELMy H-mode

Particle confinement assumption: ELMy H-mode

Auxiliary power requirement: P_{aux} (aux power) $\geq P_{\text{th}}$ (L-H transition threshold power)

$$\tau_E(\text{required}) = \tau_E(\text{ELMy H-mode}) = 0.85 \times \tau_E(\text{ITER93H ELM-free})$$

$$\sim H_L \times \tau_E(\text{ITER89P})$$

- ELM-free H-mode (ITER93H) scaling:

$$\tau_E^{\text{ITER93H (ELM-free)}} = 0.053 I^{1.06} R^{1.9} a^{-0.11} [n_{20}]^{0.17} B^{0.32} A_i^{0.41} \kappa_x^{0.66} P^{-0.67}$$

- ELMy H-mode scaling:

$$\tau_E(\text{ELMy H-mode}) \sim 0.85 \times \tau_E(\text{ELM free H-mode})$$

- ITER (89P) L-mode power-law scaling (ITER89P):

$$\tau_E^{\text{ITER89P}} = 0.048 I^{0.85} R^{1.2} a^{0.3} [n_{20}]^{0.1} B^{0.2} A_i^{0.5} \kappa^{0.5} P^{-0.5}$$

- Confinement/ignition margin: $M_{\text{ign}} \sim 1.1$ at nominal burn condition
- H-mode threshold power:

$$\text{L-to-H transition: } P_{\text{sep}} (\text{MW}) \geq P_{\text{thr, L-H}} (\text{MW}) = 0.044 [n_{20}] B(\text{T}) AS (\text{m}^2)$$

$$\text{H-to-L transition: } P_{\text{H-L}} \sim 0.5 \times P_{\text{L-H}}$$

MHD stability:

- Beta limit: $\beta_{\text{tot}} = \beta_{\text{th}} + \beta_{f\alpha} + (\beta_{\text{beam}}) \leq \beta_{\text{max}}(\%) = gI/aB = \beta_N (I/aB)$

$$\beta_N = g \leq 2.5 \quad \text{for nominal operation (ignition studies)}$$

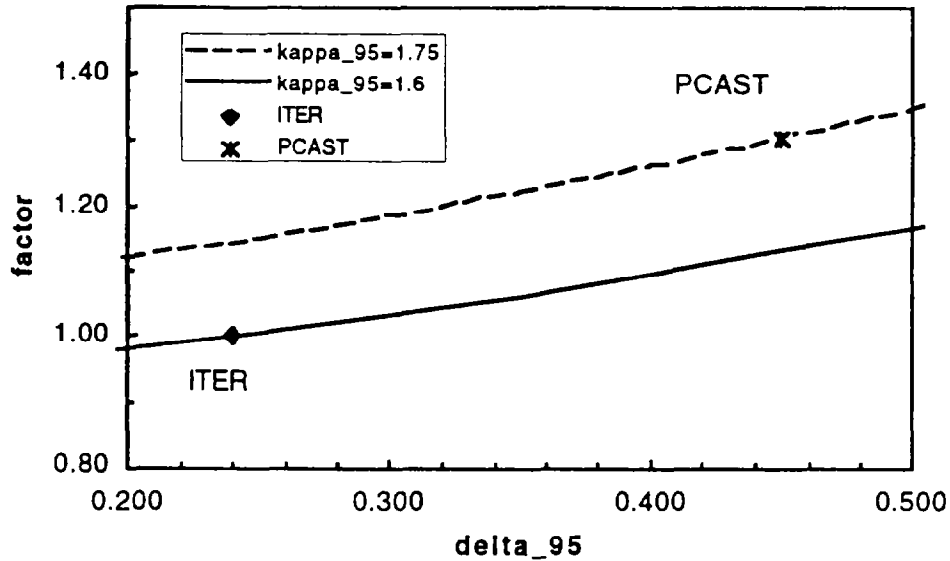
$$\beta_N = g \leq ?? (>2.5?) \quad \text{for advanced scenarios with reversed shear}$$

- Safety factor: $q_{\psi}(95\%) \geq 3.0$
- Rotation and error field: $f_{\text{rot}} \geq 1 \text{ kHz}$, $|B_{2,1}/B_0| \leq 10^{-4}$.

Internal inductance l_i and beta poloidal β_p : PF capability at 21 MA (nominal)

$$0 \leq \beta_p \leq 1.2 [\beta_p = 0.9 (\text{nominal})]; \quad 0.7 \leq l_i(3) \leq 1.1 [l_i(3) = 0.9 (\text{nominal})]$$

a) Cross Section Shape Factor



b) Aspect Ratio Factor

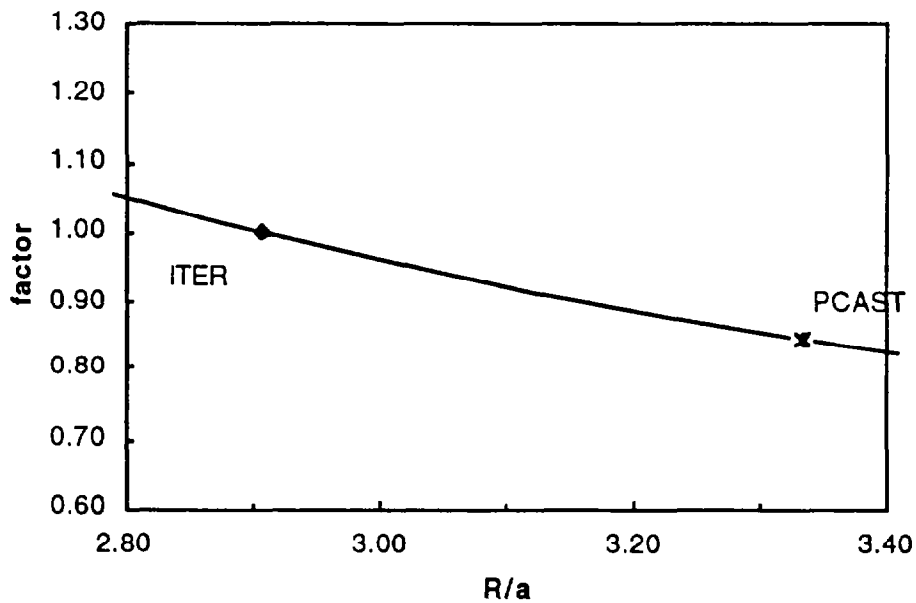


Fig. 1 a)Plot of the Cross Section Shape Factor $S_{\kappa\delta}$ as a function of elongation κ_{95} and triangularity δ_{95} , normalized to the ITER value. The PCAST shape produces a factor 1.30 increase. b)Plot of the Aspect Ratio Factor S_E as a function of aspect ratio R_0/a , normalized to the ITER value. The PCAST design produces a factor 0.84 reduction.

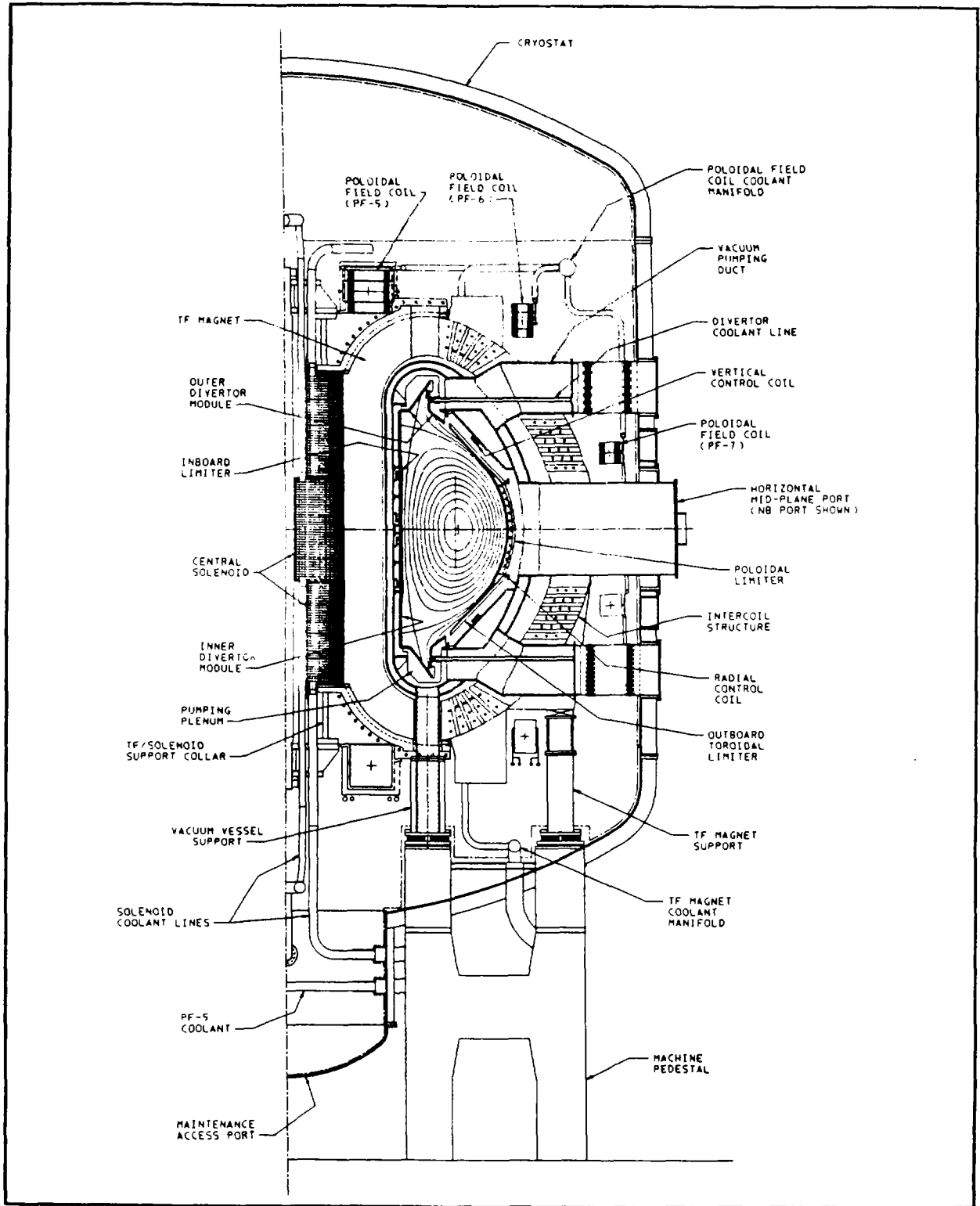


Fig. 2. Elevation drawing of illustrative PCAST machine design showing major elements that affect physics performance.

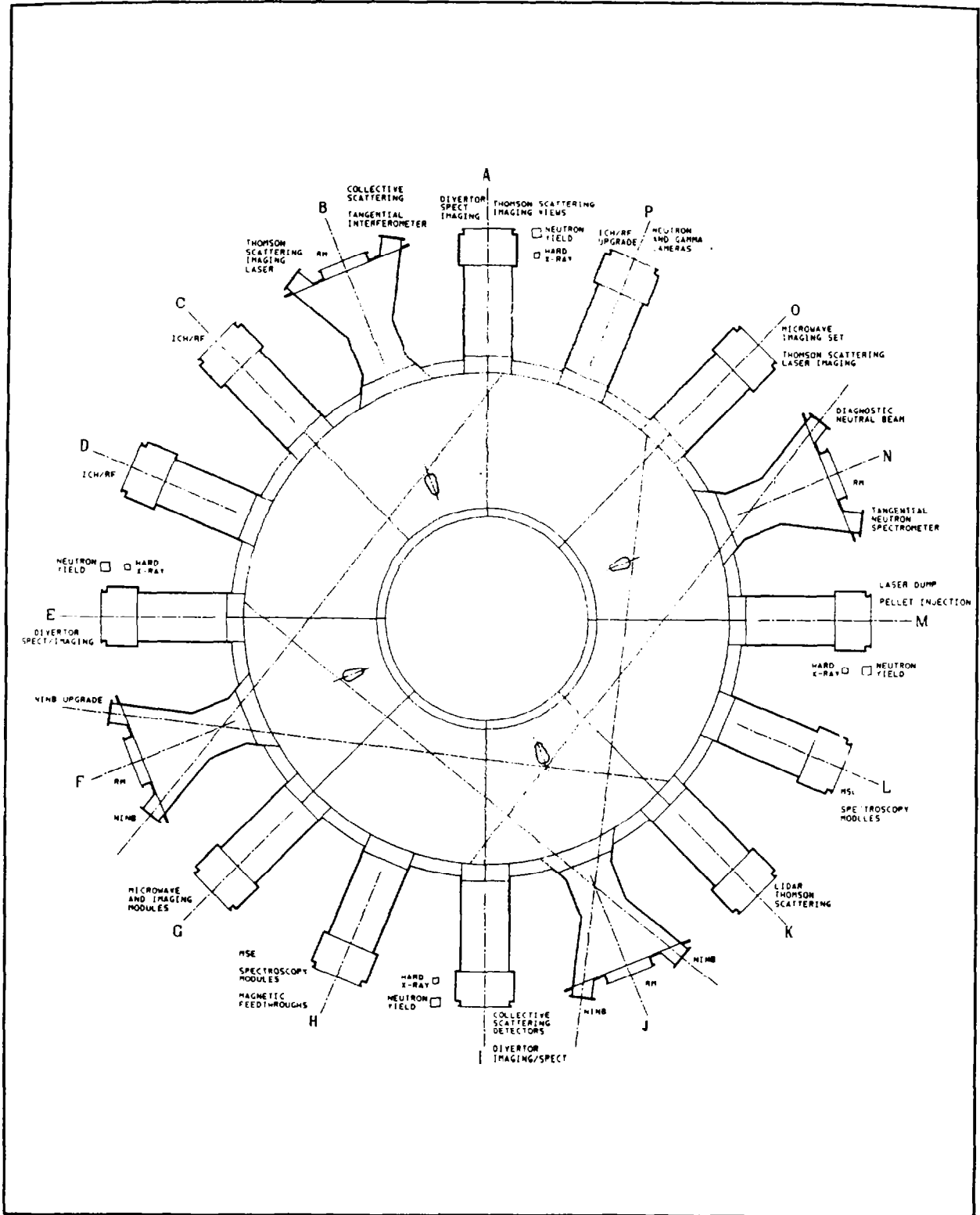


Fig. 3. Plan diagram of illustrative PCAST machine design showing locations of heating (NINB and ICH/RF), fueling (pellet injection) and midplane diagnostics.

1.2.1. ITER Physics Guidelines and Basis

N. A. Uckan (ORNL)

Based on the present understanding and characterization of tokamak experiments and theory, the physics specifications and guidelines for the ITER design have been developed by the ITER Joint Central Team, the Home Teams, and the ITER Physics Expert Groups during the period 1992-1995.

The initial ITER physics design guidelines, covering the period up to 1989, were summarized in Ref. [1] and were updated in Ref. [2] to include the developments in physics understanding at the end of the ITER Conceptual Design Activities (ITER-CDA). This report provides an interim update to these guidelines reflecting the developments during the ITER Engineering Design Activity (EDA).

The physics basis consists of guidelines for energy confinement, operational limits, power and particle control, disruptions, current drive and heating, alpha particle physics, and plasma control. The ITER physics group has worked with the engineering design groups to implement these guidelines. In many cases, the physics issues have not been fully resolved, and a physics R&D program has been developed to complete the physics basis for ITER.

In general, the determination of optimum tokamak parameters involves a complex trade-off between a large number engineering and physics constraints. However, the overall dimensions are set by a relatively simple set of criteria (see Ref. [3]). These criteria derive from the requirements for (i) adequate energy confinement, (ii) sufficient MHD stability and plasma control to avoid frequent disruptions, (iii) adequate shielding to protect the superconducting coils from nuclear heat, and (iv) achieving allowable stresses and superconducting performance in the TF coils:

Physics and engineering issues	Design requirement
– Energy confinement	$I, A = R/a, q_{\psi}$
– MHD stability and plasma control	q_{95}, κ, δ
– Shielding thickness for coil protection	d_{BS} (blanket/shield thickness)
– Coil stress limits/thermal stability margin	$B_{coil} = B_{max}$ at the coil
– Pulse length	R_{bore} (solenoid radius)

From a radial build, the definition of q_{ψ} and aspect ratio $A (= R/a)$, and the $1/R$ fall-off of the field ($B \sim 1/R$), the size of the device is specified by $I, A, q_{95}, \kappa, \delta, d_{BS}$, and B_{coil} . The choice of confinement model, helium concentration, and elongation are the major design drivers. Other quantities are: $q_{95} \geq 3$ for MHD stability, $A \sim 2.5-3.5$ (experimental range), $d_{BS} \sim 1-1.2$ m, $B_{coil} \sim 11-13$ T, $t_{pulse} \geq 1000$ s. The EDA design follow from these considerations and choices for aspect ratio ($A \sim 2.8$), elongation ($\kappa_{95} \sim 1.6$), helium confinement ($\tau_{pHe}^*/\tau_E \sim 10$), and pulse length (≥ 1000 s). For a given mission and design goal, there is sufficient room for design optimization.

The physics guidelines that have been adopted for the ITER design are summarized in Table I. Units are mks, MA, MW, with $n_{20} = \langle n_e/10^{20} \text{ m}^{-3} \rangle$, and $T_{10} = \langle T/10 \text{ keV} \rangle_n =$ density-weighted average temperature ($T_e \approx T_i \approx T$). H-mode profiles: $n, T \sim (1 - r^2/a^2)^{\alpha}$; with $\alpha_n \approx 0.1, \alpha_T \approx 1.0$.

Table I. ITER Physics Guidelines

Characterization of confinement:

Reference assumption for energy confinement: ELMy H-mode

Particle confinement assumption: ELMy H-mode

Auxiliary power requirement: P_{aux} (aux power) $\geq P_{\text{th}}$ (L-H transition threshold power)

$$\tau_E(\text{required}) = \tau_E(\text{ELMy H-mode}) = 0.85 \times \tau_E(\text{ITER93H ELM-free})$$

$$\sim H_L \times \tau_E(\text{ITER89P})$$

- ELM-free H-mode (ITER93H) scaling:

$$\tau_E^{\text{ITER93H (ELM-free)}} = 0.053 I^{1.06} R^{1.9} a^{-0.11} [n_{20}]^{0.17} B^{0.32} A_i^{0.41} \kappa_x^{0.66} P^{-0.67}$$

- ELMy H-mode scaling:

$$\tau_E(\text{ELMy H-mode}) \sim 0.85 \times \tau_E(\text{ELM free H-mode})$$

- ITER (89P) L-mode power-law scaling (ITER89P):

$$\tau_E^{\text{ITER89P}} = 0.048 I^{0.85} R^{1.2} a^{0.3} [n_{20}]^{0.1} B^{0.2} A_i^{0.5} \kappa^{0.5} P^{-0.5}$$

- Confinement/ignition margin: $M_{\text{ign}} \sim 1.1$ at nominal burn condition
- H-mode threshold power:

$$\text{L-to-H transition: } P_{\text{sep}} (\text{MW}) \geq P_{\text{thr, L-H}} (\text{MW}) = 0.044 [n_{20}] B(\text{T}) AS (\text{m}^2)$$

$$\text{H-to-L transition: } P_{\text{H-L}} \sim 0.5 \times P_{\text{L-H}}$$

MHD stability:

- Beta limit: $\beta_{\text{tot}} = \beta_{\text{th}} + \beta_{f\alpha} + (\beta_{\text{beam}}) \leq \beta_{\text{max}}(\%) = gI/aB = \beta_N (I/aB)$

$$\beta_N = g \leq 2.5 \quad \text{for nominal operation (ignition studies)}$$

$$\beta_N = g \leq ?? (>2.5?) \quad \text{for advanced scenarios with reversed shear}$$

- Safety factor: $q_{\psi}(95\%) \geq 3.0$
- Rotation and error field: $f_{\text{rot}} \geq 1 \text{ kHz}$, $|B_{2,1}/B_0| \leq 10^{-4}$.

Internal inductance l_i and beta poloidal β_p : PF capability at 21 MA (nominal)

$$0 \leq \beta_p \leq 1.2 [\beta_p = 0.9 (\text{nominal})]; \quad 0.7 \leq l_i(3) \leq 1.1 [l_i(3) = 0.9 (\text{nominal})]$$

Plasma disturbances: $\Delta\beta_p \leq 0.2$, $\Delta I_i(3) \leq 0.1$; time scale ≤ 1 s

Position/configuration control: Separatrix control ± 5 cm; I_p control ± 0.05 MA [or $\pm 1\%$]

Disruption characteristics:

Thermal quench time: 1 ms [up to 10 ms]

Current quench time: 25 ms [range: 10–300 ms]

Halo (poloidal) current: $I_{\text{halo}}/I_p \sim 20\%$ (typical) [–40% max]; halo width/a ~ 0.2 –0.4

Runaway electrons $E \sim 10$ MeV, total energy ~ 30 MJ, energy flux ≤ 5 MJ/m².

Fueling and exhaust: a combination of gas puffing and pellet injection (shallow penetration)

Power and particle control: SN poloidal divertor with active pumping located at the bottom.

Physics concept: radiative divertor or dynamic gas target divertor

Detached divertor operation with $P_{\text{div}} \leq 5$ MW/m².

Plasma purity — impurity and thermal alpha fractions:

Low-Z (Be, C) PFC; 15 cm separatrix/PFC clearance

Reference basis for estimating He concentration: $n_{\text{He}}/n_e \propto f(\tau^* p_{\text{He}}/\tau_E = 10)$.

Reference basis for secondary impurity content: $n_{\text{Be}}/n_e = 2\%$.

Toroidal field ripple: $\delta B/B \leq 2\%$ at separatrix; $\leq 0.1\%$ in central part of plasma ($r < 1.5$ m)

Auxiliary power — heating and current drive:

$P_{\text{aux}} \sim 100$ MW (NB and RF) for $t_{\text{pulse}} \sim 10^3$ – 10^4 s

Startup EC system: $f_{\text{EC}} \sim 90$ –140 GHz; $P_{\text{EC}} \sim$ few MW

Neutral beam: $E_{\text{NB}} \sim 400$ –1000 keV; $P_{\text{NB}} \sim 50$ MW, $R_{\text{tan}} \sim 6.2$ m

EC H&CD: $f_{\text{EC}} \sim 170$ GHz (on-axis heating), ~ 250 GHz (off-axis CD); $P_{\text{EC}} \sim 50$ MW

IC fast wave: $f_{\text{IC}} \sim 40$ –90 MHz; $P_{\text{IC}} \sim 50$ MW

CD figure of merit $\gamma = \langle n_{20} \rangle I_{\text{CD}} R / P_{\text{CD}}$; $I_{\text{bs}}/I_{\text{total}} \sim 15$ –30%

Density Limit

- **High-density limit** imposes an upper limit on the plasma edge density. A tentative characterization of the Borrass density limit adapted for a single-null divertor configuration of ITER-EDA takes a form

$$n_{20} = (n_{20}/n_{e,s20}) C [Q_{\perp}^{5/8} B^{5/16} (1 - f_{\text{rad}}^{\text{div}})^{11/16} / (q_{\psi} R)^{1/16}]$$

where $n_{e,s20}$ = upstream plasma density at the separatrix, Q_{\perp} (MW/m²) = mean power flux crossing the separatrix, $q_{\psi} = q_{\psi}(95\%)$, $C = 2.37$, and $f_{\text{rad}}^{\text{div}} = P_{\text{rad}}^{\text{div}} / (4\pi^2 R a \kappa^{0.5} Q_{\perp})$ = divertor impurity radiative fraction. The power is assumed to be evenly distributed between outboard and inboard divertor channels. The value of $n_{e,s}/n_e$ (~ 0.4–0.7) depends on particle transport and fueling at the plasma periphery and is not well defined.

— For a comparison, Greenwald density limit is:

$$n_{20}^{\text{GR}} = \kappa J(\text{MA/m}^2) = I(\text{MA}) / (\pi a^2) \text{ line-averaged density } (10^{20} \text{ m}^{-3})$$

- **Low-density limit** defines the heating power required to get the H-mode. This limit is also disruptive and is associated with the error-field induced instability.

References

- [1] *ITER Physics Design Guidelines: 1989* [N.A. Uckan, IAEA/ITER Documentation Series, No.10, Feb. 1990].
- [2] *ITER Design Information Document: Physics* [N.A. Uckan, ITER-TN-PH-0-5, Nov. 1990].
- [3] D. Post and N. Uckan, *Fusion Technology*, Vol. **21**, 1427 (1992)].

1.2.2. Steady-State Ignition and High-Q Scenarios

W.M. Nevins (LLNL)

In this section we examine possible ignited and high-Q driven scenarios in the PCAST machine. The reference design point and operating points are shown in Table I of Section 1.1. As discussed there, the key issues affecting the choice of the reference operating point are:

1. Achieving ignited operation under the same confinement assumptions as ITER—that is, with an energy confinement time that is 0.77 times the ITER93H ELM-free confinement scaling, and a worst-case impurity mix of $n_{\text{B}}/n_e=3\%$ together with a helium concentration governed by the assumption that $\tau_{\text{He}}^*=10\tau_E$;
2. Operation below the β -limit—that is, with $\beta_N \leq 2.5$
3. Operation below the density limit
4. Achieving L–H transitions
5. Avoiding H–L back-transitions.

The PCAST machine is able to satisfy all of these constraints with margins similar to, or greater than the ITER Interim design in ignited, or high-Q driven operation.

Power Balance in Ignited Operation

We may visualize the operating space of the PCAST machine at full current ($I_p=15.3$ MA) and with H-mode density and temperature profiles ($\alpha_n=0.1$ and $\alpha_T=1.0$) by plotting the “ignition curve”—that is, the locus of points where the ohmic and alpha heating power balances the radiated and conducted loss—versus the operating parameters volume-

averaged density, $\langle n_e \rangle$, and density-weighted volume-averaged temperature, $\langle T_e \rangle_n$, as shown by the solid curve in Fig. 1.

PCAST Machine Ignition Curve

$$(I_p = 15.3 \text{ MA}, \tau_{He}^* / \tau_E = 10)$$

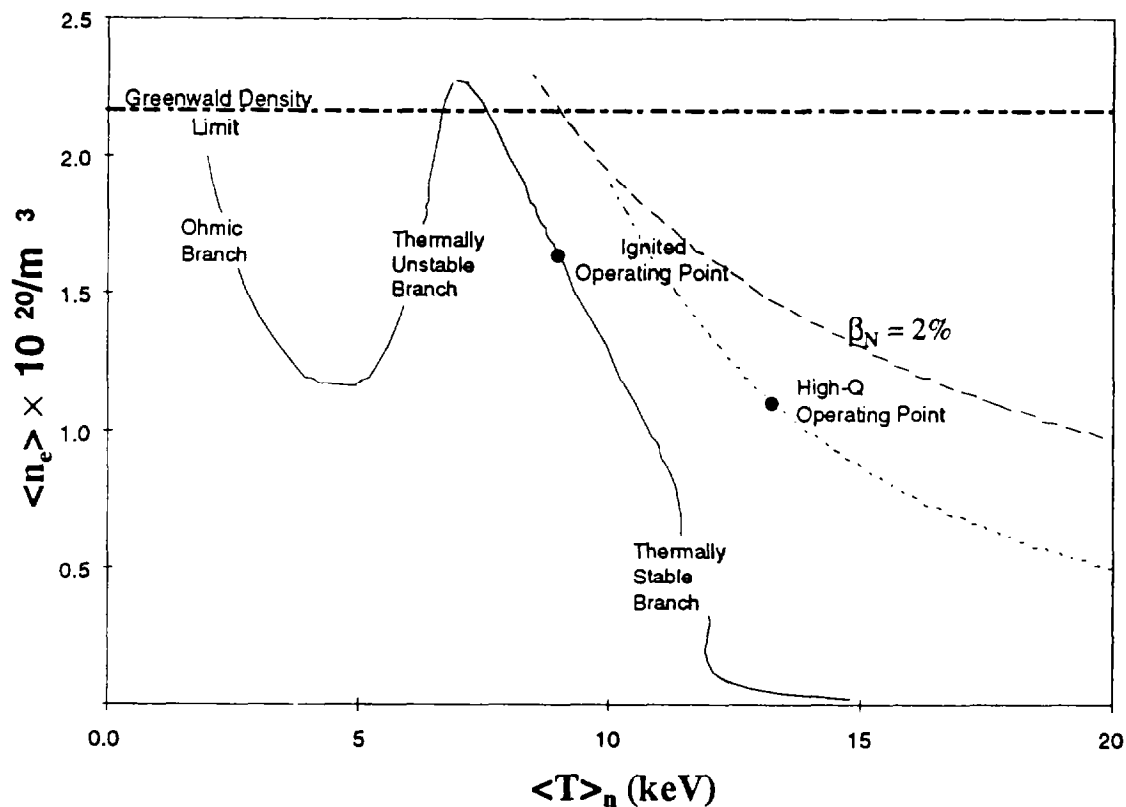


Figure 1. Plasma operational contour (POPCON) diagram depicting the operating space of the reference PCAST machine at full field. The solid curve is the ignition contour ($P_{aux}=0$). The short dashed curve (- - - -) is the marginal H-L driven contour, as defined in this section. The Greenwald density limit and $\beta_N=2$ limit are clearly labeled as operating boundaries.

In computing this ignition curve we employed formulae for estimating the fusion power due to Uckan et al. [1] Numerical integration over the plasma volume shows that this formula is accurate to within about 5% for the thermally stable ignited operating points shown in Fig. 1.

The ignition curve for the PCAST machine differs from that of the ITER Interim Design in that the Ohmic branch rolls over and meets the thermally unstable branch of the ignition curve at $\langle n_e \rangle \approx 1.2 \times 10^{20}/\text{m}^3$ and $\langle T_e \rangle_n \approx 5$ keV for PCAST, while the Ohmic and ignited branches of the $P_{\text{aux}} = 0$ curve are separated by the Cordey pass in ITER. These branches merge for PCAST operation because the sum of the alpha heating and loss power exceeds the total loss power at the Cordey pass. Hence, while auxiliary heating power will be required to achieve an L-to-H-mode transition, auxiliary heating is not required to maintain power balance once H-mode confinement has been achieved in PCAST.

The ITER93H ELM-free scaling degrades with heating power as $P^{-0.67}$ — faster than previous confinement scalings which generally varied with heating power as $P^{-0.5}$. As a result, the thermally unstable and the thermally stable branches of the PCAST ignition curve meet at $\langle n_e \rangle \approx 2.3 \times 10^{20}/\text{m}^3$ and $\langle T_e \rangle \approx 7$ keV, and power balance cannot be achieved in ignited operation at higher densities. In this situation, operation on the thermally unstable branch of the ignition curve is unattractive—either because the fusion power is low ($P_{\text{fusion}} \leq 200$ MW for densities $\langle n_e \rangle \leq 1.6 \times 10^{20}/\text{m}^3$), or because the separation in $\langle T_e \rangle_n$ is small (the thermally stable and unstable branches are separated by less than 3 keV for $\langle n_e \rangle \geq 1.6 \times 10^{20}/\text{m}^3$). Hence, we will not consider operation on the thermally unstable branch further, instead focusing on operating points on the thermally stable branch of the ignition curve. This eliminates any requirement for active control to maintain operation at a thermally unstable operating point (“burn-control”). Operating point control on the PCAST machine can be achieved through intervention over time scales longer than the energy confinement time; for example, by controlling the fuel injection rate as is presently envisioned in the ITER design

The reference operating point in Fig. 1 differs slightly from that discussed in Section 1.1 due to small differences in the numerical models. At a density of $1.63 \times 10^{20}/\text{m}^3$ we find a somewhat higher temperature ($\langle T_e \rangle \approx 9.0$ keV, vs. 8.6 keV for

the model employed in Sect. 1.1) and a somewhat higher fusion power (431 MW vs. 400 MW). The fusion power increases with increasing density on the thermally stable branch of the ignition curve. The fusion power limit of 400 MW is reached at $\langle n_e \rangle \approx 1.6 \times 10^{20}/\text{m}^3$. Lower power operating points can be achieved at lower density with the fusion power going to zero as $\langle n_e \rangle$ approaches zero.

The β -limit

The PCAST machine has substantially more margin in β than ITER. The dashed curve in Fig. 1 shows the locus of points for which the thermal, volume-averaged β equals $0.02 \times I_p/aB_o$ (with I_p measured in MA, a in meters, and B_o in Tesla). For comparison, we note that the ITER guidelines specify a β -limit of $0.025 \times I_p/aB_o$. In addition to the thermal beta, we must also consider the fast alpha pressure. The pressure of the fast alpha particles, $\langle \beta_\alpha \rangle$, is 0.14% ($0.001 \times I_p/aB_o$) at the reference operating point, compared to a thermal beta of 2.17%. The fast alpha beta, $\langle \beta_\alpha \rangle$, decreases with decreasing density, dropping to 0.06% at $\langle n_e \rangle = 0.5 \times 10^{20}/\text{m}^3$ (corresponding to a fusion power of about 50 MW). We conclude that, for the relatively high densities and low temperatures envisioned for PCAST operation, the fast alpha pressure does not significantly increase the volume-averaged beta. Even when the fast alpha pressure is included, all of the ignited operating points fall well below the rather conservative β -limit shown in Fig. 1, $\langle \beta \rangle \leq 0.02 \times I_p/aB_o$.

The Density Limit

Much concern has been recently expressed regarding the tendency of ITER operating points to exceed the Greenwald density limit, $\langle n_e \rangle \leq I_p/\pi a^2$, where I_p is in MA, a is in meters, and $\langle n_e \rangle$ is measured in units of $10^{20}/\text{m}^3$. This limit is shown by the combination of long and short dashes (— - — - —) in Fig. 1. All of the ignited operating points considered for the PCAST machine fall substantially below the Greenwald

density limit. The PCAST reference design point avoids the Greenwald limit due to its higher magnetic field and stronger shaping relative to the ITER design point.

We have also investigated PCAST operating points relative to the power-dependent Borrass density limit [2], a theoretically predicted limit on the density at the plasma edge (which we denote n_{ex}). The precise form of this limit depends on the plasma configuration, differing between single and double null discharges, and on details of the atomic physics near the divertor target. This latter issue has been addressed either through approximate analytic solutions [cf., Borrass (1991)], or by fitting to numerical solutions [Uckan, et al. (1991)].

We first consider the numerical fit to the density limit for the ITER CDA design, which featured a double null configuration with aggressive shaping similar to the present PCAST reference design point. This fit to numerical results, generated in collaboration with Borrass during the ITER CDA, is given by

$$n_{ex,CDA} \leq 1.8 (P_{net}/S)^{0.53} B_o^{0.31} / (q_{95} R_o)^{0.22},$$

where P_{net} is the power conducted across the separatrix, S is the surface area of the plasma, and B_o is the field at the magnetic axis.

Alternatively, we may use the approximate analytic form of the Borrass density limit from [Borrass (1991)],

$$n_{ex,EDA} \leq C_{Borrass} (P_{net}/S)^{5/8} B_o^{5/16} (1-f_{imp})^{11/16} / (q_{95} R_o)^{1/16},$$

where $f_{imp} \approx 0.5$ is the fraction of the exhaust power that is radiated in the divertor. Borrass evaluated the constant $C_{Borrass}$ as 2.37 for the ITER EDA design operating in L-mode. [3] However, three correction factors must be applied for the PCAST design (numerical values for these corrections factors follow recommendations in [Borrass (1991)]).

1. The Borrass density limit is determined by the power exhaust to the inner divertor legs. The exhaust power per unit area across the separatrix is lower on the inboard segment of the separatrix (by about a factor of 3), leading to a downward correction to the density limit of $(0.5)^{5/8} \approx 0.65$.
2. The connection length between the plasma midplane and the divertor is shorter (by about a factor of 2) in double nulls than in single nulls of the same size and general shape, leading to an upward correction of the density limit of $(0.4)^{-1/16} \approx 1.06$.
3. The thermal conductivity in the scrape-off-layer in H-mode is lower than it is in L-mode (by about a factor of 3), leading to an upward correction in the density limit of $(3)^{3/8} \approx 1.51$ (note that this correction factor should be applied for both the PCAST and ITER EDA operating points as both are assumed to be in H-mode).

Combining these factors, we find for the PCAST machine

$$C_{\text{Borrass}} \approx 2.29 .$$

Assuming that the separatrix density is 0.4 times the volume-averaged density, we define the margin of the operating point relative to the CDA version of the Borrass density limit as

$$M_{\text{CDA}} = n_{\text{ex,CDA}} / 0.4 \langle n_e \rangle ,$$

with a corresponding definition for the EDA version (M_{EDA})

The reference operating point of the PCAST machine has a very small margin relative to the Borrass density limit ($M_{\text{CDA}}=1.01$, $M_{\text{EDA}}=1.02$). Fortunately, the Borrass limits closely match the operating density along the thermally stable branch of the PCAST machine's ignition curve shown in Fig. 1. Both versions of the density margin are plotted as functions of density along the thermally stable branch of the ignition curve, in Fig. 2.

Both density limit margins remain near unity, but drop below unity at a density of $0.8 \times 10^{20}/\text{m}^3$ (Borrass EDA margin), corresponding to a fusion power of about 100 MW. Given the inexact nature of these estimates of the density limit, one could still be concerned by the small margin relative to the Borrass density limit at the desired operating point. This margin can be substantially increased in high-Q driven operation as described in connection with H→L-mode transitions in the next section.

Borrass Density Limit Margins on Thermally Stable Branch of Ignition Curve

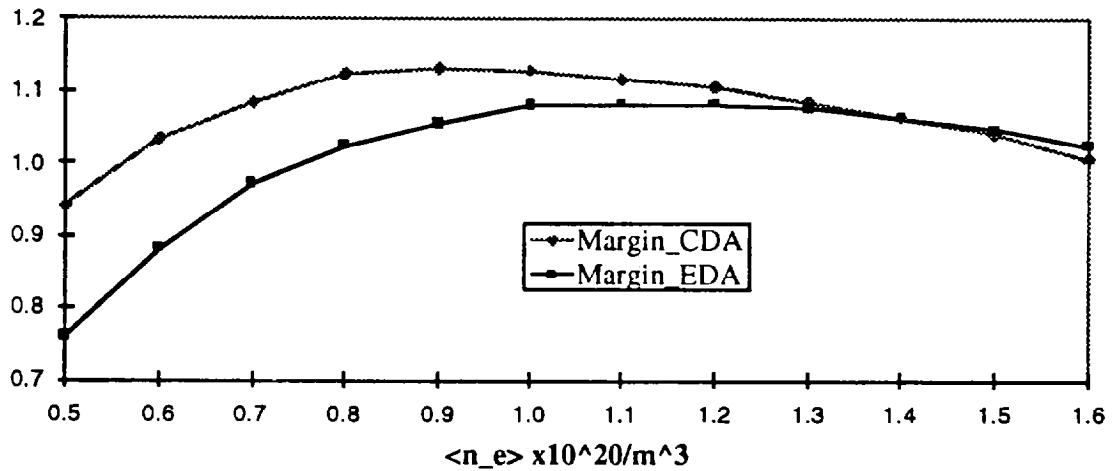


Figure 2. Borrass density-limit margins along the thermally stable branch of the ignition curve.

L → H and H → L Mode Transitions

The ignited operating points projected for both the ITER and PCAST machines assume H-mode like confinement (specifically, an energy confinement time of 0.77 times ITER93H ELM-free energy confinement). The threshold power for the L→H transition is a critical factor in determining the auxiliary heating power on both machines; and the possibility of an H→L transition occurring as the density is increased from its value at the start of the current flat-top (projected as about $0.5 \times 10^{20}/\text{m}^3$ for both the PCAST and ITER devices) toward the desired operating density is a concern in both machines. The PCAST

design has an advantage relative to ITER in this regard in that the installed auxiliary heating power (60 MW) is nearly equal to the alpha heating power at the projected ignited operating point (80 MW), while the installed auxiliary heating power in the ITER design (100 MW) is substantially less than the alpha heating power at ITER's projected ignited operating point (300 MW). Hence, there is relatively more auxiliary power available on the PCAST device to ensure a transition into the H-mode and to avoid H→L transitions in high-Q driven operation. Moreover, the first wall and divertor systems in the PCAST device can accommodate the additional loss power.

The projection of L→H-mode power thresholds from the existing database to ITER and PCAST operation is inexact. The largest uncertainty concerns the scaling of this power threshold with machine size. We consider five possible scaling laws:

1. In its initial analysis, the H-mode Database Working Group [4] proposed an L→H-mode power threshold of the form

$$P_{L\rightarrow H,ASDEX} \approx 0.44 (n_{e,\text{bar}}/10^{20}/\text{m}^3) (S/\text{m}^2) (B/T) \text{ MW},$$

where $n_{e,\text{bar}}$ is the line averaged density. We have characterized this as the ASDEX scaling because much of the initial data came from ASDEX. However, the constant in front reflects more recent additions to the ITER H-mode database.

2. It has been noted that the ASDEX H-mode threshold scaling is not dimensionally consistent with plasma-physics based scaling constraints. If one assumes a linear dependence on $n_{e,\text{bar}}$ and B_o , then such constraints would force the size dependence to go as $R^{2.5}$. The best fit to the present data is then [5]

$$P_{L\rightarrow H,\text{linear}} \approx 0.3 (n_{e,\text{bar}}/10^{20}/\text{m}^3) (B/T) (R_o/\text{m})^{2.5} \text{ MW}.$$

3. Some tokamaks, including both JT-60 and DIII-D report a density dependence that is weaker than linear. This leads to the dimensionally consistent threshold scaling

$$P_{L \rightarrow H, JT-60U} \approx 0.6 (n_{e, \text{bar}} / 10^{20} / \text{m}^3)^{0.75} (B / \text{T}) (R_o / \text{m})^{1.5} (a / \text{m})^{0.5} \text{ MW}$$

4. A dimensionally consistent scaling with a very weak density and size dependence has been proposed by R. Perkins of the ITER Physics Integration Unit,

$$P_{L \rightarrow H, Perkins} \approx 0.012 (n_{e, \text{bar}} / 10^{20} / \text{m}^3)^{0.5} (B / \text{T}) (S / \text{m}^2) (a / \text{m})^{-0.5} \text{ MW.}$$

5. Finally, one can ignore plasma-physics dimensional constraints, and perform a free fit to the database, minimizing the root-mean-square error. This results in the following scaling

$$P_{L \rightarrow H \text{ Free-fit}} \approx 1.7 (n_{e, \text{bar}} / 10^{20} / \text{m}^3)^{0.81} (B / \text{T})^{0.66} (R_o / \text{m})^{1.19} (a / \text{m})^{0.87} (\kappa)^{-0.46} \text{ MW.}$$

Given the wealth of physical phenomena that are known to occur in the edge region of the plasma, and which have the potential to affect the L→H transition threshold, one must be somewhat skeptical of scalings based on dimensional constraints. Given the preliminary quality of the data base, it also seems difficult to justify forcing scalings with particular parameters such as S. Hence, we give most weight to the $P_{L \rightarrow H \text{ Free-fit}}$ estimate of the L→H power threshold, since it provides the best fit to an extensive database, as shown in Fig. 3.

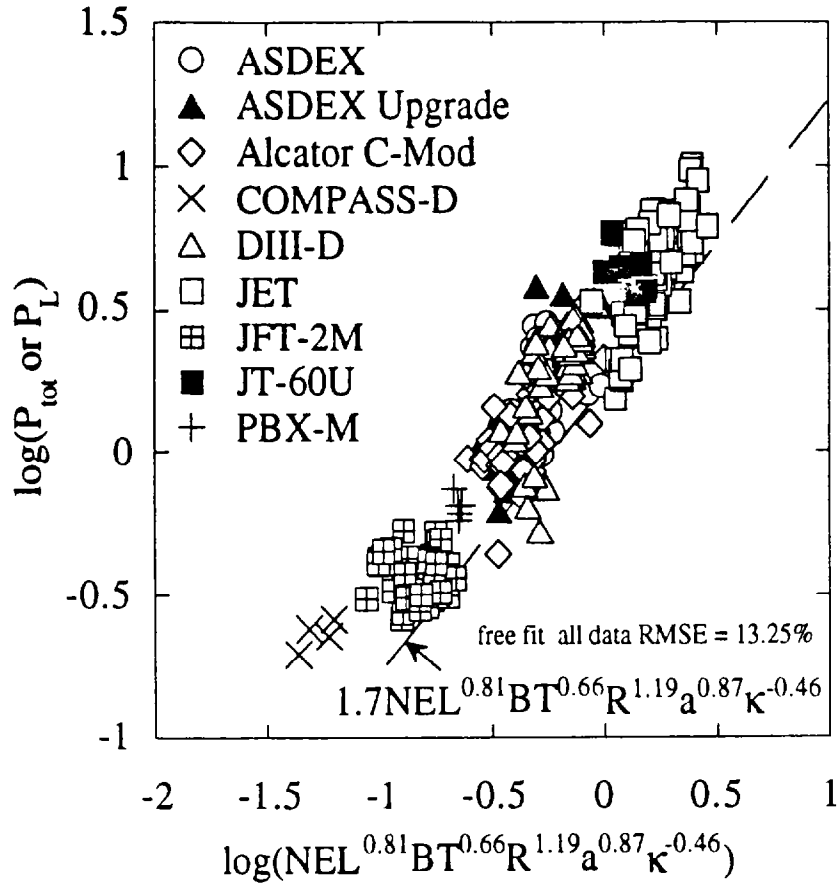


Figure 3. Comparison of experimental L→H-mode power thresholds with the “Free-fit” scaling expression, denoted in this section as $P_{L \rightarrow H}^{\text{Free-fit}}$.

Both PCAST and ITER assume an operational scenario in which auxiliary heating power is applied to a target plasma at a density that is initially well below that of the ignited operating point. The density and alpha-particle heating power then rise simultaneously. The auxiliary heating power must exceed the L→H-mode threshold at the target density to ensure achievement of the L→H-mode transition with high confidence. The installed auxiliary heating power P_{aux} is 100 MW and 60 MW, respectively. We define an L→H-mode transition margin as $M_{L \rightarrow H} \equiv P_{\text{aux}}/P_{L \rightarrow H}$, evaluated at a nominal line-averaged target plasma density of $0.5 \times 10^{20}/\text{m}^3$ for both devices, and tabulate its value for each of the considered scalings in Table I.

Table I. L→H-Mode Transition Margins

	ITER	PCAST
P_{L→H,ASDEX}	142MW	60MW
M_{L→H,ASDEX}	0.7	1.0
P_{L→H,linear}	161MW	60MW
M_{L→H,linear}	0.62	1.0
P_{L→H,JT-60U}	79	34
M_{L→H,JT-60U}	1.27	1.76
P_{L→H,Perkins}	33	19
M_{L→H,Perkins}	3.03	3.16
P_{L→H,Free-fit}	72	26
M_{L→H,Free-fit}	1.39	2.31

We find that the PCAST machine has sufficient auxiliary heating and power-handling capability for transition into the H-mode, based on the most reliable (free-fit) scaling result. Further margin against the "ASDEX" and "Linear" scalings would be afforded by taking into account the anticipated $1/A_i$ scaling of the threshold power, based on hydrogen vs. deuterium results, and allowing for finite fusion power production.

Far less effort has gone into determining the threshold power for H→L-mode back-transitions. Here we follow the ITER JCT in assuming that

$$P_{H\rightarrow L} \approx 0.5 P_{L\rightarrow H} ,$$

and define the margin against H→L-mode transitions as

$$M_{H \rightarrow L} \equiv P_{\text{net}}/P_{H \rightarrow L} .$$

The values of $M_{H \rightarrow L}$ at the reference ignited operating point for both the PCAST and ITER devices are shown in Table II.

Table II. H→L-Mode Transition Margins

	ITER	PCAST
$P_{H \rightarrow L, \text{ASDEX}}$	200 MW	108 MW
$M_{H \rightarrow L, \text{ASDEX}}$	1.05	0.51
$P_{H \rightarrow L, \text{linear}}$	215 MW	100 MW
$M_{H \rightarrow L, \text{linear}}$	0.97	0.55
$P_{H \rightarrow L, \text{JT-60U}}$	83 MW	43 MW
$M_{H \rightarrow L, \text{JT-60U}}$	2.58	1.28
$P_{H \rightarrow L, \text{Perkins}}$	28 MW	19 MW
$M_{H \rightarrow L, \text{Perkins}}$	7.50	2.96
$P_{H \rightarrow L, \text{Free-fit}}$	81 MW	35 MW
$M_{H \rightarrow L, \text{Free-fit}}$	2.58	1.56

We see that both the ITER and PCAST devices have substantial margins against H→L-mode transitions for the JT-60U, Free-fit, and Perkins power threshold scalings. The ITER reference operating point has little or no margin against H→L-mode transitions for the ASDEX and linear power threshold scalings; while the PCAST device has insufficient heating power to sustain H-mode under the ASDEX and linear power threshold scalings.

Both the ASDEX and linear power threshold scalings vary linearly with the density at the operating point. Since the estimates of the H→L-mode threshold power are very similar in both cases (108 MW vs. 100 MW), a high-Q driven operating scenario in which the operating density is lowered (thus lowering $P_{L\rightarrow H}$) while auxiliary heating is applied to increase the ion temperature, the fusion power, and the net heating power (thereby increasing $M_{L\rightarrow H}$) will yield similar results for both ASDEX and linear power threshold scalings. We choose to focus on the ASDEX scaling because this scaling is somewhat more challenging and it has received more attention in the past.

The short dashed curve (- - - -) in Fig. 1 shows the locus of points for which the net exhaust power is exactly equal to $P_{H\rightarrow L,ASDEX}$. The net heating power exceeds $P_{H\rightarrow L,ASDEX}$ for driven operating points above this line. Figure 4 shows the variation of the auxiliary heating power and the fusion power (divided by 10, so that it will be comparable to the auxiliary heating power) at the H→L power threshold (i.e., along the short dashed curve of Fig. 1). We see that modest auxiliary heating is sufficient to achieve driven operation above the ASDEX H→L-mode power threshold in the PCAST device.

Auxiliary and Fusion Power at ASDEX H-L threshold

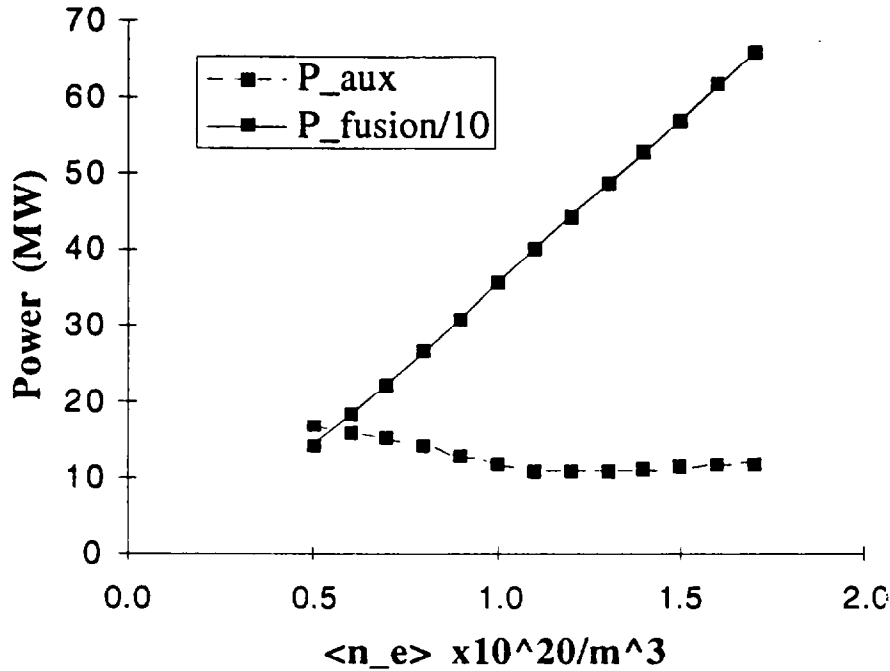


Figure 4. Auxiliary heating and fusion power as functions of density along the marginal H-L curve of the PCAST machine.

In particular, we find a high-Q ($Q \approx 36$) operating point that produces 400 MW of fusion power with 11 MW of auxiliary heating power at a volume averaged density of $\langle n_e \rangle = 1.1 \times 10^{20}/\text{m}^3$, and a temperature of 13.3 keV. We conclude that it should be possible to avoid H→L-mode back-transitions by applying modest amounts of auxiliary power in high-Q operation under all of the H-mode power threshold scalings considered. In particular, there is no difficulty in sustaining the H-mode against the Free-fit scaling, which has the strongest experimental basis. An added benefit in such driven operation is that the margins to the Borrass density limits are greatly increased (to $M_{\text{CDA}}=1.64$ and $M_{\text{EDA}}=1.69$, for the CDA and EDA versions, respectively, of the Borrass density limit).

Advanced Steady-State Operating Modes

An important goal for both the PCAST device and ITER would be to demonstrate steady-state operation at high β_N in which the full plasma current is supported by a combination of the neoclassical bootstrap current and non-inductive current drive. With control over the current profile, it may be possible to operate with the plasma pressure as measured by β_N as high as 6. Such an increase in the plasma pressure that can be confined in a given magnetic field would greatly improve the economic viability of tokamak fusion reactors. Advanced steady state operating scenarios have been developed for ITER. [6] Similar scenarios have also been developed for the PCAST Device. The more aggressive shaping of the PCAST device relative to ITER is an advantage for advanced steady-state operating modes because this increases the magnetic shear at the plasma edge, thereby improving edge ballooning stability and access to regimes of enhanced confinement.

A critical goal for the PCAST device would be to demonstrate the physics basis for an advanced steady-state demonstration reactor. The key physics parameter for reactor improved economics is β_N . Operating modes with β_N up to 6% can be achieved without exceeding the 400 MW fusion power limit in the PCAST device by operation at reduced magnetic field ($B_o \approx 4$ T) and reduced plasma current ($I_p \approx 8$ MA). The resulting plasma discharges have high β_p plasma, which naturally leads to high bootstrap current and more aggressive shaping. Our calculations show that the PCAST poloidal field system can support a plasma with an elongation $\kappa_{95} \approx 1.91$ and triangularity $\delta_{95} \approx 0.66$ at $\beta_p \approx 2.2$. This operating point is summarized in Table 2.

B_o	4 T
I_p	8 MA
R_o	5.0 m
κ_{95}/δ_{95}	1.91/0.66
f_{stab}	1.6
P_{fusion}/P_{aux}	400 MW/20 MW
$\langle n_e \rangle$	$1.0 \times 10^{20}/m^3$
$\langle T_e \rangle$	15 keV
β_N	5.9%
τ_E	2.7 s
$\tau_E/\tau_{ITER93H}$	1.75

References

- [1] N.A. Uckan et al, *ITER Physics Design Guidelines :1989*, ITER Documentation Series No. 10 (IAEA, Vienna, 1990).
- [2] K. Borrass, *Nuclear Fusion* **31**, 1035 (1991).
- [3] K. Borrass, private communication via V. Mukavatov (Feb. 15, 1995).
- [4] F. Ryter for the H-Mode Database Working Group, EPS Meeting, Lisbon, 1993.
- [5] F. Ryter et al, *Nuclear Fusion* (to be published).
- [6] W.M. Nevins et al, "ITER Steady State Operation and Advanced Scenarios", Proc. of the 15th International Conference on Plasma Physics and Controlled Nuclear Fusion Research, Seville, 1994 (IAEA, Vienna, to be published) paper IAEA-CN-60/E-P-5.

1.2.3.a. Neutral Beam Injection

C. C. Tsai (ORNL) and D. Mikkelsen (PPPL)

Requirements

For the reference scenario, the neutral beam injection system injects full power, i.e. all 30 MW of deuterium or tritium beams at 500-keV for 15 seconds to heat the plasma up to "ignition". For the next 120 s of burn, the NBI system would be adjusted to inject neutral beams at $\sim 1/3$ power (10 MW) or less for burn control. The NBI system should be constructed with a capability of full power operation for the entire pulse (135 s). This NBI system can be used for testing the first wall during the pre-DT phase of the program. (This might have to be done at reduced field due to site power limits.)

For fulfilling the above neutral beam injection (NBI) requirements, we plan to use 3 beamlines similar to the JT-60U 500-keV beamlines, which are rated at 10 MW each. [1,2] They are configured as 2 co-injection beamlines and 1 counter-injection beamline, and are to inject tangentially at a radius of $R = 4 \text{ m}$ ($R_0 - 2a/3$). The beam system should have the capability to add a second counter-injection beamline, for a total of four, as an upgrade in case balanced beams are needed. Figure 1 shows a plan view of the test cell including two of the four beamlines installed on special tangential ports; the space allocated for the other two is also seen.

The heating systems must be capable of injecting into an Ohmically heated target plasma whose line-averaged density is $\leq 0.5 \times 10^{20} \text{ m}^{-3}$ in order to reduce the H-mode power threshold. For this density, the calculated beam shine-through power is only 0.2% of the power incident on the plasma

(assuming a deuterium beam, for which the plasma is slightly more transparent than for tritium, and a pessimistic profile). With a density of $0.3 \times 10^{20} \text{ m}^{-3}$, the shinethrough is still only 4%. Assuming a beam cross section of 0.2 m^2 , the incident power density is 50 MW/m^2 and the shinethrough heat load on the opposite wall a manageable 2 MW/m^2 . Thus there is some margin available in the minimum target plasma density, providing some flexibility to lower the H-mode threshold if necessary. At operating density $\langle n_e \rangle = 1.6 \times 10^{20} \text{ m}^{-3}$, the beams are well trapped and the power deposition strongly peaked on axis, as shown in Fig. 2.

System Description

The JT-60U 500-keV N-NBI system is a negative-ion based neutral beam system [1,2]. It is the first high energy negative-ion based neutral beamline in the world. Each beamline is designed to inject 10 MW energetic neutrals for 10 sec beam duration with a duty cycle of 1/60. This beamline uses two 22-A and 500-keV negative-ion sources for injecting 22 MW deuterium ion beams. Assuming 60% neutralization efficiency, 90% transmission efficiency and 2% reionization loss, this beamline should inject 11.6 MW neutrals into the plasmas, to satisfy the 10 MW requirement.

The PCAST neutral beam system is required to provide reliable operation for injecting 135-s neutral beams. The beamline technology being developed for JT-60U and ITER [3-5] should be applicable to the PCAST NBI beam system. In a recent design study of 1-MeV, 1000-s ITER beamline [6,7], the irradiation damage on the insulator column of the ion source has been calculated and evaluated to be acceptable. Furthermore, recent advances in R&D ion sources achieve a high current density of 20-mA/cm^2 at low source

pressures of 0.2 Pa. It is logical to design a compact PCAST NBI beamline with one large ion source (500-keV/44-A) for the convenience of remote maintenance and handling. The beamline system consists of a cesium-seeded volume negative ion source mounted on a source tank with 4 cryopump modules; a neutralizer mounted on a beam tank that houses bending magnet, ion dumps and 4 cryopump modules; and the end tank housing a calorimeter, a drift duct, and gate valves. The other beam equipment are the ion source power supply, a control system and an auxiliary sub-system that includes a cooling water system, a cryogenic refrigeration system, and an auxiliary pumping system, a gas system providing pressurized air, helium, sulfur hexafluoride, and nitrogen, and a tritium recovery system. Table 1 lists the beamline specification of the PCAST NBI system.

The potential technical issues associated with the PCAST NBI system are in the areas of plasma generation, neutronics and tritium, gas flows and pumping, neutralization and stripping, etc. Some of these issues will be resolved by ongoing intensive research and development of NBI injectors for JT-60U and ITER. A few necessary analysis tasks or experimental R&D tasks envisaged are further elaborated below.

Negative Ion Source

The heart of the PCAST NBI system is the negative ion source that needs a demonstration of a reliable long pulse (135 s) production of negative ions of deuterium and tritium. Usually, the negative ion current density will be lower for the heavier isotope. The source also has to be operated to form negative ion beams using 50:50 mixture of deuterium and tritium. To achieve 2 weeks' operation without source maintenance, multiple sets of tungsten

filaments need to be tested and evaluated for long pulse operation. In such negative ion sources, the molybdenum plasma grid, which operates at a temperature in a range between 600 K and 800 K, needs to be demonstrated for reliable long pulse operation.

Tritium and Cryopumping

The PCAST NBI beamlines have to be designed with double containment chambers for tritium confinement. If the outer chamber is filled with helium, there is no concern for maintaining the accumulated gas below the hydrogen explosion limit. The cryopump modules used in these beamlines should be constructed with a movable shutter so that the pump can be regenerated during beam operation. As elaborated in the next paragraph, the time period between cryopump regeneration in these beamlines will be determined by the tritium inventory. The inventory problem associated with tritium beams is an analysis task in the future engineering phase. The tritium recovery and process system needs to be designed, constructed, and tested.

In the PCAST NBI beamlines, the working gas is deuterium, tritium, or their mixtures, variable up to 50:50 ratio. The neutralizer gas should be deuterium for minimizing tritium accumulation. Following the specification of the JT-60U 500-keV N-NBI beamlines, the gas feed will consist of 5 Pa-m³/s each for deuterium and tritium into the source and 4 Pa-m³/s deuterium into the neutralizer. Under such conditions, the regeneration of the cryopump modules could be determined by the tritium accumulation. Assuming feeding 5 Pa-m³/s tritium for 135 s D:T (50:50) beam conditions, each beam pulse will have about 0.3 moles tritium condensed on cryopanel. It takes only 3 beam pulses to accumulate 5.4 grams of tritium. If the desired operation is as

frequent as one 135-s pulse every 20 min. (for commissioning, for example), then the cryopump modules need to be regenerated every hour. To get the beam system to operate without regeneration interference, each cryopump module could be designed and built with a movable shutter. Then each cryopump module could be isolated from the beam tank and be regenerated separately. The specifications of cryopump regeneration should fulfill the requirements of beam injection including duty cycle and deuterium and tritium mixtures. Such frequent regeneration cycles may demand high cooling capacity of the cryogenic refrigerator. For cooling 24 cryopump modules of the 3 beamlines, the cryogenic system may need to have a cooling capacity of 1000 W.

Remote Handling

The ion source and the beamline should be designed for the convenience of remote maintenance. Because of the concerns of activation, a R&D task needs to be initiated to estimate the neutron flux at various locations in the NBI beamline. For the convenience of remote maintenance, the PCAST beamlines will use double-sealed gate valve at the source end and at the drift duct end. The double-sealed gate valve is being developed for ITER beamlines.

Plasma Neutralizer

The injection power per beamline can be increased substantially by raising neutralization efficiency. This could be done by upgrading the conventional 60% gas neutralizer to a 85% class plasma neutralizer. The rated injection power per beamline will be raised to 14 MW from 10 MW. Subsequently, the fraction of residual ions could be reduced, so does the heat flux or particle flux on the ion dumps. Thus the improvement in neutralization

could minimize the erosion problem of ion dumps. This idea needs to be demonstrated before being applied to the PCAST NBI beamlines.

References

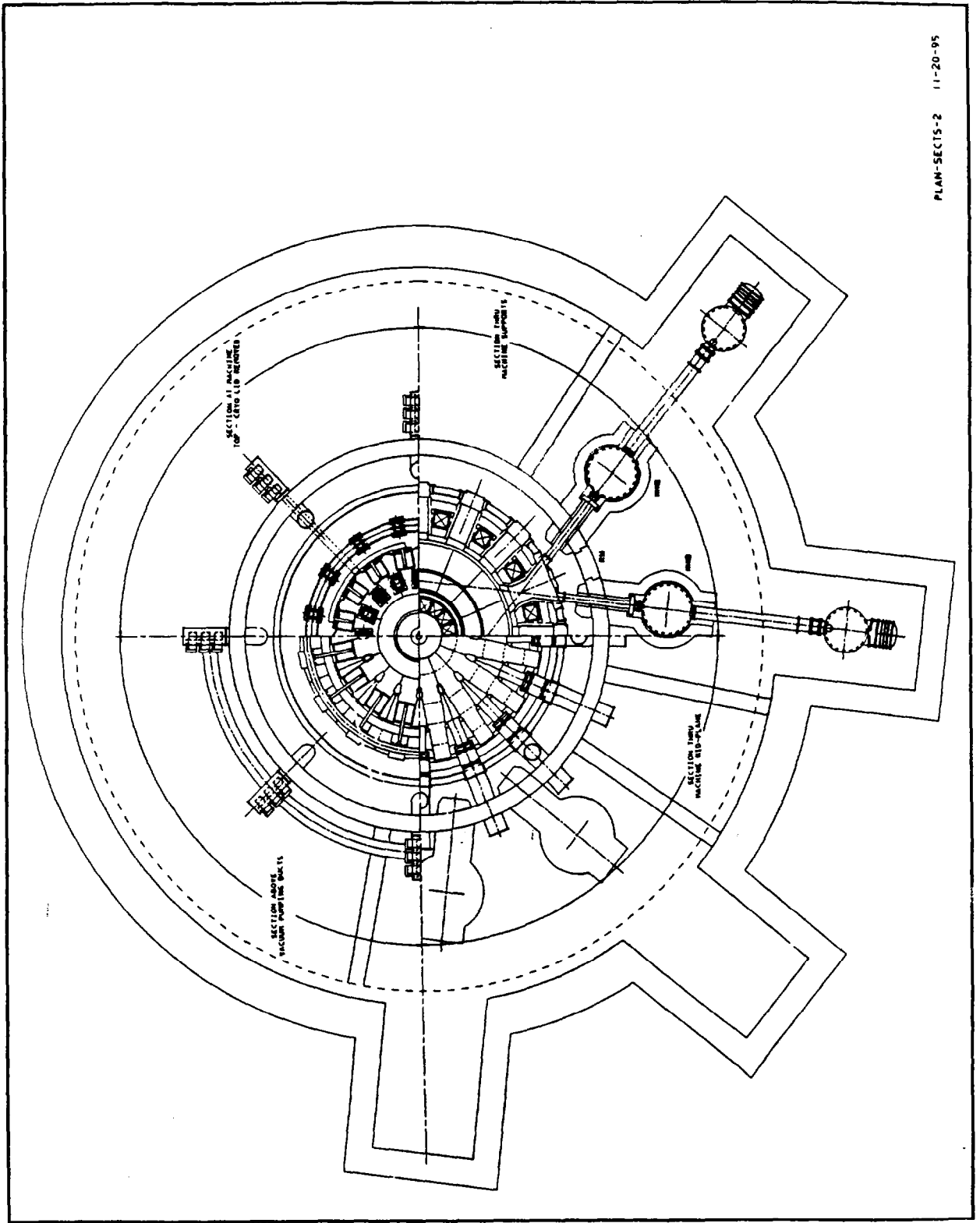
- [1] M. Kuriyama et al., "Construction of a 500 keV Negative-Ion-Based NBI system for JT-60U," Proc. 14th Symp. on Fusion Engineering, Boston, October 1993, pp.470- 473.
- [2] Y. Okumura et al., "Development of a Large D- Ion Source for the JT-60U Negative-Ion-Based Neutral Beam Injector," *ibid*, pp. 466-469.
- [3] Yoshihiro Ohara et al., "ITER Neutral Beam Injection System – Japanese Design Proposal," JAERI - M 91-052 (1991)
- [4] J. Pamela et al., "Neutral Beams for ITER," NET-Report, EUR-FU/XII-163/104-94 (1994).
- [5] ITER-EDA meeting at Cadarache on proposed ITER-NBI System on May 5 and 6, 1994.
- [6] Y. Okumura et al., "Design Study on a 1 MeV, 12.5 MW Neutral Beam Injector Module for ITER," JAERI-Tech 95-018, March 1995.
- [7] Y. Okumura et al., JAERI 1995 Interim Report on the "part of the Engineering and Physics Design of the ITER NBI 2 MeV, 12.5 MW Module," Design Task Agreement N53TD08-94-10-28FJ, April 14, 1995.

Table 1. Specifications of Beamline Required for JT-60U, ITER, and PCAST

	JT-60U	ITER	PCAST
Beam Energy, keV	500	1000	500
Beam Power, MW	10	16.7	10
Pulse Duration, s	10	>1000	135
Beam Species	D	D	D & T
Number of Beamlines	1	3	3
Ion Source/Beamline	2	1	1
Beam Current/source, A	22	40	44
Current Density, mA/cm ²	13	20	16
Source Pressure, Pa	0.3	0.2	0.2
Beam Divergence, mrad	5	3	3
Extraction Area, cm ²	45 x 110	60 x 165	60 x 137
Apertures (14mm diam.)	1080	1300	1800
Total hole area, cm ²	1662	2000	2772
Transparency, %	33.60	20.20	33.6
Accelerator, Stage	3	5	3
Voltage/stage, kV	167	200	167
Source Size			
Diameter, m	2	3	2.3
Height, m	1.7	2	1.5
Weight/source, ton	6.5	20	9.7
Injection port size, cm ²	55 x 55	45 x 110	40x50
Beamline length, m (Ion source to injection port)	24	22.5	16

Notes:

1. The PCAST beamline design is based on the ITER beamline design.
2. The transparency of the grid in the ITER beamline is low because of the sub-divided neutralizer that makes the neutralizer shorter even at the high energy. We expect high grid transparency in the PCAST beamline, where we don't have to use the sub-divided neutralizer.
3. The diameter of the ion source in the PCAST beamline is much smaller than that in the ITER in spite of the wider extraction area in the PCAST. This is because the PCAST needs only three acceleration stages.



PLAN-SECTIS-2 11-20-95

Fig. 1. Plan view of the PCAST test cell. Two beamlines are shown installed on special tangential ports; the space allocated for the third Day-1 beamline and a fourth (upgrade) beamline is also seen.

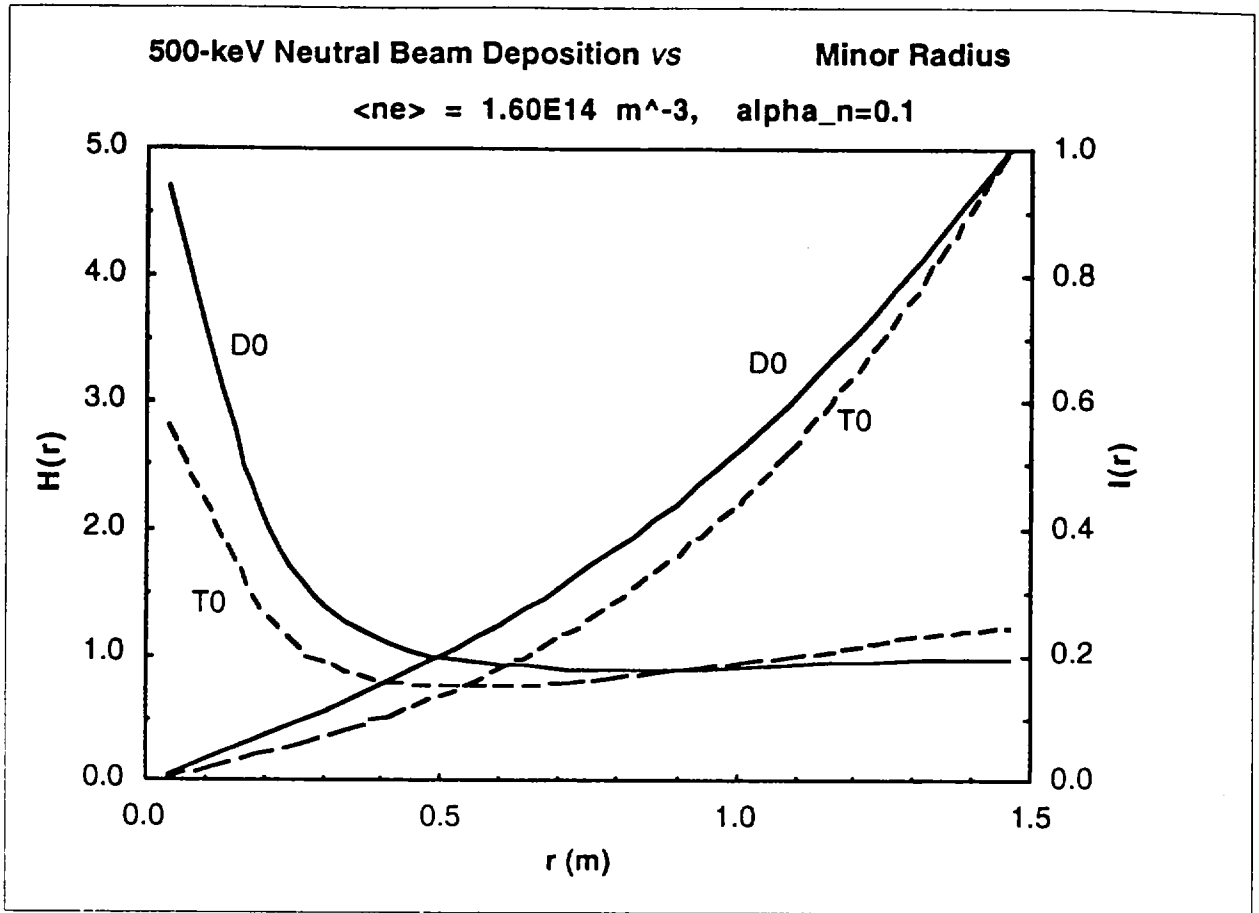


Fig. 2. Calculated neutral beam deposition profile $H(r)$ and its integral $I(r)$ for D^0 and T^0 species for the reference operating density ($\langle n_e \rangle = 1.6 \times 10^{20} \text{ m}^{-3}$) and density profile $n_e \sim [1 - (r/a)^2]^{0.1}$.

1.2.3.b. Ion Cyclotron Heating System for PCAST Machine

D. W. Swain, D. B. Batchelor, M. D. Carter (ORNL)

Introduction and summary

This chapter describes the design of an ion cyclotron heating (ICH) system for the PCAST machine. This system could also be used to heat electrons directly, and to drive current near the plasma center. Throughout the chapter, we describe a design and capabilities of a single unit, consisting of one antenna installed in a horizontal midplane port and its associated tuning and matching equipment, power sources, DC supplies, and control equipment. The number of such units required depends on the power required at the available operating frequencies, and the allowable voltages in the antenna and transmission systems.

Operation of the ICH system is considered for 3 frequencies at 7 T central magnetic field:

- 70 MHz for ion heating ($2\omega_T$ and He³ minority)
- \approx 80 MHz for direct electron heating (and possibly current drive)
- 105 MHz for ion heating ($2\omega_D$ and H minority)

Under nominal density profiles and distance from the separatrix to the first wall at the outer midplane, a simple antenna system can deliver up to 15 MW to the plasma at 70 and 80 MHz. While the antennas can deliver this amount of power also at 105 MHz without exceeding the nominal voltage limit of 35 kV in the rf system, the rf power sources may limit the power at

this frequency to about 11 MW/port, unless better rf sources than those presently available are developed.

The antenna is very similar to the one currently under design for ITER. The port size for this machine (1.37 m wide, 2.64 m high) is very close to the present ITER horizontal ports (1.60 m wide, 2.60 m high). It consists of eight current straps mounted in a four (toroidal) by two (poloidal) array. Each current strap is grounded at the center and fed at each end by a vacuum coax.

Tuning and matching is similar to the present ITER concept, and should allow dynamic matching to ELM's (for example). RF sources similar to those presently available are envisioned, possibly with some modest upgrading of tube capabilities to allow higher power operation at the 105 MHz frequency.

RF sources are available that will tune 30 –120 MHz, and the system could be designed to operate at any frequencies in this range. However, such flexibility might reduce the power-handling capability at some desired frequencies of operation, compared to a system that was optimized for operation at that frequency.

Physics

Heating Scenarios

For 7 T operation, the various resonant frequencies are shown as a function of position in Fig. 1. The graph spans the range from the inner radius of the plasma ($R = 3.5$ m) to the outer radius ($R = 6.5$ m).

Based on the resonant curves, we choose the following operating modes:

- $f = 70$ MHz for
 - $2\omega_T$ heating in a D-T mixture. Fully ignited plasma.
 - He^3 minority heating in a D- He^3 mixture, with He^3 as a minority species. Startup experiments.
- $f \approx 80$ MHz for
 - Direct electron heating, possibly for fast-wave current drive, if desired. There will be competition at this frequency between electron absorption and $2\omega_T$ absorption at the resonance past the machine center. The power split between them depends on several factors, including the phase velocity in the toroidal direction of the launched wave.
- $f = 105$ MHz for
 - $2\omega_D$ heating, either in a pure D plasma or a D-T mixture
 - H minority heating in a H-D mixture

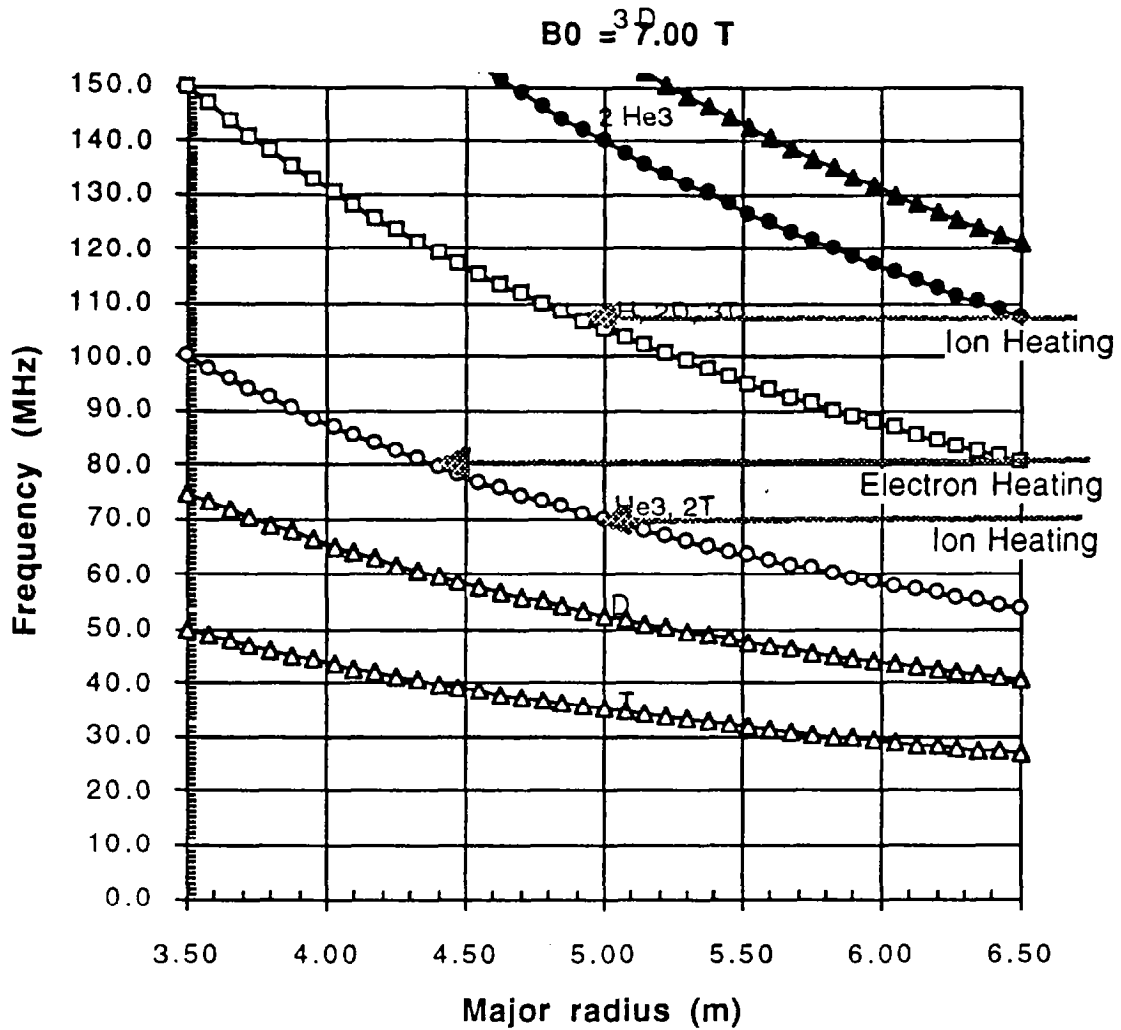


Fig. 1. Resonant frequencies of various ion species vs. major radius, for a magnetic field of 7 T at the plasma center ($R_0 = 5 \text{ m}$).

Density profile

We use the density profile given as:

$$\begin{aligned}
 n(r) &= (n_0 - n_{\text{edge}}) (1 - r^2/a^2)^{\alpha n} + n_{\text{edge}} & \text{for } r < a \\
 &= n_{\text{edge}} \exp\{-(r-a)/\lambda\} & \text{for } r > a
 \end{aligned}$$

for values of density parameters:

$$n_0 = 1.8 \times 10^{20} \text{ m}^{-3}$$

$$n_{\text{edge}} = 0.33 \times n_0 = 0.6 \times 10^{20} \text{ m}^{-3}$$

$$a = 1.5 \text{ m}$$

$$\lambda = 0.02 \text{ m}$$

$$\alpha_n = 0.1$$

Ion density is a 50/50 mix of D/T

The resulting value of volume avg. density is $\langle n \rangle = 1.58 \times 10^{20} \text{ m}^{-3}$.

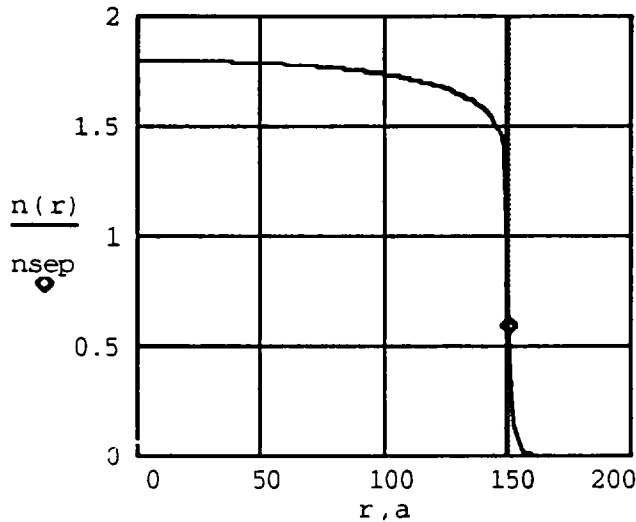


Fig. 2. Density profile used in loading calculations. In this plot, the separatrix is located at $r = 150 \text{ cm}$.

The results of loading calculations obtained from the RANT3D code using this density profile will be given in the section discussing the power-handling capability of the antenna, after the design of the antenna has been described.

Antenna design

Antenna geometry

- We assume a Faraday shield (FS) and antenna layout similar to the ITER design. The antenna with FS is inserted through a main horizontal port.

- We assume the front of the FS is 1 cm behind the first wall or first limiter that defines the end of unrestricted plasma volume.
- The cross-section of the antenna is as shown below. The current strap is 5 cm thick, with its front surface 6 cm behind first wall.
- The septum is 16 cm behind first wall.

Figures 3–5 show dimensions of the antenna. Two of the units shown in Fig 3 will fit into a port that is 137 cm wide by 264 cm high, the nominal port size for the machine.

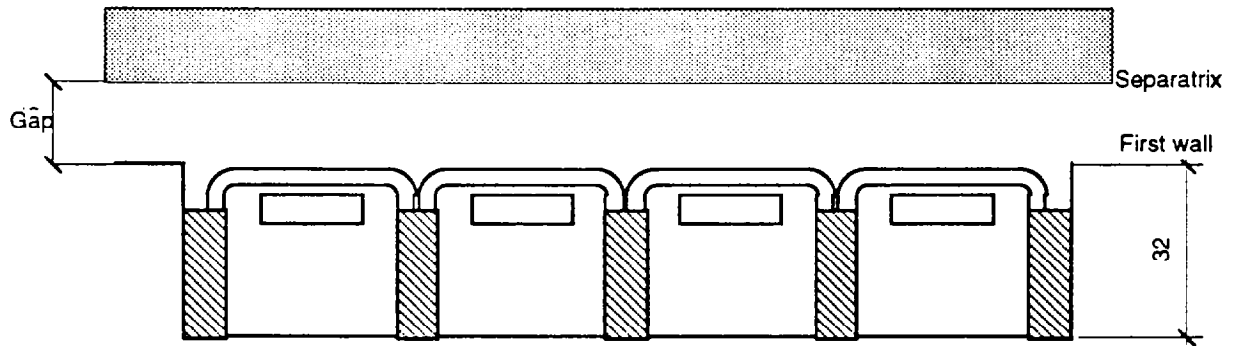


Fig. 3. Cut through antenna, showing 4 current straps, septa, and first wall.

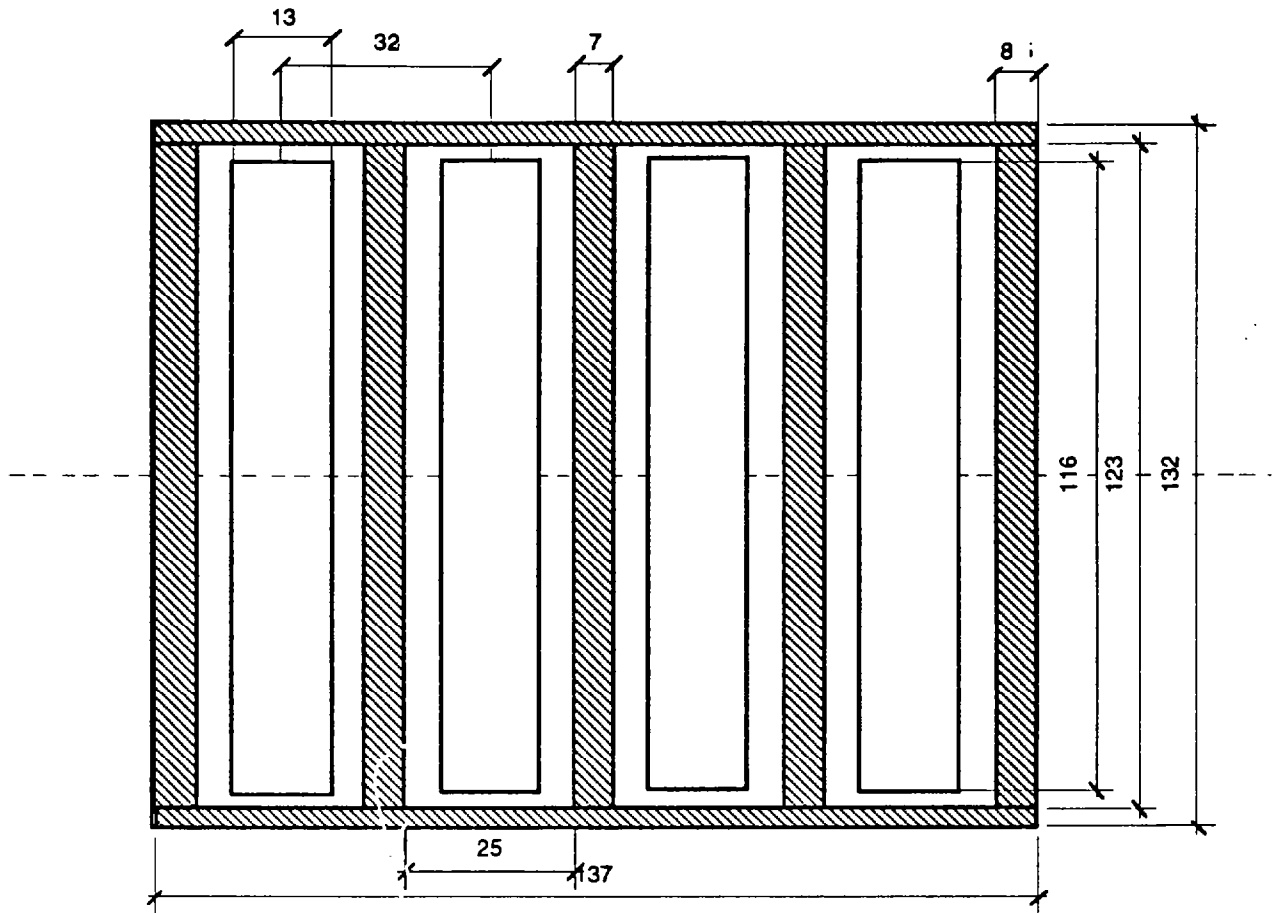


Fig. 4. Front view from plasma (Faraday shield not shown). Two of these stacked vertically fill one port on the PCAST machine.

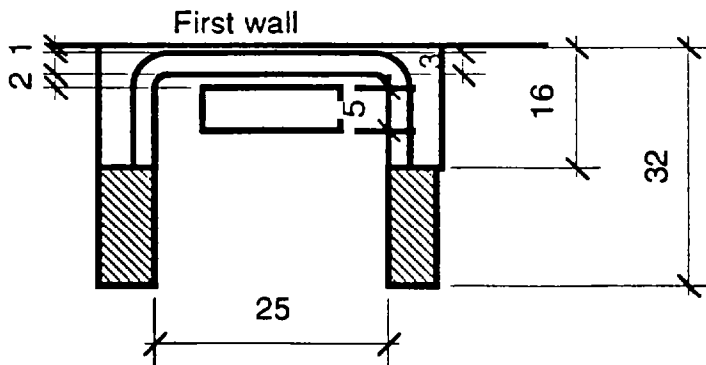


Fig. 5. Detail of antenna cross section.

Antenna electrical characteristics

- Based on calculations for ITER for similar strap configurations (Ref. [1]) we take $Z_{\text{strap}} = 40$ ohms, $\beta_{\text{strap}} (= v_{\text{phase}}/c) = 0.7$.
- Strap is grounded at the center, and fed at both ends by vacuum transmission line.
- We choose the vacuum transmission line characteristic impedance to be 30 ohms.

Power to the plasma calculations

Figs 6 and 7 show the voltage and current vs. distance from the strap ground for $f = 70$ and 105 MHz. The end of the current strap is shown by a vertical line in the figures. For this calculation, the maximum voltage anywhere in the system was constrained to equal 35 kV.

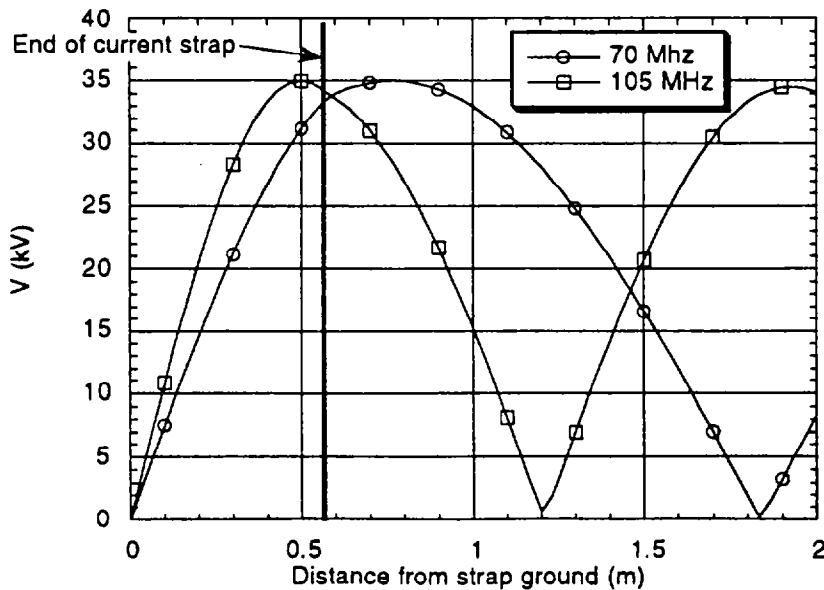


Fig. 6. Voltage in antenna/transmission line system, with $V_{\text{max}} = 35$ kV

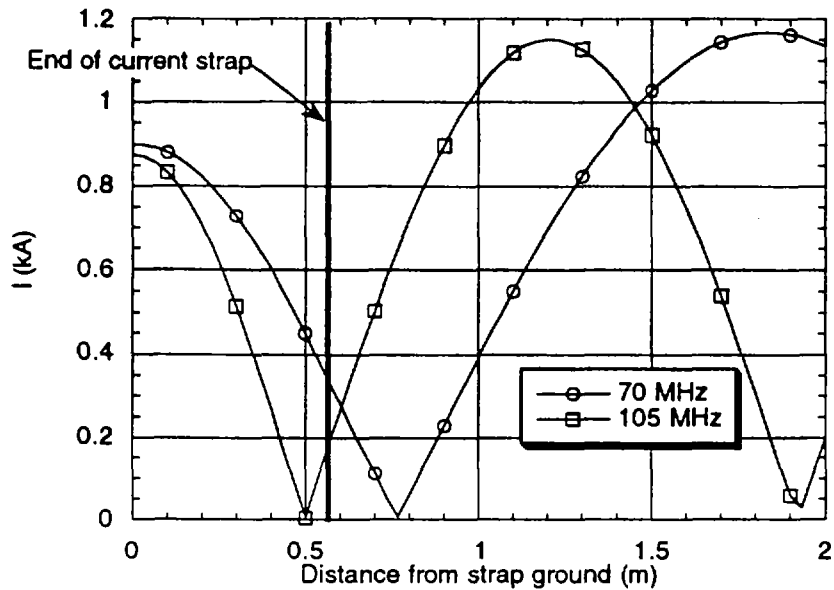


Fig. 7. Current in antenna/transmission line system for $V_{max} = 35$ kV

Power to the plasma at 70 MHz

Fig. 8 shows the results from a RANT3D, Ref. [2], loading calculation coupled with the circuit analysis results shown above. For these curves, the plasma loading was computed using the density profile shown in Fig. 1, and the antenna geometry parameters shown in Figs. 2-4. Here, the gap is the distance from the plasma separatrix to the first wall, as defined in Fig. 2.

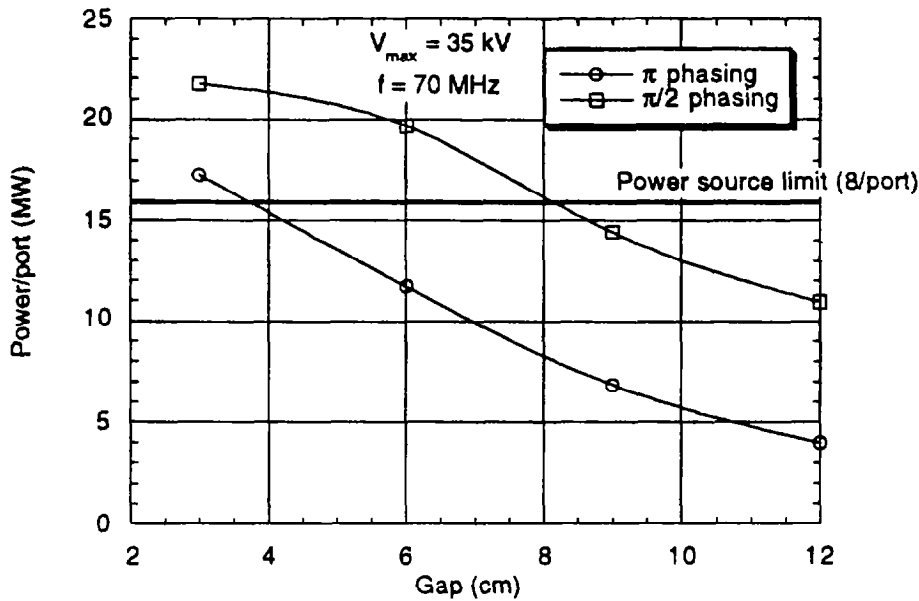


Fig. 8. Power per port at $f = 70$ MHz vs. the gap between the first wall and the separatrix, for $V_{\max} = 35$ kV.

If the maximum voltage anywhere in the rf system is constrained to 35 kV, 15 MW/port can be obtained for π phasing if the gap is ≤ 4 cm; for $\pi/2$ phasing, 15 MW/port can be obtained for a gap ≤ 9 cm. Also shown on the figure is a line at 16 MW representing the maximum power that can be delivered to the plasma if eight rf transmitters are used to power the current straps in one port (see section on rf power sources). This assumes that 2 MW/transmitter can be delivered to the plasma at this frequency. Commercial units designed to deliver 3 MW into a matched load are available, so this is a reasonable assumption.

Figure 9 shows the maximum voltage required to deliver either 10 MW/port or 15 MW/port as a function of the gap, for two phasing values between adjacent current straps. In practice, 35 – 40 kV is probably a reasonable upper bound on the acceptable value of V_{\max} .

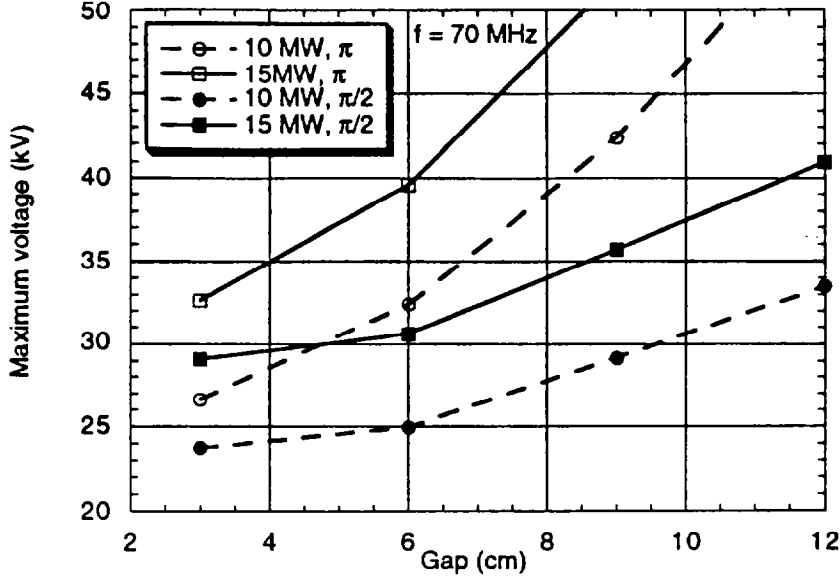


Fig. 9. Maximum voltage in antenna/transmission line vs. gap, for two powers/port (10 and 15 MW) and two phases between current straps (π and $\pi/2$), for $f = 70$ MHz.

Power to the plasma at 105 MHz

Figure 10 shows the power per port for π and $\pi/2$ phasing as a function of gap. For this frequency, the loading actually increases (for $\pi/2$ phasing) as the gap is increased. This phenomenon has been seen before in calculations during the conceptual design of an antenna system for BPX (Ref. [3]). When the plasma is too close to the antenna, the plasma impedance as seen by the antenna gets to be too good, and the plasma begins to look more like a highly conducting medium than a lossy medium.

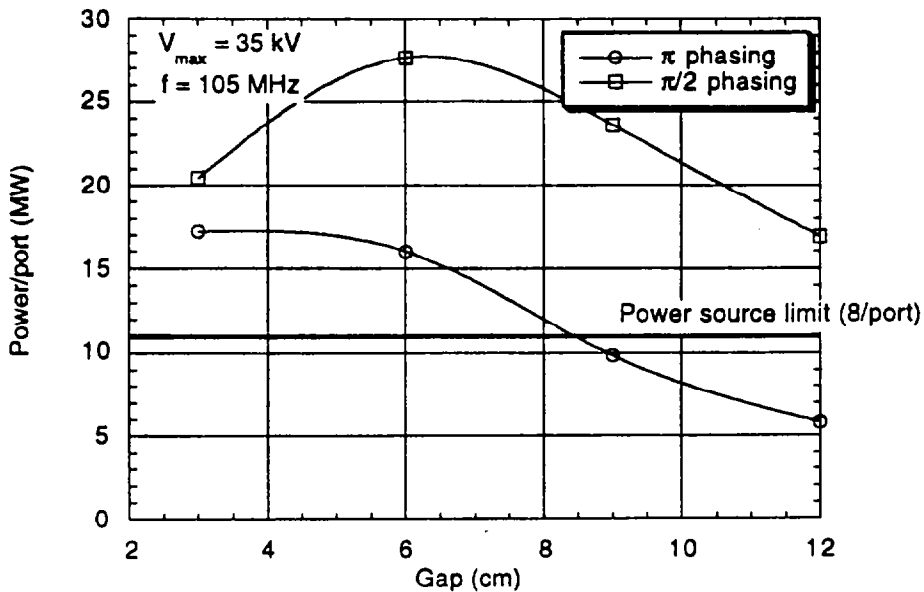


Fig. 10. Power per port at $f = 105$ MHz vs. the gap between the first wall and the separatrix, for $V_{\max} = 35$ kV.

At 105 MHz, the power sources cannot deliver as much power as at 70 MHz. The limit is shown in the figure at approximately 11 MW/port, assuming that there are eight rf power sources of presently available design used to power the antennas (see section on rf sources). Thus, for all but the largest gaps at π phasing, the limitation on the power delivered to the plasma (assuming operation at 35 kV is acceptable) will be limited by the source power available instead of the maximum operating voltage.

Figure 11 shows the maximum operating voltage vs. gap for two values of power and two phasings, for $f = 105$ MHz.

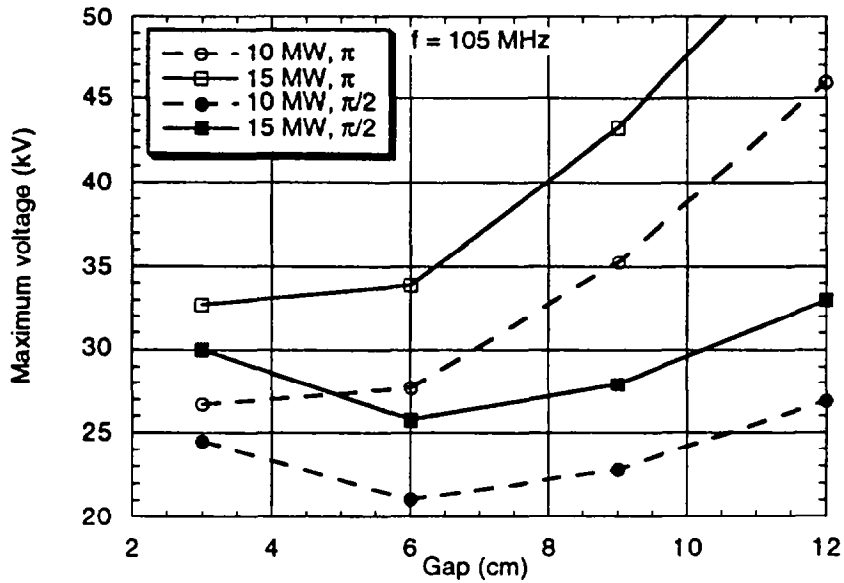


Fig. 11. Maximum voltage in antenna/transmission line vs. gap, for two powers/port (10 and 15 MW) and two phases between current straps (π and $\pi/2$), for $f = 105$ MHz.

Description of the rest of the IC system

Tuning and matching

A schematic of the IC system is shown in **Fig. 12**. This figure shows the components needed to power the top (or bottom) half of one port.

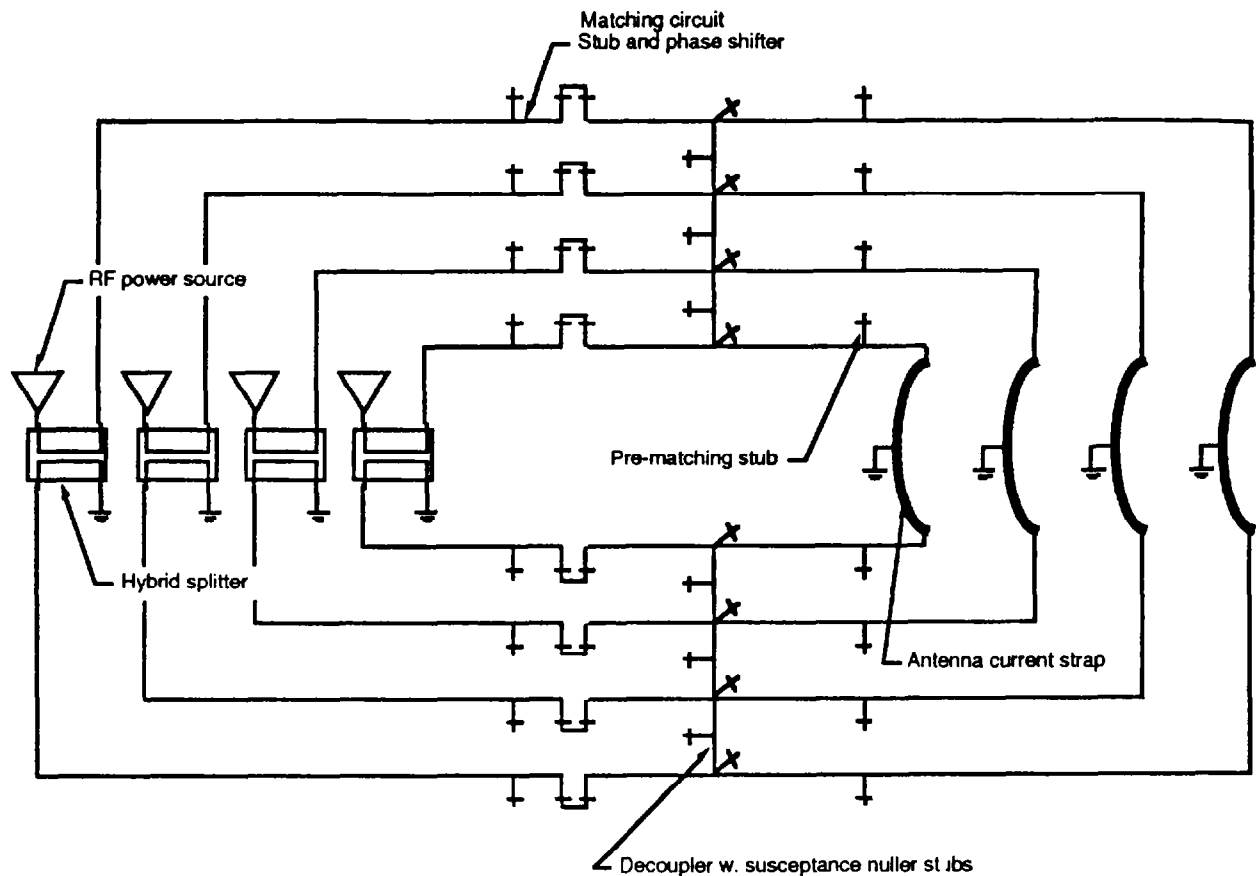


Fig. 12. Schematic of the rf components needed to power 1/2 of an in-port IC antenna.

For a one-port, 15 MW system, the system contains twice the components shown:

- Eight rf power sources
- Eight 9" pressurized transmission lines from the sources to the tuning and matching circuitry
- Eight hybrid power splitters (one for each line)
- 16 matching circuits consisting of:
 - Stub tuner
 - Phase shifter

- 12 decoupler circuits consisting of:
 - Coax connecting adjacent feedlines
 - Stub tuner
- 16 susceptance nuller stubs (possibly, optional)
- 16 Pre-matching stubs (possibly, optional)
- 16 vacuum feedthroughs
- One port-mounted antenna, consisting of 8 center-grounded current straps, with each strap fed at both end for a total of 16 inputs.

This design is similar to the one that has been studied for ITER. While details of the tuning and matching system design will evolve, the overall system will look a lot like the one shown. The system described above will be adequate for costing purposes.

RF sources

RF power sources are commercially available that will do the job needed for ITER, especially at frequencies below 80 MHz. For example, new rf sources purchased by GA for use on the DIII-D experiment cover the frequency range 30 – 120 MHz. **Fig. 13** shows the power that can be delivered at a VSWR of 1.5:1 vs. frequency (Ref. [4]).

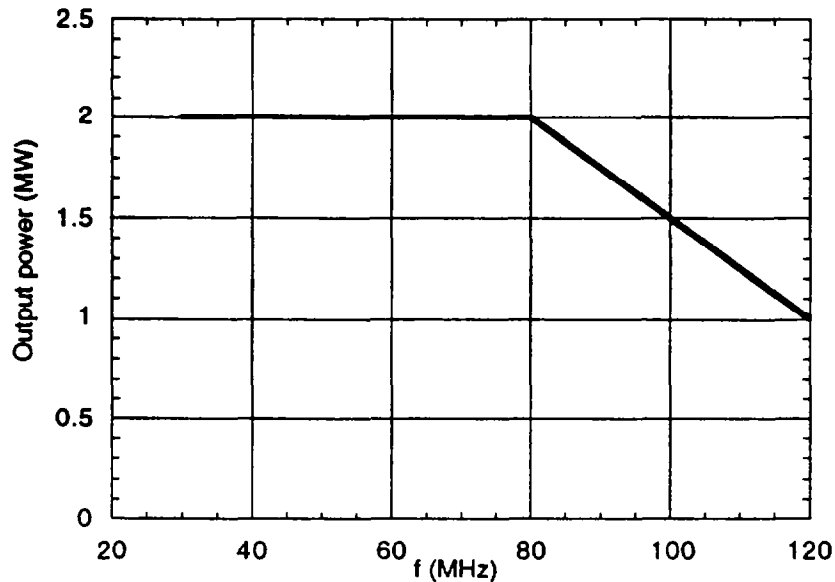


Fig. 13. Output power vs. frequency for DIII-D sources into a load with a VSWR of 1.5.

At 70 MHz, the nominal output power into the mis-matched load is 2 MW, so eight rf sources could supply 16 MW to the plasma; this is the horizontal line shown in Fig. 8. Above about 80 MHz the rated power decreases, so that at 105 MHz the power available is only about 1.4 MW. This means that at this frequency, eight sources could only supply about 11 MW of power to the plasma; this is the horizontal line shown in Fig. 10.

There are three avenues to take to cope with the reduction in source power at the higher frequency:

- Accept reduced power to about 11 MW per port at the higher frequency
- Assume that advances in tube manufacture over the next decade will allow 2 MW per tube operation at the higher frequency
- Increase the number of power sources per antenna

For the purpose of the costing exercise, we assume that either of the first two options is adopted.

AC power, cooling, controls

The overall efficiency of an IC system from AC power to heating the plasma is about 55–60%, depending on several factors. Therefore, for 15 MW of rf power/port into the plasma, the total AC power needed will be 25 – 28 MW.

The cooling system will be required to remove the excess heat, namely about 15 MW per antenna unit. The bulk of this heat is generated at the transmitters, which are about 66% efficient.

In addition, hardware and software for ICH system control, data acquisition, and analysis will be required. These are not described here, but are mentioned for completeness.

References

- [1] D. Taylor et al., "Final Report for ITER Task D89", ITER US Home Team Document ITER/US/95/IV-RF-02 (March 24, 1995).
- [2] M. D. Carter et al., "Three-dimensional physics of ICRF launchers for fusion devices", accepted for publication in *Nuclear Fusion*.
- [3] D. W. Swain et al., "The ion cyclotron Heating (ICH) system for BPX", v. 1, p. 94, Proc. 14th Inst. Electr. Electron. Eng./Nucl. Plasma Sci. Soc. Symp. on Fusion Engineering, San Diego, Sept. 30-Oct. 3, 1991, IEEE, New York, 1991.

[4] ABB transmitter information from General Atomics, private communication.

1.2.4 Plasma Shaping Experimental Basis

E. Lazarus (ORNL)

In this study we have taken advantage of plasma shaping to optimize the tokamak design. Shaping allows a substantial reduction in machine size and increase in beta margin relative to ITER, while maintaining ITER's ignition margin. These benefits are predicated on the assumption that 1) $q_{95}=3$ remains a valid operational limit, and 2) the energy confinement scalings are valid over the range of shapes considered. The shape parameters we have used are well justified by the experimental data base for operation with shaped plasmas at $q_{95} \geq 3$ and H-mode confinement. Here we use the DIII-D data base to illustrate the required effects.

a. Stability Boundaries

The picture of shaping effects presented here has evolved over the past several years on the DIII-D tokamak and is closely related to aspect ratio. In fact we begin by defining a shape parameter $S \equiv I_N q$, where $I_N = I_p / a B_T$. [1] This can be motivated by making an analogy with ϵ , the inverse aspect ratio. In a circular tokamak the safety factor is simply

$$q = \frac{a B_T}{R B_p} = 2\pi \epsilon \left[\frac{\mu_0 I_p}{a B_T} \right]^{-1} \quad (1)$$

while for general shapes S is defined by the relation,

$$q = \frac{1}{2\pi} \oint \frac{B_T d\ell}{R B_p} \equiv \mu_0 S \left[\frac{\mu_0 I_p}{a B_T} \right]^{-1}. \quad (2)$$

By analogy with Eq. (1) we can identify S as a generalized inverse aspect ratio (within a factor $\mu_0/2\pi$). An interpretation of S , consistent with this analogy, is that S reflects the

fraction of a flux contour on the high field side of the tokamak. This makes S more general than a specification of κ and δ . With this interpretation of shaping, then decreasing ϵ , which reduces the ratio B_{\max}/B_{\min} across the plasma, will tend to offset the benefits of cross section shaping. Conversely, increasing S through shaping is equivalent to reducing the aspect ratio (i.e., increasing ϵ) as a means of increasing the current-carrying capacity of the plasma.

Another reason S is attractive as a descriptor of shaping is that it incorporates the familiar Troyon beta limit ($\beta_{\max}=gI_N$) while S itself is bounded by axisymmetric ($n=0$) stability for a fixed current profile. In DIII-D this limit (S_{\max}) is about 8.3 at $\ell_i = 1$. Using S and q , the Troyon limit can be considered an expression limited by $n=0$ stability (through S) and $n=1$ stability (through g and q), i.e., $\beta_{\max} = gS/q$. We can thus increase the beta limit by increasing S , given limits on g and q .

In DIII-D the q_{95} representation of the safety factor (i.e., q evaluated at the 95% flux surface) appears to have the same operational meaning as the edge safety factor in limited circular tokamak plasmas. Analysis of the DIII-D stability data base shows that operating space is clearly bounded at $q_{95}=2$ for plasmas covering a wide range of shapes and beta ($S \leq 7$ and $\beta_N \leq 4$ near the $q_{95}=2$ limit). The few exceptional plasmas which achieved $q_{95} < 2$ have been examined and found to have certain common features. In these the $q=2$ surface was very close to the edge [$0.965 < \psi/\psi(a) < 0.985$]. All occurred during a current ramp and were followed by disruptions a few ms after the time of the equilibria presented. All are at low beta ($\beta_p \approx 0.1$); DIII-D has never achieved a reasonable β at $q_{95} < 2$. Thus, $q_{95}=q_{\min}$ accurately represents a tokamak operational boundary for all shapes, and therefore $q_{95}=\text{constant}$ (in the case of ITER, 3) is a valid design limit.

Since the highest β values in DIII-D are typically obtained with q values close to the limit (about 2.5) we would expect to see a good correlation between S and β_{\max} . This is shown in Strait's review paper [2] for a number of tokamaks. For DIII-D diverted plasmas we evaluate S as $q_{95}I_p/aB_T$. The stability data base shows that β_{\max} is proportional to S , consistent with the picture of the intersection of $n=0$ and $n=1$ stability boundaries [3].

b. Confinement Scaling

Next we consider the applicability of typical tokamak confinement scaling assumptions to strongly shaped plasmas. The confinement properties of tokamaks can be represented in a simple way, using the DIII-D/JET scaling,

$$\tau_E = 0.11 \times F \left(\frac{I_p R^{3/2}}{\sqrt{P}} \right) \quad (MA, m, MW, s) \quad (3)$$

Then a lowest order performance figure-of-merit, $\beta\tau_E$ ($\propto nT\tau_E/B^2$), simplifies to

$$\beta\tau_E \cong 0.13 \times \left[\frac{S^2 R^2}{\kappa} \right] \left[\frac{F^2}{q^2} \right] \quad (\% \cdot s, m) \quad (4)$$

with some uncertainty as to whether replacing κ with $(1+\kappa^2)/2$ provides a better representation of the data. The constituents of this relationship are discussed in [4]. This is a very constraining relationship, since both S and q are limited by stability. This formula simply predicts that, for a given machine size, $\beta\tau_E$ is increased by raising S , thereby allowing I_p to be as high as possible without making the safety factor too low. The predicted proportionality between maximum $\beta\tau_E$ and $\left[\frac{S^2 R^2}{\kappa} \right] \left[\frac{F^2}{q^2} \right]$ is confirmed by the DIII-D confinement data base, which has little overlap with the shape experiment on DIII-D

in 1993 [5] or the stability data base used above. This data base covers a range in S arising largely from differences between single and double null plasmas.

The factor F in Eq. (3) is somewhat greater than 1.0. Originally, this scaling was developed for ELM-free H-mode. However, as the DIII-D machine has become cleaner (through boronization) and freer of metallic impurities (outer wall armor tile) the coefficient has risen. A representative value in double null plasmas for ELMing H-mode is 1.2 or 1.3. The coefficient is thought to be lower in single-null plasmas, but this would need further investigation if the value of F were important. The F factor is related to the more familiar H-factor (ITER-89P confinement multiplier) by $H \approx 0.15 + 1.35F$.

c. Shaping Potential for Tokamak Design

ITER has chosen an operating point where $q=3$ and $S=4$. Although the PCAST illustrative design has a more strongly shaped cross section, it also has a lower ϵ , so S is only increased to 4.4. The DIII-D tokamak operates routinely with S values up to 6.5, corresponding to $\kappa_x=2.1$, $\delta_x=0.85$. A key requirement for reliable operation in this regime is the use of an optimized vertical position control system. With further measures to avoid the axisymmetric instability, DIII-D has reached S values as high as 8. Thus the data base exists to justify consideration of tokamak designs with stronger shaping (higher S) than that adopted for the PCAST machine, with proper attention to vertical control.

References

- [1] E.A. Lazarus, et. al., Phys. Fluids **B4** (1992) 3664.
- [2] E.J. Strait, Phys. Plasma **1** (1994) 1415.
- [3] E.A. Lazarus, et. al., Phys. Fluids **B3** (1991) 2220.
- [4] E. A. Lazarus, Proceedings , *20th EPS Conference on Controlled Fusion and Plasma Physics*, Vol 17C , p I-95.
- [5] E. A. Lazarus, et. al. IAEA (Seville) Paper IAEA-CN-60/A-5-I-1.
- [6] E.A. Lazarus, et.al., Nucl. Fusion **30** (1990) 111.

1.2.5.a Poloidal Field System Design

R. H. Bulmer (LLNL)

PF configuration

The design of the poloidal field system draws on experience with earlier tokamak designs, particularly those of the BPX [1] and TPX [2] machines. We have selected a PF configuration with 14 coils having up-down symmetry, with 7 independent circuits, as shown in figure 1. The solenoid is comprised of a total of 8 modules (PF1-4U&L), and provides both poloidal flux and a significant shaping function during the scenario. The vertical partitioning of the modules was selected to support the highly-shaped plasma ($\delta_{95} \approx 0.45$, $\delta_r \approx 0.9$) A "divertor coil", PF5, maintains elongation and the outer ring coils (PF6 and PF7) supply the primary vertical field over a range of poloidal beta.

The reference plasma configuration is based on the parameters listed in Table 1.

Table 1 — Plasma parameters for the reference configuration.

<i>toroidal field,</i>	$B_\phi = 7.00$	T
<i>plasma current,</i>	$I_p = 15.30$	MA
<i>major radius,</i>	$R_o = 5.00$	m
<i>minor radius,</i>	$a = 1.50$	m
<i>elongation,</i>	$\kappa_{95} = 1.75$	
<i>triangularity,</i>	$\delta_{95} = 0.45$	
<i>poloidal beta,</i>	$\beta_p = 0.50$	
<i>internal inductance,</i>	$\ell_i = 0.85$	
<i>safety factor, on axis,</i>	$q_o = 0.90$	

Where the definitions of normalized internal inductance and poloidal beta¹ are respectively:

$$\ell_i = \frac{2 \int B_p^2 dV}{\mu_0^2 R_o I_p^2}$$

$$\beta_p = \frac{4 \int p dV}{\mu_0 R_o I_p^2}$$

The value of poloidal beta in Table 1 is consistent with a normalized beta ($\beta_N = \frac{\beta\phi}{I/aB}$) of 1.60.

¹ These definitions are sometimes referred to as $\ell_i(3)$ and $\beta_p(3)$

From the reference equilibrium, the coordinates of the outboard strike-point and a belt-limiter point were extracted and used as shape constraints for subsequent equilibria. This ensures consistency of divertor geometry and utilization of the available vertical space for the plasma (the flux surface defining the scrape-off-layer, SOL, envelope is constrained to just pass within the belt-limiter point). These *constraint point* coordinates are:

$$R, Z_{div} = 3.962, \pm 3.964\text{m}$$

$$R, Z_{belt} = 5.660, \pm 2.117\text{m}$$

Consequently, actual values of the elongation and triangularity for any particular equilibrium will deviate from the nominal (or reference case) depending upon profile parameters and the flux state.

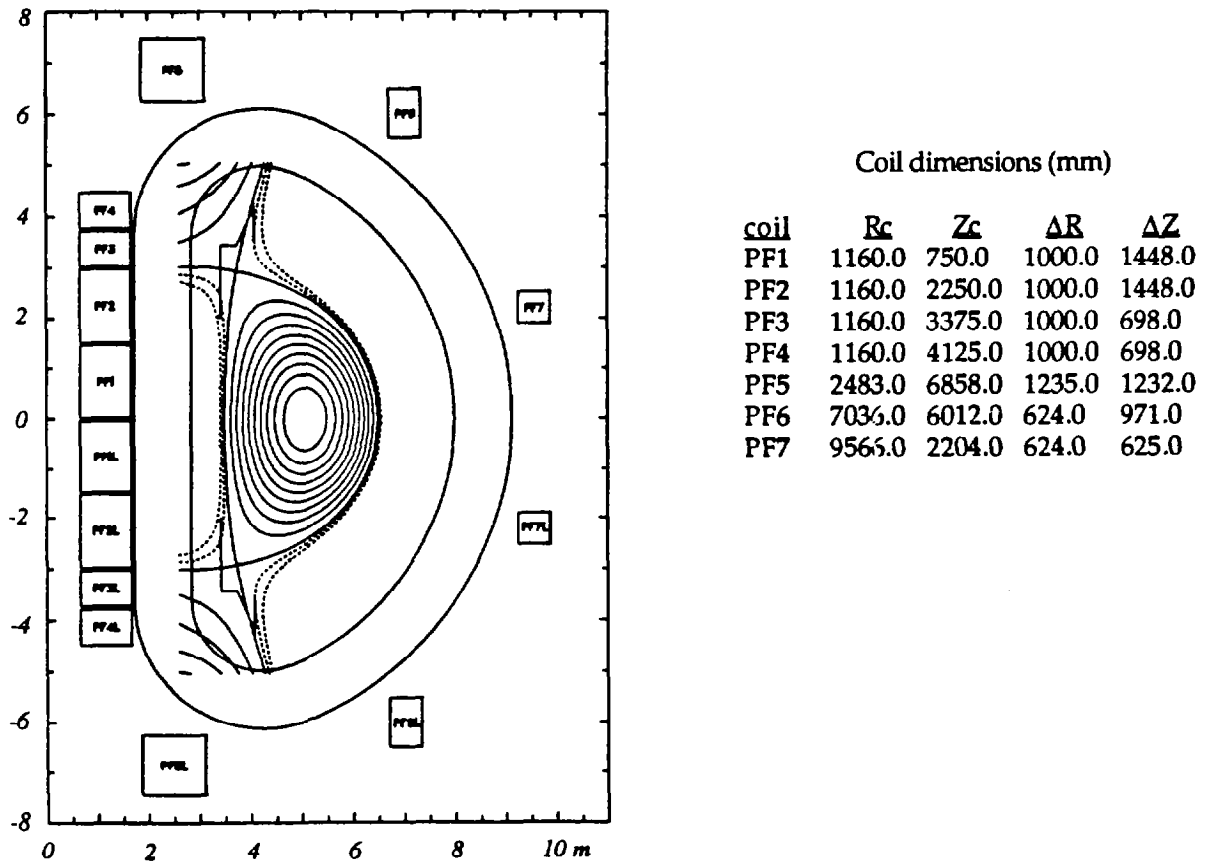


Figure 1 — Poloidal field system.

Plasma profile models

The plasma profile models include a sawtooth parameter to flatten the current and pressure near the magnetic axis.

$$p(\psi) = p(0) \quad \tilde{\psi} \leq \tilde{\psi}_s$$

$$p(\psi) = p(0) \left[1 - \left(\frac{\tilde{\psi} - \tilde{\psi}_s}{1 - \tilde{\psi}_s} \right)^2 \right]^2 \quad \tilde{\psi} > \tilde{\psi}_s$$

and the parallel current density, $J_0 \equiv \frac{1}{R_0} \frac{\langle \vec{j} \cdot \vec{B} \rangle}{\langle \vec{B} \cdot \nabla \phi \rangle}$, with:

$$J_0(\psi) = J_0(0) \quad \tilde{\psi} \leq \tilde{\psi}_s$$

$$J_0(\psi) = J_0(0) \left[1 - \left(\frac{\tilde{\psi} - \tilde{\psi}_s}{1 - \tilde{\psi}_s} \right) \right]^{\alpha_j} \quad \tilde{\psi} > \tilde{\psi}_s$$

with normalized poloidal flux:

$$\tilde{\psi} = \frac{\psi - \psi_{axis}}{\psi_{edge} - \psi_{axis}}$$

The desired values of q_0 and ℓ_i are achieved by adjusting the profile parameter, α_j , and the sawtooth parameter, $\tilde{\psi}_s$.

Poloidal flux consumption

The total poloidal flux consumption is estimated to be $\Delta\Psi_{ext} = 216.7$ Wb according to the distribution in Table 2, with resistive consumption during the current ramp-up based on Ejima [3] scaling (with the coefficient $C_{Ejima} = 0.5$):

<u>Table 2 — Poloidal flux consumption estimate</u>		
<u>Phase</u>	<u>Basis</u>	<u>Wb</u>
Delay to initiation		7.5
ramp-up	$\Delta\Psi_{ind} = L_p I_p$	146.1
ramp-up	$\Delta\Psi_{res} = C_E(\mu_0 R_0 I_p)$	48.1
heating	$\Delta\Psi_{heat} = 0.2 \text{ V} \times 15\text{s}$	3.0
burn	$\Delta\Psi_{burn} = 0.1 \text{ V} \times 120\text{s}$	12.0
<u>Total</u>		<u>216.7</u>

The inductive term includes the flux consumed in going from the low-beta start-of-flattop, SOF state (at the end of the current ramp-up) to the full beta start-of-burn, SOB, state, so:

$$L_p = L_p^{SOB} = 9.55\mu H$$

where this inductance is derived from the actual current distribution in the equilibrium field. The flux consumption estimate assumes a heating phase of 15s duration, and a full-beta burn phase of 120s duration.

Coil engineering constraints

Thermal and structural considerations in the magnet design will limit the peak currents and/or the length of the scenario. In the development of the fiducial equilibria, these constraints are treated as follows. In general, a thick solenoid will have greater thermal capacity and therefore less temperature excursion during the required pulse, but a thin solenoid is more efficient in flux production and will result in lower radial forces. (The tradeoff variation of the solenoid radial build is discussed in more detail in a subsequent section.) Values of the flux-linkage at initial magnetization and end-of-burn, EOB, are adjusted to (1) provide the total required flux-swing, and (2) balance the radial or hoop forces in the coils at the two states. A target value of:

$$\frac{F_R}{\Delta Z_{coil}} = 1400 MN / m$$

is considered feasible from structural considerations, and this value indicates a required coil thickness of approximately 1m. The degree of pre-cooling can be estimated by calculating the value of the specific heat generation:

$$\int J_{Cu}^2 dt \text{ with } J_{Cu} = \frac{1}{0.88} J_{pack}$$

over the scenario, and relating this value to the resistivity function of the particular conductor and its allowable temperature excursion.

Initial magnetization state

An initial magnetization or pre-bias state was developed to relate the flux linkage to peak currents and radial forces, in order to provide guidance on the required flux linkage at EOB to balance the forces in the solenoid. With a solenoid having $\Delta R = 1.00$ m, a pre-bias flux linkage of:

$$\Psi_{cur}^{IM} = 104 Wb$$

approximately balances the radial forces at the two flux states. The corresponding coil parameters at IM are given in Table 3, below.

Table 3 — Coil parameters at initial magnetization.

coil	NI	J_{pack}	B_{max}	F_R	F_Z	$\frac{F_R}{\Delta Z_c}$
	MA	A/mm ²	T	MN	MN	MN/m
PF1	28.52	19.70	23.92	1979	-10	1367
PF2	28.52	19.70	23.62	1931	-68	1334
PF3	13.75	19.70	22.19	871	-107	1248
PF4	13.75	19.70	20.18	783	-303	1122
PF5	30.11	19.79	13.54	1578	-225	1281
PF6	-0.01	-0.02	0.22	0	0	0
PF7	0.42	1.08	0.27	-1	-1	-2

Note the average radial force per unit height of coil PF1 is 1367 MN/m, just under the target value.

Fiducial equilibria

The fiducial states characterizing the scenario equilibria are:

XPF	x-point formation
SOF	start-of-flattop (end of the current ramp-up, low beta)
SOB	start-of-burn (full current, full beta)
EOB	end-of-burn

The XPF state can place demands on the divertor coil, PF5, current. The initial magnetization state is also evaluated since it is limited by the coil allowables. The four shape constraints described earlier, i.e.:

$$\psi(R_0 + a, 0) = \psi(R_0 - a, 0) = \psi(R_{div}, Z_{div}) \equiv \psi_{xpt}$$

$$\psi(R_{belt}, Z_{belt}) \equiv \psi(R_0 + a + \Delta R_{SOL}, 0)$$

with a scrape-off-layer envelope of $\Delta R_{SOL} = 60$ mm, specify the free-boundary equilibrium problem, along with the self-consistent treatment of the flux consumption estimates. The fiducial equilibria are summarized in figures 2–5.

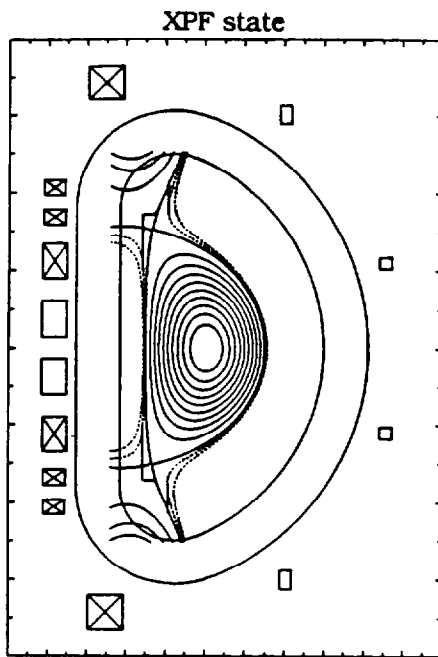
The shape conformity over the full-current portion of the scenario is very good — the triangularity variation is only $0.45 \leq \delta \leq 0.47$ — and the MHD safety factor is $q_{95} \approx 3.1$ for all the full-current states. Figure 6 shows the poloidal flux surfaces for the reference equilibrium — this shape is essentially unchanged over the burn phase.

The out-of-plane loads on the TF coils for the four fiducial states are plotted in Figure 7.

The coil currents at initial magnetization and the four fiducial states have been placed into a time scenario with a ramp-up time of 25s, a heating duration of 15s and a burn length of 120s, for the purposes of calculating the specific heating function, $\int J_{Cu}^2 dt$. The results are shown in Figure 8, where we see coil PF1 reaches a value of:

$$\int J_{Cu,PF1}^2 dt = 13.5 \times 10^{16} \text{ A}^2 \text{ m}^{-4} \text{ s}$$

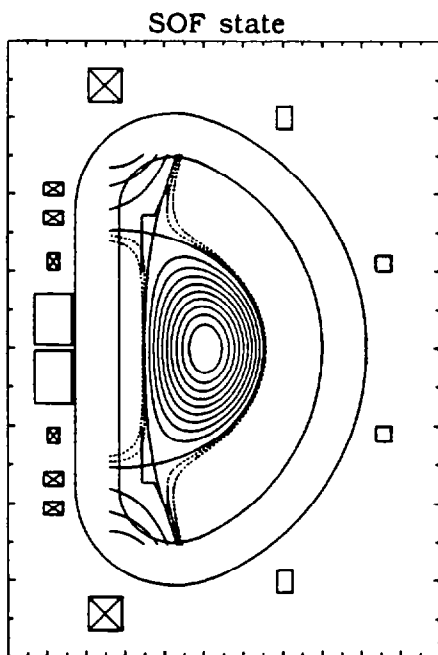
All other coils are below $5 \times 10^{16} \text{ A}^2 \text{ m}^{-4} \text{ s}$ at the end of the scenario.



R_0 (m)	5.00	a (m)	1.50
I_p (MA)	10.00	B_ϕ (T)	6.60
β_ϕ	0.22	β_N	0.22
ℓ_i	0.85	β_{pol}	0.10
q_0	1.17	q_{95}	4.72
κ_{95}	1.79	κ_x	2.03
δ_{95}	0.49	δ_x	0.90
R_{axis} (m)	5.04	Z_{axis} (m)	0.00
R_{ospt} (m)	3.96	Z_{ospt} (m)	± 3.96
R_{ispt} (m)	3.42	Z_{ispt} (m)	± 3.08
Ψ_{ext} (Wb)	-27.01	L_p (μH)	9.20
V (m^3)	408.31	A (m^2)	13.61

	NI	J_{pack}	B_{max}	F_R	F_R	$\frac{F_R}{\Delta Z_c}$
coil	MA	A/mm ²	T	MN	MN	MN/m
PF1	-18.20	-12.57	9.33	117	-344	81
PF2	16.44	11.35	10.37	316	319	219
PF3	6.88	9.86	10.13	186	-11	267
PF4	6.19	8.87	9.25	164	-52	234
PF5	23.27	15.29	9.69	684	-63	555
PF6	-4.50	-7.42	2.56	108	-10	111
PF7	-2.82	-7.24	1.89	47	3	75

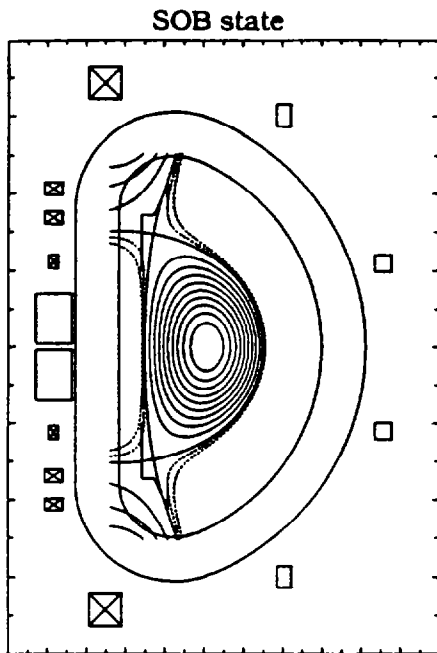
Figure 2 — Equilibrium at the x-point formation state.
Coil cross-sections drawn in proportion to their current.



R_0 (m)	5.00	a (m)	1.50
I_p (MA)	15.30	B_ϕ (T)	7.00
β_ϕ	0.47	β_N	0.32
ℓ_i	0.85	β_{pol}	0.10
q_0	.90	q_{95}	3.13
κ_{95}	1.77	κ_x	1.99
δ_{95}	0.47	δ_x	0.86
R_{axis} (m)	5.04	Z_{axis} (m)	0.00
R_{ospt} (m)	3.96	Z_{ospt} (m)	± 3.96
R_{ispt} (m)	3.42	Z_{ispt} (m)	± 3.03
Ψ_{ext} (Wb)	-93.14	L_p (μH)	9.25
V (m^3)	402.14	A (m^2)	13.35

	NI	J_{pack}	B_{max}	F_R	F_R	$\frac{F_R}{\Delta Z_c}$
coil	MA	A/mm ²	T	MN	MN	MN/m
PF1	-38.55	-26.62	24.30	1657	-918	1144
PF2	3.52	2.43	13.01	-28	108	-19
PF3	5.05	7.23	5.58	50	52	71
PF4	5.04	7.23	5.75	73	-7	105
PF5	21.69	14.25	8.56	445	-15	361
PF6	-6.84	-11.28	3.83	233	-40	240
PF7	-4.60	-11.78	3.04	113	2	181

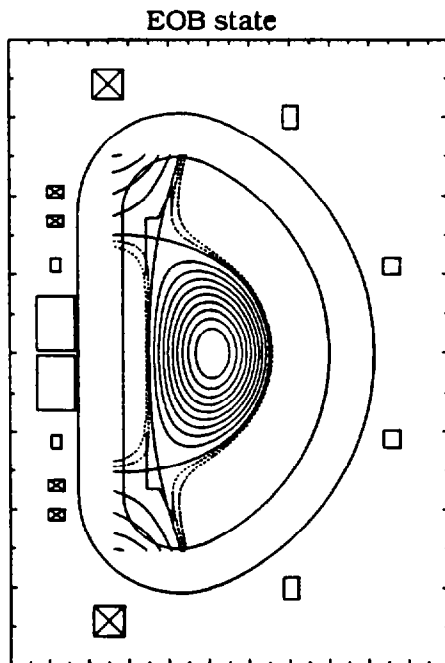
Figure 3 — Equilibrium at the start-of-flattop state.
Coil cross-sections drawn in proportion to their current.



R_0 (m)	5.00	a (m)	1.50
I_p (MA)	15.30	B_ϕ (T)	7.00
β_ϕ	2.34	β_N	1.60
ℓ_1	0.85	β_{pol}	.50
q_0	.90	q_{95}	3.13
κ_{95}	1.75	κ_x	1.96
δ_{95}	0.46	δ_x	0.86
R_{axis} (m)	5.08	Z_{axis} (m)	0.00
R_{ospt} (m)	3.96	Z_{ospt} (m)	± 3.96
R_{ispt} (m)	3.42	Z_{ispt} (m)	± 2.99
Ψ_{ext} (Wb)	-100.75	L_p (μ H)	9.55
V (m^3)	399.30	A (m^2)	13.25

	NI	J_{pack}	B_{max}	F_R	F_R	$\frac{F_R}{\Delta Z_c}$
coil	MA	A/mm ²	T	MN	MN	MN/m
PF1	-36.45	-25.17	23.11	1514	-805	1045
PF2	2.51	1.73	12.55	-22	72	-15
PF3	4.50	6.45	4.90	36	46	52
PF4	4.56	6.52	5.12	58	-3	83
PF5	20.62	13.56	8.10	392	-10	318
PF6	-6.28	-10.36	3.59	216	-44	223
PF7	-5.40	-13.84	3.54	151	-8	241

Figure 4 — Equilibrium at the start-of-burn state.
Coil cross-sections drawn in proportion to their current.



R_0 (m)	5.00	a (m)	1.50
I_p (MA)	15.30	B_ϕ (T)	7.00
β_ϕ	2.34	β_N	1.60
ℓ_1	0.85	β_{pol}	0.50
q_0	.90	q_{95}	3.10
κ_{95}	1.75	κ_x	1.96
δ_{95}	0.45	δ_x	0.85
R_{axis} (m)	5.08	Z_{axis} (m)	0.00
R_{ospt} (m)	3.96	Z_{ospt} (m)	± 3.96
R_{ispt} (m)	3.42	Z_{ispt} (m)	± 2.98
Ψ_{ext} (Wb)	-112.70	L_p (μ H)	9.55
V (m^3)	398.09	A (m^2)	13.20

	NI	J_{pack}	B_{max}	F_R	F_R	$\frac{F_R}{\Delta Z_c}$
coil	MA	A/mm ²	T	MN	MN	MN/m
PF1	-38.93	-26.89	25.44	1916	-814	1323
PF2	-2.52	-1.74	15.01	44	-73	30
PF3	3.27	4.69	3.32	3	43	4
PF4	3.57	5.12	3.36	24	7	35
PF5	17.36	11.41	6.63	231	6	187
PF6	-6.26	-10.34	3.57	212	-47	218
PF7	-5.46	-14.00	3.58	151	-9	242

Figure 5 — Equilibrium at the end-of-burn state.
Coil cross-sections drawn in proportion to their current.

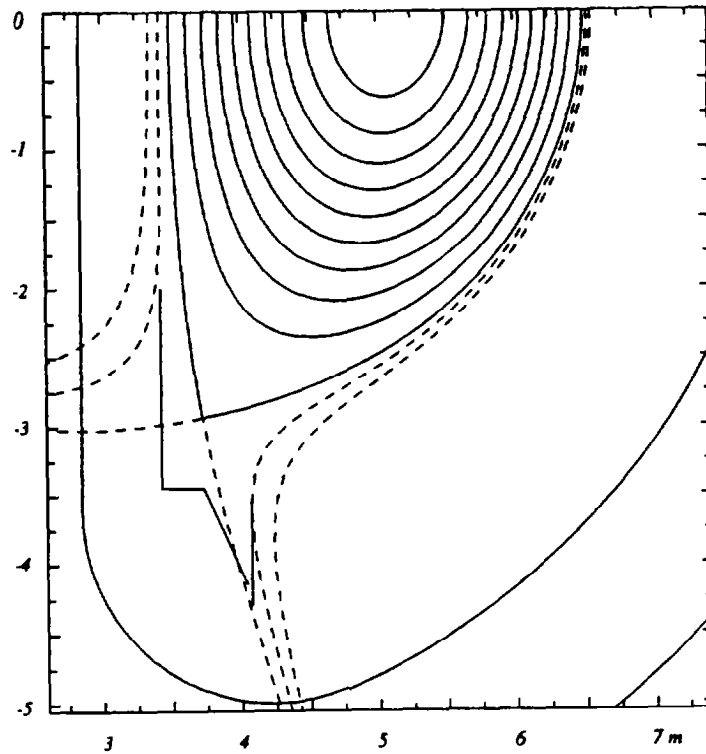


Figure 6 — Poloidal flux surfaces for the reference equilibrium.
 Field lines in the outboard SOL region map through $(R_0 + a + \Delta R, 0)$ with $\Delta R = 30, 60$ mm.
 Field lines in the inboard SOL region map through $(R_0 - a - \Delta R, 0)$ with $\Delta R = 75, 150$ mm.

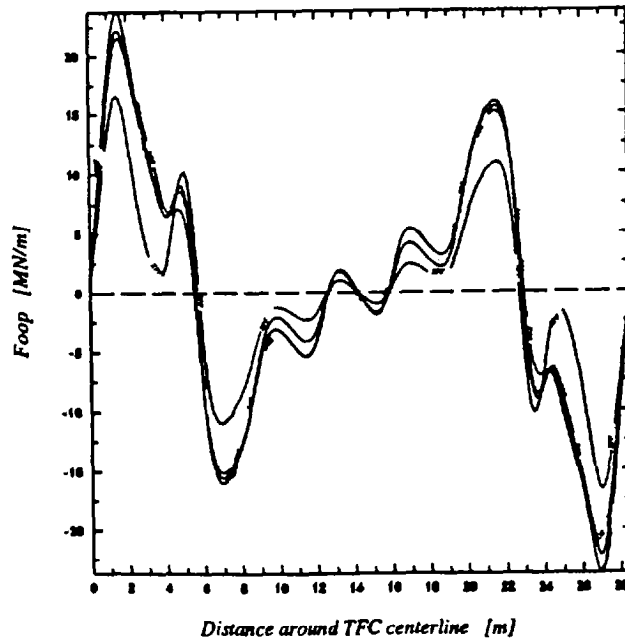


Figure 7 — Out-of-plane loads on the TF coils at the fiducial flux states.
 The distance is measured from the inboard midplane in a clockwise direction.

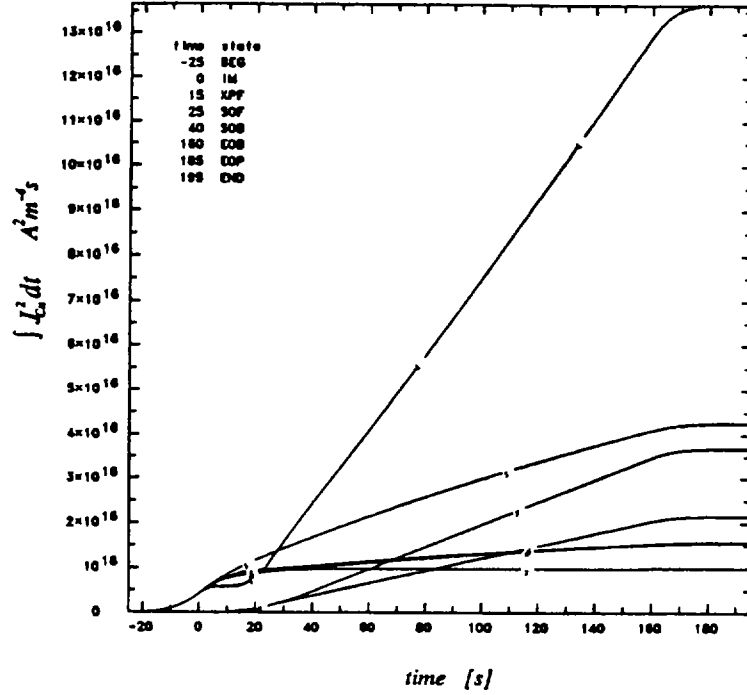


Figure 8 — $\int J_{Cu}^2 dt$ accumulation in coils PF1 – PF7 over the scenario with a solenoid (PF1 – PF4) thickness of $\Delta R_C = 1.00$ m.

Solenoid radial build tradeoff

In order to explore the solenoid radial build tradeoff, three sets of fiducial equilibria were generated with the following solenoid thicknesses:

$$\Delta R_{PF1-4} = 0.80, 1.00, 1.20\text{m}$$

all having an outer radius of 1.66m.

The significant differences between these three cases are summarized in Table 4.

Table 4 — Solenoid radial build sensitivity on PF1 performance.

ΔR_{PF1-4}	[m]	0.80	1.00	1.20
$\frac{F_R}{\Delta Z_c}$	[MN/m]	1133	1367	1588
$10^{-16} \int J^2 dt$	[A ² m ⁻⁴ s]	16.1	13.5	12.5

The intermediate case has been adopted as the baseline configuration, as described earlier. Coil parameters for the two variants are given in Tables 5 and 6.

Table 5 — Results with $\Delta R_{PF1-4} = 0.80$ m.

Initial magnetization state - $\psi_{ext} = 102$ Wb.

coil	NI	J_{pack}	B_{max}	F_R	F_Z	$\frac{F_R}{\Delta Z_c}$
PF1	24.27	20.95	20.37	1640	-9	1133
PF2	24.27	20.95	20.12	1601	-60	1106
PF3	11.70	20.95	18.97	725	-94	1039
PF4	11.70	20.95	17.32	659	-269	944
PF5	29.58	19.44	13.30	1522	-215	1236
PF6	-0.02	-0.03	0.21	0	0	0
PF7	0.41	-1.06	0.27	-1	-1	-2

X-point formation state - $\psi_{ext} = -29.2$ Wb.

coil	NI	J_{pack}	B_{max}	F_R	F_Z	$\frac{F_R}{\Delta Z_c}$
PF1	-16.01	-13.82	8.19	99	-318	68
PF2	13.45	11.61	8.51	238	277	165
PF3	5.64	10.11	8.27	143	-7	204
PF4	4.99	8.93	7.60	126	-40	180
PF5	23.04	15.14	9.56	662	-57	538
PF6	-4.58	-7.57	2.60	110	-11	114
PF7	-2.81	-7.22	1.88	47	3	75

Start-f-flatop state - $\psi_{ext} = -95.5$ Wb.

coil	NI	J_{pack}	B_{max}	F_R	F_Z	$\frac{F_R}{\Delta Z_c}$
PF1	-33.55	-28.96	20.88	1402	-836	968
PF2	2.02	1.74	12.09	-18	66	-13
PF3	3.99	7.14	4.34	32	46	45
PF4	3.96	7.09	4.55	52	-1	74
PF5	21.77	14.31	8.56	441	-9	358
PF6	-6.99	-11.54	3.91	240	-42	248
PF7	-4.57	-11.73	3.02	112	2	179

Start-of-burn state - $\psi_{ext} = -103.3$ Wb.

coil	NI	J_{pack}	B_{max}	F_R	F_Z	$\frac{F_R}{\Delta Z_c}$
PF1	-31.78	-27.43	19.92	1289	-735	890
PF2	1.15	1.00	11.65	-12	35	-8
PF3	3.53	6.32	3.78	22	41	31
PF4	3.56	6.37	4.01	40	2	58
PF5	20.73	13.62	8.11	388	-5	315
PF6	-6.46	-10.66	3.68	225	-46	232
PF7	-5.37	-13.77	3.53	149	-7	238

End-of-burn state - $\psi_{ext} = -114.7$ Wb.

coil	NI	J_{pack}	B_{max}	F_R	F_Z	$\frac{F_R}{\Delta Z_c}$
PF1	-33.83	29.20	21.86	1620	-740	1119
PF2	-3.06	-2.64	13.53	56	-94	39
PF3	2.51	4.50	3.38	-2	37	-3
PF4	2.77	4.95	2.62	15	9	22
PF5	17.64	11.59	6.72	235	9	190
PF6	-6.45	-10.65	3.66	221	-49	228
PF7	-5.43	-13.91	3.56	150	-8	239

Table 6 — Results with $\Delta R_{PF1-4} = 1.20$ m.

Initial magnetization state - $\psi_{ext} = 105$ Wb.

coil	NI	J_{pack}	B_{max}	F_R	F_Z	$\frac{F_R}{\Delta Z_c}$
PF1	33.23	19.13	27.86	2299	-10	1588
PF2	33.23	19.13	27.52	2243	-73	1549
PF3	16.02	19.13	25.81	1011	-116	1448
PF4	16.02	19.13	23.41	900	-329	1289
PF5	30.51	20.05	13.72	1618	-231	1314
PF6	-0.03	-0.05	0.22	0	0	0
PF7	0.43	1.09	0.28	-1	-1	-2

X-point formation state - $\psi_{ext} = -26.2$ Wb.

coil	NI	J_{pack}	B_{max}	F_R	F_Z	$\frac{F_R}{\Delta Z_c}$
PF1	-20.83	-11.99	11.06	147	-364	101
PF2	19.31	11.11	12.29	379	346	261
PF3	8.12	9.70	12.04	223	-12	320
PF4	7.40	8.83	10.98	196	-60	280
PF5	23.63	15.53	9.85	707	-66	574
PF6	-4.57	-7.54	2.59	110	-10	114
PF7	-2.80	-7.18	1.88	47	3	75

Start-f-flatop state - $\psi_{ext} = -92.5$ Wb.

coil	NI	J_{pack}	B_{max}	F_R	F_Z	$\frac{F_R}{\Delta Z_c}$
PF1	-44.24	-25.46	28.50	1937	-965	1338
PF2	4.12	2.37	14.32	-31	116	-22
PF3	5.95	7.10	6.71	62	57	90
PF4	6.03	7.20	6.87	90	-9	129
PF5	22.42	14.74	8.87	481	-17	391
PF6	-6.99	-11.53	3.90	241	-41	248
PF7	-4.56	-11.69	3.01	112	3	179

Start-of-burn state - $\psi_{ext} = -100.2$ Wb.

coil	NI	J_{pack}	B_{max}	F_R	F_Z	$\frac{F_R}{\Delta Z_c}$
PF1	-41.87	-24.10	27.12	1770	-849	1222
PF2	2.97	1.71	13.88	-25	78	-17
PF3	5.32	6.35	5.92	46	50	66
PF4	5.46	6.52	6.11	72	-5	103
PF5	21.40	14.06	8.42	427	-11	347
PF6	-6.46	-10.66	3.68	226	-45	232
PF7	-5.35	-13.73	3.52	149	-7	238

End-of-burn state - $\psi_{ext} = -111.7$ Wb.

coil	NI	J_{pack}	B_{max}	F_R	F_Z	$\frac{F_R}{\Delta Z_c}$
PF1	-44.59	-25.66	29.66	2208	-856	1524
PF2	-2.62	-1.51	16.83	44	-70	30
PF3	3.94	4.70	3.68	7	48	10
PF4	4.35	5.19	4.19	33	7	48
PF5	18.34	12.06	7.05	268	5	217
PF6	-6.45	-10.65	3.67	222	-48	228
PF7	-5.41	-13.87	3.55	149	-8	239

Advanced tokamak configuration

A 12MA high-beta reverse-shear tokamak configuration can be supported by the PF system of the *PCAST Machine*, as shown in Figures 9 and 10. This configuration has:

$$q_0 = 4.2, q_{\min} = 2.4, q_{95} = 3.6$$

It satisfies the same four shape constraints used for the fiducial equilibria, and can be sustained with reasonable coil currents.

The profile forms used for reverse-shear plasmas are, for the pressure:

$$p(\psi) = p(0) \left[(1 - \tilde{\psi})^2 + \varepsilon_p (1 - \tilde{\psi}) \tilde{\psi} \right]$$

with $\varepsilon_p = 0.05$, and for the parallel current density:

$$J_o(\psi) = J_o(0) \left[(1 - \tilde{\psi})^{\alpha_j} + \varepsilon_j (1 - \tilde{\psi}) \tilde{\psi} \right]$$

with $\alpha_j = 1$. The desired value of q_0 is achieved by adjusting the value of ε_j ($=2$).

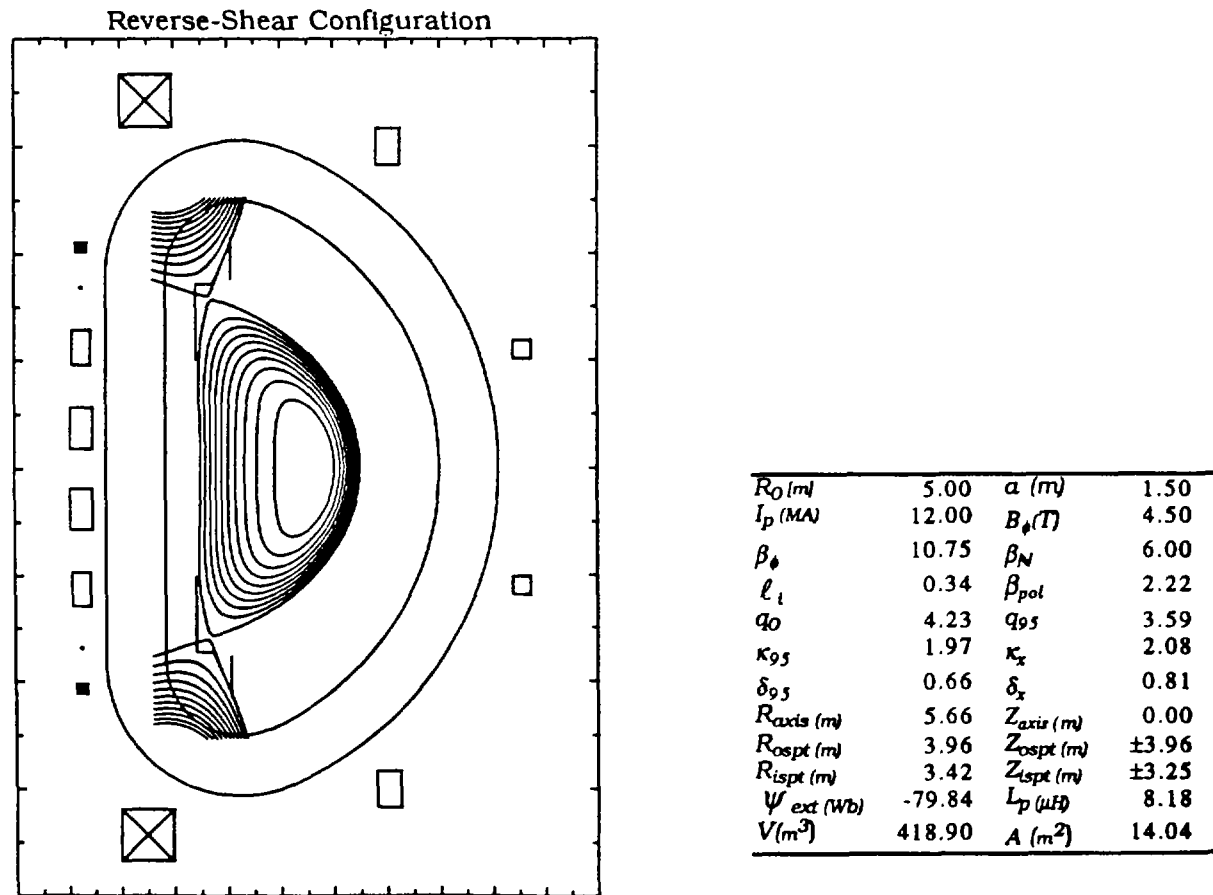


Figure 9 — Reverse-shear equilibrium in the *PCAST Machine*.

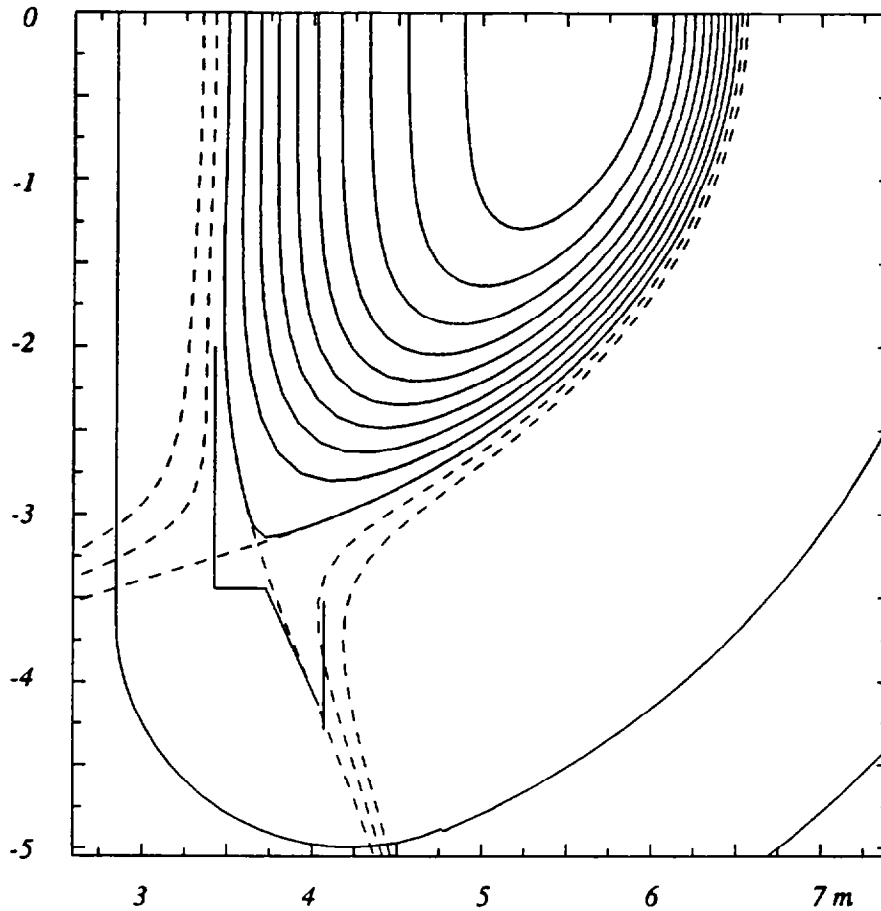


Figure 10 — Poloidal flux surfaces for the reverse-shear equilibrium.
 Field lines in the outboard SOL region map through $(R_0 + a + \Delta R, 0)$ with $\Delta R = 30, 60$ mm.
 Field lines in the inboard SOL region map through $(R_0 - a - \Delta R, 0)$ with $\Delta R = 75, 150$ mm.

References

- [1] S.C.Jardin, et al., "(BPX) MHD Equilibrium and Stability", *Fusion Technol.*, **21**, 1123 (1992)
- [2] S.C.Jardin, et al., "TPX Physics Design Description", 93-930325-PPPL/GNeilson-01, Princeton Plasma Physics Laboratory, (Mar. 1993)
- [3] S. Ejima, et al., "Volt-second Analysis and Consumption in Doublet III Plasmas", *Nuc. Fus.*, **22**, 1313 (1982)

1.2.5.b. Fast Position Control

C. Kessel (PPPL)

Vertical Stability

The elongation of the nominal plasma is 1.96 at the separatrix, so that the plasma is vertically unstable to the $n=0$ axisymmetric mode. The surrounding structure must provide some degree of slowing down or the plasma will move on an Alfvén time scale, making feedback control very difficult. The vacuum vessel, which includes a double wall geometry and outboard extensions toward the plasma, can provide this function with sufficient margin. The stability factor, which is a measure of this margin, is defined as $f_s = 1 + \tau_g/\tau_{L/R}$, where τ_g is the growth time for plasma vertical motion and $\tau_{L/R}$ is the longest time-scale up-down asymmetric mode induced in the structure. A stability factor of 1.0 corresponds to the plasma motion on an Alfvén time scale. The stability factor for the PCAST device is 1.25 for the most vertically unstable plasma condition, which occurs at the start of flattop. This good stability behavior is provided by the close proximity of the vacuum vessel over a large poloidal extent. The resulting growth time, for this same plasma, is 33.6 ms., assuming an Inconel 625 vessel at a temperature of 150 degrees C with a 4.45 cm thickness, resulting in a total toroidal resistance of 15 micro-ohms. This combination of stability factor and growth time provides reasonable requirements for vertical position feedback control to maintain the plasma position indefinitely. Since the vacuum vessel is sufficient, additional dedicated conducting structure is not required.

Vertical Position Control

Active vertical position control is achieved by a pair of coils on the outboard side of the plasma, located between the extensions and the plasma,

behind the first wall ($R=5.4$ m, $Z=\pm 2.4$ m). This location was chosen to take advantage of lower power requirements. Other locations were examined; between the extension and the vessel wall ($R=5.8$ m, $Z=\pm 2.8$ m) and just outside the outer vessel wall ($R=7.0$ m, $Z=\pm 3.6$ m). The analysis indicates that the power (MVA) requirements increase significantly as the coils move farther from the plasma and have more intervening structure. As an example, the resulting peak powers required for a 2 cm. step response were 10, 30, and 300 MVA, respectively, to provide a critically damped trajectory with a rise time of approximately the unstable plasma growth time (35 ms). The current and voltage requirements in the control coils were determined as those required to control a randomly fluctuating vertical position with a 1 cm rms excursions and a time-scale of 60 ms. This resulted in peak current and voltages of 100 kA-turns and 100 V/turn. The voltage was clamped at 100 V/turn for the simulation. The feedback control algorithm was a proportional-derivative law.

Radial Position Control

The plasma radial position control is achieved by a pair of coils on the outboard side of the plasma, located inside the vacuum vessel and just below the extensions ($R=6.6$ m and $Z=\pm 1.4$ m). These are separate from the vertical position coils because it reduces the power requirements and this location is better suited to providing vertical field. An ELM simulation is used to determine the maximum current and voltage in the coils, which consists of 20% reductions in the plasma stored energy every 500 ms, with reheating in between. The timescale is chosen to be a fraction of the energy confinement time to guarantee proper coupling to the ICRF antenna for heating. The

peak current required was approximately 200 kA-turns, and the peak voltage was 400 V/turn. The feedback control algorithm was a proportional only law.

1.2.5.c. Plasma Initiation

P-W Wang (MIT)

The PF system must be capable of producing a peak loop voltage of 15V in the absence of plasma breakdown. Breakdown occurs when the loop voltage reaches 15 V and a field null (which must be unique within the vessel) exists. The null is centered at $(R, Z) = (6.0 \text{ m}, 0.0 \text{ m})$ and its magnitude $|B_p| < 2.5 \text{ mT}$ within a 0.5 m radius. Following breakdown, the vertical field is ramped on, with a time derivative that is matched to the current rise rate. The field index $[n = -(R/B_z)(dB_z/dR)]$ is maintained in the range 0.2 to 1.0 to provide vertical and horizontal stability. Feedback control of the plasma current and radial equilibrium is established when the plasma current reaches 100 kA. Besides satisfying the physics requirements, the engineering constraints also need to be considered, including the coil voltages, currents, flux consumption, eddy currents, and power system requirements.

The startup scenario is divided into three general phases, charge, blip, and current rise. The charge time is assumed to be 50 seconds (from $t = -50 \text{ s}$ to 0 s). Seven pairs of copper PF coils are charged, at constant voltage, to their pre-blip values of current to produce a 108 Wb pre-blip flux bias for the PCAST machine. Coil positions and builds are shown in Table 1. Coil currents and voltages (per coil) at $t = 0^- \text{ s}$ are listed in Table 2. Number of turns for each coil is still to be determined. One constraint will be that the coil voltage can not exceed the maximum voltage that a coil is designed for, for example 20 kV. The internal control (IC) coils are not included in this scenario, but could be employed if desired.

Table 1. Coil centroid positions (R_c, Z_c) and builds (DR, DZ).

Coil	PF1	PF2	PF3	PF4	PF5	PF6	PF7
R_c (m)	1.230	1.230	1.230	1.230	2.483	7.036	9.566
Z_c (m)	± 0.750	± 2.250	± 3.375	± 4.125	± 6.960	± 6.012	± 2.204
DR (m)	0.800	0.800	0.800	0.800	1.118	0.712	0.712
DZ (m)	1.450	1.450	0.700	0.700	1.118	1.118	1.118

The blip phase requires that the (open) loop voltage in the vacuum chamber rises as rapidly as possible to 15 V to breakdown and initiate a plasma, Fig. 1. This loop voltage is induced by a rapid change in the PF coil currents with constant voltage change, Table 2, in seven independent PF coil circuits. The blip time period is 0.388 seconds. A significant amount of eddy current is induced in the axisymmetric vacuum vessel, 1.1 MA at the end of the blip. The vacuum vessel has a total equivalent resistance of 15 m Ω . The flux consumption for this phase is 3.6 Wb as shown in Fig. 1.

Table 2. Summary of coil currents and voltages at the end of the three phases, charge ($t = 0^-$ s), blip ($t = 0.388$ s), and current rise ($t = 0.688$ s).

Coil		PF1	PF2	PF3	PF4	PF5	PF6	PF7
Current NI (MA-t)	$t=0$	26.3	25.7	17.2	16.2	26.6	0.58	0.38
	0.388 s	24.2	27.5	14.3	13.8	24.8	0.24	0.33
	0.688 s	23.0	27.8	14.2	13.8	24.6	0.40	0.32
Voltage V/N (V/t)	$t=0^-$ s	3.90	3.80	5.00	4.65	7.38	2.15	2.29
	0.388 $^-$ s	-7.45	0.00	-17.8	-18.8	-23.0	-31.3	-17.9
	0.688 $^-$ s	-6.29	1.17	1.60	2.01	2.28	5.33	-6.18

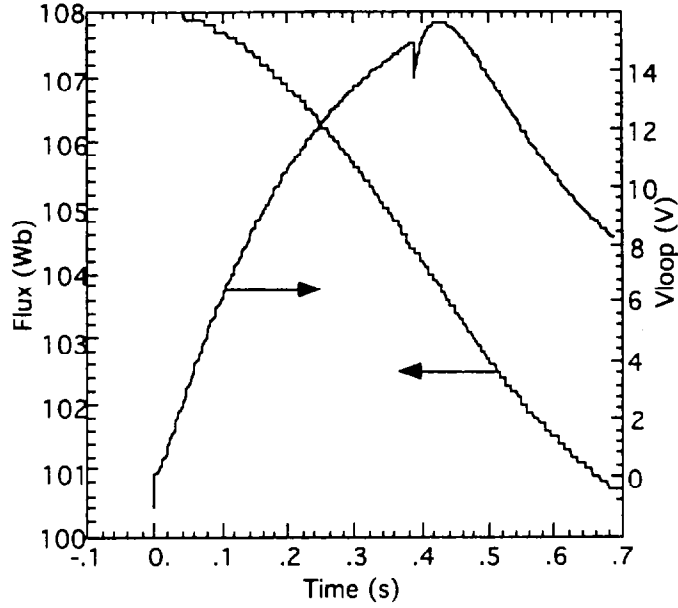


Fig. 1 : Poloidal magnetic flux and loop voltage at $R = 6.0$ m versus time. Breakdown occurs at $t = 0.388$ s.

The PF coil system also needs to maintain a magnetic field null within a large region inside the vacuum vessel, taking into account the influence of the eddy currents, during the plasma breakdown period. The quality of this field null is crucial to the following avalanche phase. The null at the breakdown is centered at $(R, Z) = (6.0 \text{ m}, 0.0 \text{ m})$ with the vertical magnetic field $|B_{\perp}| < 2.5 \text{ mT}$ over a range of $4.6 \text{ m} < R < 6.5 \text{ m}$ (outer limiter), Fig. 2. The duration of the null lasts over 0.2 s before the breakdown. The electric field E is

$$E = \frac{V_{loop}}{2\pi R} \leq 0.4 \text{ V/m} .$$

The connection length L is

$$L \approx \frac{a_{null} B_{\phi}}{B_{\perp}} = \frac{0.5 \text{ m} \times 7 \text{ T}}{5 \times 10^{-4} \text{ T}} = 7,000 \text{ m}$$

The radius of the null, a_{null} , is 0.5 m and, at this radius, the average vertical field is about 0.5 mT. The combination of the electric field and the connection length should enable a reliable plasma startup. This is because the field null quality obtained is very good. A requirement of $|B_{\perp}| < 2.5$ mT over $a_{\text{null}} = 0.5\text{m}$, which gives $L = 1,400$ m, is adequate for the PCAST machine.

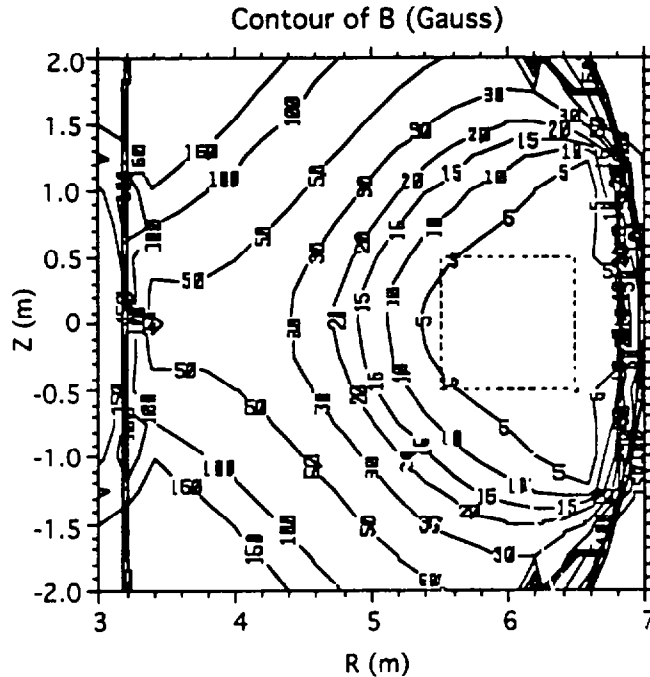


Fig. 2 : $|B_p|$ -field [Gauss] contours at the breakdown, $t = 0.388$ s.

The plasma current rise phase requires the system to maintain the vertical field necessary to maintain the plasma in equilibrium against radial motion and to provide field gradient consistent with vertical and horizontal stability throughout the phase, until the feedback control system can take over. The feedback of the horizontal field measured by the flux loops for vertical position control is assumed to be established at the plasma current of 100 kA. The current ramp rate of 0.33 MA/s is obtained assuming that the resistive plasma voltage starts at the breakdown loop

voltage and decays exponentially with a time constant of 0.1 s. The duration of this phase is 0.3 s. Coil currents and voltages at the end of this phase are listed in Table 2. The flux consumption is 3.7 Wb.

The PCAST machine is capable of producing breakdown centered at $(R,Z) = (6.0 \text{ m}, 0.0 \text{ m})$ with an electric fields of 0.4 V/m while maintaining a field null below 2.5 mT over a radius of 0.5 m with a maximum one-turn voltage of 31.3 V in PF6. The duration of the existence of the field null is also kept long, 0.2 s. An initial current ramp rate of 0.33 MA/s is obtained. The total flux consumption during this sequence is about 7.3 Wb.

1.2.5.d. Reference Discharge Simulation C. Kessel (PPPL)

We have developed a self-consistent simulation of the reference ignited plasma discharge from rampup through rampdown. The target flat-top plasma parameters are those for the Reference Operating Point obtained by static zero-dimensional analysis in Section 1.1. The simulation is done with the Tokamak Simulation Code (TSC), a two-dimensional, time dependent, free boundary simulation code that advances the MHD equations describing the transport time-scale evolution of an axisymmetric magnetized tokamak plasma. The TSC evolves the magnetic field in a rectangular computational domain using the Maxwell-MHD equations for the plasma and passive structure, coupled through boundary conditions to the circuit equations for the tokamak poloidal field (PF) coils. The plasma model in TSC was prescribed by providing functional forms for the electron and ion thermal conductivities, and for the plasma electrical resistivity. Thus, TSC evolves 2D variables for the magnetic poloidal flux and toroidal field, but utilizes flux coordinate mappings to solve 1D equations for the surface averaged temperatures and densities. In addition, the model includes separate energy equations for electrons and ions, neoclassical resistivity, bootstrap current, a time-averaged sawtooth model, the Coppi-Tang transport model, and radiation from impurities, bremsstrahlung, and cyclotron emission. The plasma density is not evolved in time, but is given by the prescribed function, $n(x,t) = n(0,t)[(1-x^b)^a + n_a(t)]$, where $n(0,t)$ is the central density, $n_a(t)$ is the normalized density at the plasma edge, and x is the normalized radial coordinate in the plasma. $n(0,t)$ is specified as a piecewise linear function of time, and the exponent values for the density profile are taken to be $b=2.0$, $a=0.5$, and $n_a(t)=0.4$. The thermal helium density profile is assumed to have

the same shape as the electron density profile, and the particle balance in the plasma is consistent with charge neutrality. The density limit is monitored throughout the discharge with respect to the Murakami, Greenwald, and Borrass limits. A 2% carbon impurity is assumed throughout the discharge.

The inclusion of passive structures in discharge modeling is critical in obtaining accurate estimates of the volt-second consumption and response to feedback systems. The passive structure model includes the double walled vacuum vessel with the outboard extensions toward the plasma. The total toroidal resistance is 15 micro-ohms. Since TSC must begin its simulation with a plasma present, a constant voltage is set as the initial condition over the entire computational grid. This causes finite currents to exist in the structures at the beginning of the simulation, as would be expected after the breakdown phase. The layout of the poloidal field (PF) coils, structure, and plasma for the TSC simulations is shown in Fig. 1. Feedback systems are used in the simulations to control the plasma radial position, total current, and shape.

The basic features of the PCAST discharge simulations are described in this section. The discharge can be broken up into four phases: plasma current rampup (0-25 s), initial heating and density rise (25-40 s), flat-top (40-160 s), and plasma cooling and current rampdown (160-200 s). Two scenarios are simulated, differing in the method uses to control the initial burn transient. In the Density-Ramp Scenario (Figs. 2-5) a 50-50 mixture of DT fuel is assumed and the density is gradually increased throughout both the heating and flat-top phases. In the Fuel-Mixture Ramp Scenario (Figs. 6-9), the density is ramped up to its steady state value in the heating

phase, while the D:T fuel ratio is ramped up gradually. In both scenarios, the goal is to raise the fusion power output with minimum overshoot, and then maintain it at an approximately constant level for 120 s.

Plasma Current Rampup

The plasma starts as a circular 250 kA plasma limited on the outboard side of the tokamak ($R=5.7$ m, $a=0.8$ m) and is grown to full size and shape. The plasma current is ramped at a constant rate to achieve 15.3 MA in 25 seconds. The plasma becomes diverted between 15 and 20 seconds. The volume average electron density increases linearly during this phase to 0.35×10^{20} m⁻³. Only ohmic heating takes place in this phase, and reaches a maximum value of 10 MW. The total flux consumption for rampup is 170 V-s, with 8 V-s resistive, 62 V-s internal inductive, and 100 V-s external inductive using the axial flux accounting method.

The important issues to examine in the plasma current rampup phase of the discharge are internal inductance $l_i(t)$, safety factor $Q_{95}(t)$, poloidal flux consumption, and PF coil voltages. Previous work demonstrated that there is a critical current rampup time, set by the time it takes for current to diffuse into the ohmically heated plasma. Ramping the current up faster than this critical time does not reduce flux consumption, but can lead to degraded MHD stability.

The MHD stability of the rampup phase stands out as the primary constraint for this region of the discharge. Non-beta limiting instabilities dominate the discharge during plasma current rampup and rampdown. A diagram displaying the discharge trajectory in l_i and Q_{95} , which is based on

zero pressure resistive and ideal MHD stability analysis, has shown particular promise for evaluating the MHD stability in these discharge phases, Fig. 3. The upper boundary, corresponding to peaked current profiles, is correlated with resistive instabilities. Density limit disruptions typically involve a peaking of the current profile and a crossing of this upper boundary.

The sawtooth-shaped boundary of the diagram represents surface kink modes. These are most unstable when the value of the safety factor at the plasma edge just exceeds an integer value. The unstable region to the left in the diagram is associated with the low values of q_{95} , less than 3.0, and the corresponding difficulty with obtaining any stable current profiles in this range.

For the 25 second plasma current rampup the value of $l_i/2$ drops to a minimum value of 0.38, while its steady state value is 0.45. This causes it to drop slightly into the unstable region at a q_{95} value of 4.0. In addition, it is desirable to have a well developed sawtooth during the rampup before heating, indicated by a large $q=1$ radius. This is not achieved and leads to expansion of the sawtooth radius in flattop which causes a core thermal drop. Both of these issues could be avoided by extending the rampup time by roughly 5-10 seconds. The 25-s rampup is obtained with less than 15 V/turn on all PF coils, and an Ejima coefficient of 0.3. Both scenarios have the same current ramp-up trajectory.

Initial Heating and Density Rise

At the end of the plasma current rampup phase 40 MW of auxiliary heating is applied for 15 seconds. The plasma stored energy rises to approximately 250 MJ during this time, and the fusion power output increases to over 400 MW. The volume average plasma electron density increases linearly to $0.75 \times 10^{20} \text{ m}^{-3}$ and $1.25 \times 10^{20} \text{ m}^{-3}$ for the density-ramp and the fuel-mixture ramp scenarios, respectively. The volume average plasma temperatures reach approximately 15 keV and 11 keV, respectively. For the fuel-mixture ramp scenario the tritium fraction is 0.15 in this phase. The helium density has barely begun to accumulate in this phase, since the particle confinement time is approximately 10 times the energy confinement time. By the end of this phase, the plasma β is about 2.2%, corresponding to a β_N of 1.5. In addition, the alpha input power to the plasma is 90 MW. The combination of auxiliary and alpha power match the criterion to enter to H-mode for 10 of the 15 seconds in this phase. Only 2.5 V-s are consumed.

In this phase of the discharge the approach to ignition is initiated by simultaneously ramping up the plasma density and applying auxiliary heating. The phasing of density and total input power to the plasma (auxiliary plus alpha) is done in such a way as to trigger the L to H mode transition.

Burning Plasma Flat-top

The flat-top burn phase is an ignited phase as the auxiliary heating is reduced to zero. For the density ramp scenario, the plasma density is ramped up to control the fusion power. The volume average density is ramped piecewise linearly to $1.25 \times 10^{20} \text{ m}^{-3}$. The helium content reaches its final

value only at the very end of the flat-top because of its long confinement time and the slow plasma density rampup. For the fuel mixture ramp scenario the density remains constant during flattop while the tritium fraction is increased to control the fusion power. The tritium fraction is ramped piecewise linearly from 0.15 to 0.49, as shown in Fig. 9. This phase lasts from the end of the heating at 40 seconds to the beginning of the cooling and rampdown phase phase at 160 seconds. The final volume average helium concentration is 12% of the electron density. During the burn the plasma consumes approximately 8 V-s of poloidal flux, corresponding to an average loop voltage of 0.085 V. The plasma volume average temperatures drop to 9 keV by the end of flattop for both scenarios. It is not clear whether sufficient power is being supplied to maintain the H-mode; this is discussed in more detail in Section 1.2.2.

The gradual density rise is required to maintain constant fusion power as the helium accumulates and dilutes the fuel. The helium ash is taken to have the same density profile shape as the electrons, as is experimentally observed in tokamaks. The plasma stored energy remains roughly constant at approximately 250 MJ, with a plasma β of 2.2%, corresponding to β_N of 1.5. The alpha power into the plasma is 85 MW, and the energy confinement time is about 4.5 seconds. Auxiliary power could be used to control the small excursions in fusion power shown in Figs. 5 and 9; however, no burn feedback control was used in these simulations.

Plasma Cooling and Current Rampdown

The plasma must be cooled during the current rampdown to avoid large negative currents at the plasma edge. The cooling phase begins by

reducing the plasma density, which is done on a particle confinement time scale, taken here to be approximately 30 seconds. This precipitates a drop in the alpha heating so the plasma is no longer ignited. The plasma current is ramped down in this phase from 15.3 MA to 0.25 MA. During this period the plasma is moved to the outboard limiter and reduced in size simultaneously with the plasma current being decreased. The rampdown phase lasts for approximately 50 seconds. The toroidal magnetic field is also ramped down in this phase, from 7.0 T to 4.5 T, but q_{95} is kept above 3.0. The volume average temperatures drop to below 2 keV.

During the plasma current rampdown the MHD stability becomes the primary constraint on the ramp rate, as in the current rampup phase. The l_i versus q_{95} diagram is the guide for creating stable rampdown trajectories. The process of plasma current rampdown always results in the increase of l_i as time proceeds, and the plasmas become vulnerable to resistive MHD instabilities. It is crucial to avoid this event until the plasma current is very low. Thus, the value of q_{95} must be increased simultaneously with l_i in order to avoid this region of unstable operating space.

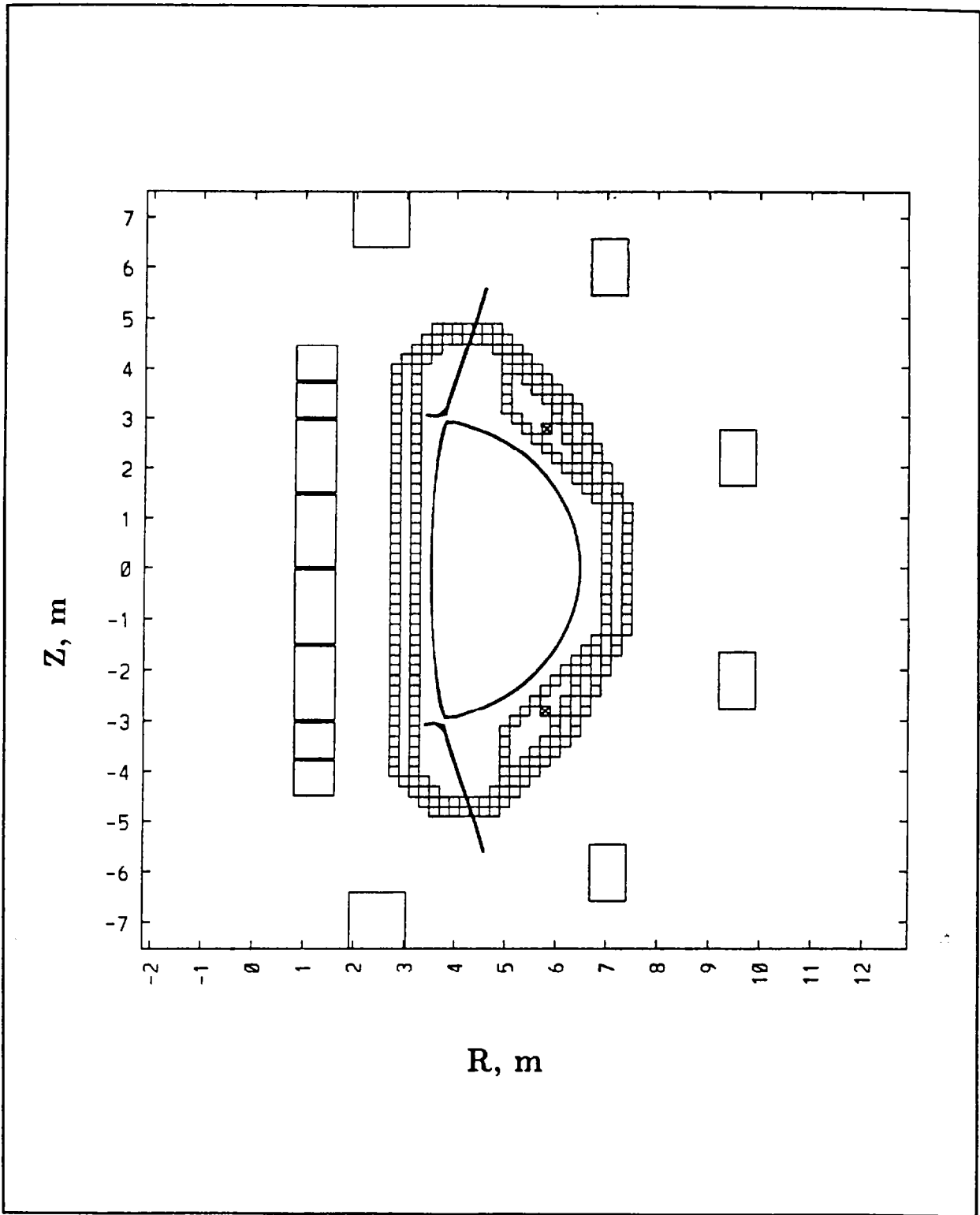


Fig. 1. Layout of poloidal field coils, vacuum vessel structure, and flat-top plasma used in TSC discharge simulations of the PCAST device.

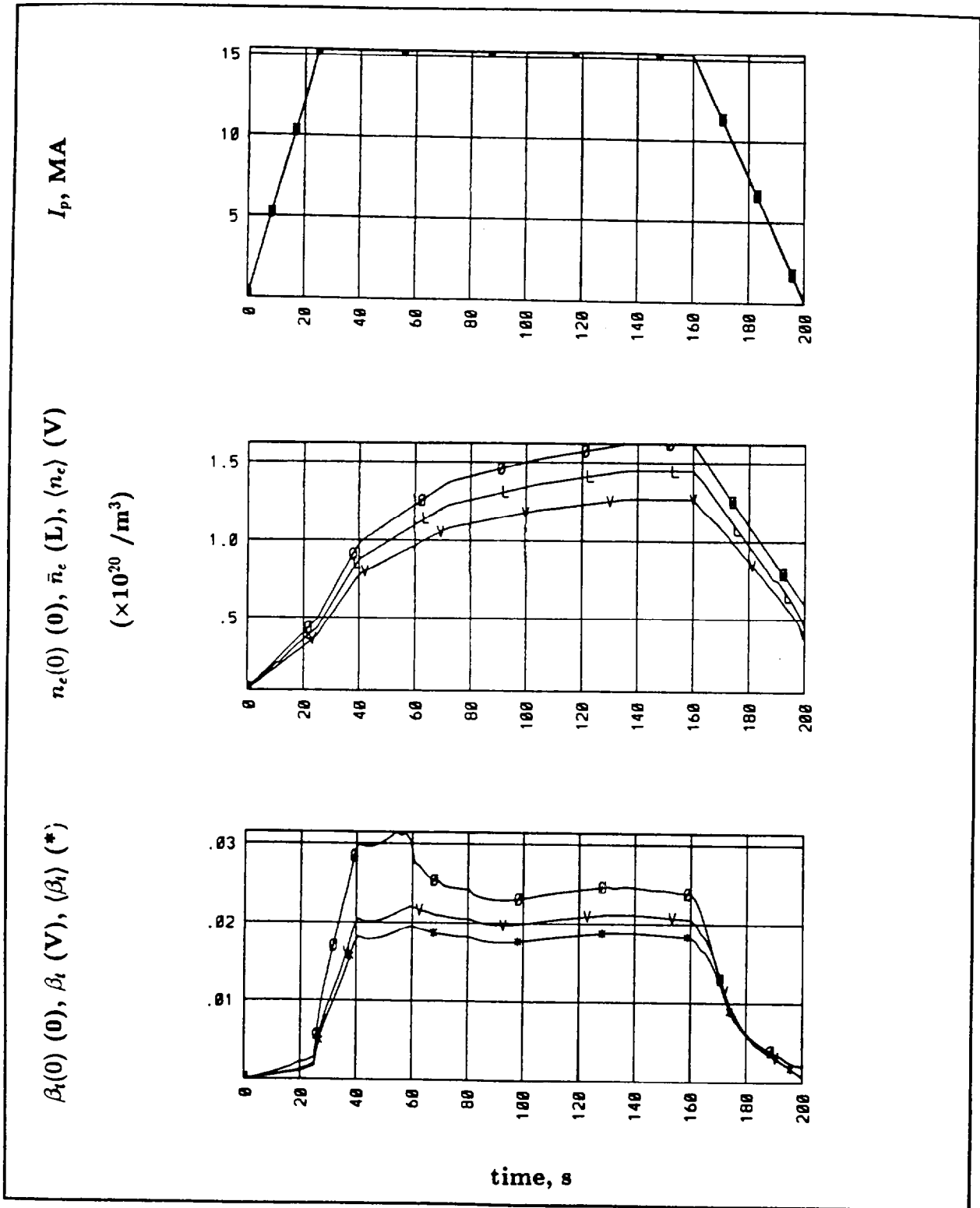


Fig. 2. Time histories of the total plasma current, toroidal β , and electron density throughout the discharge for the density-ramp scenario.

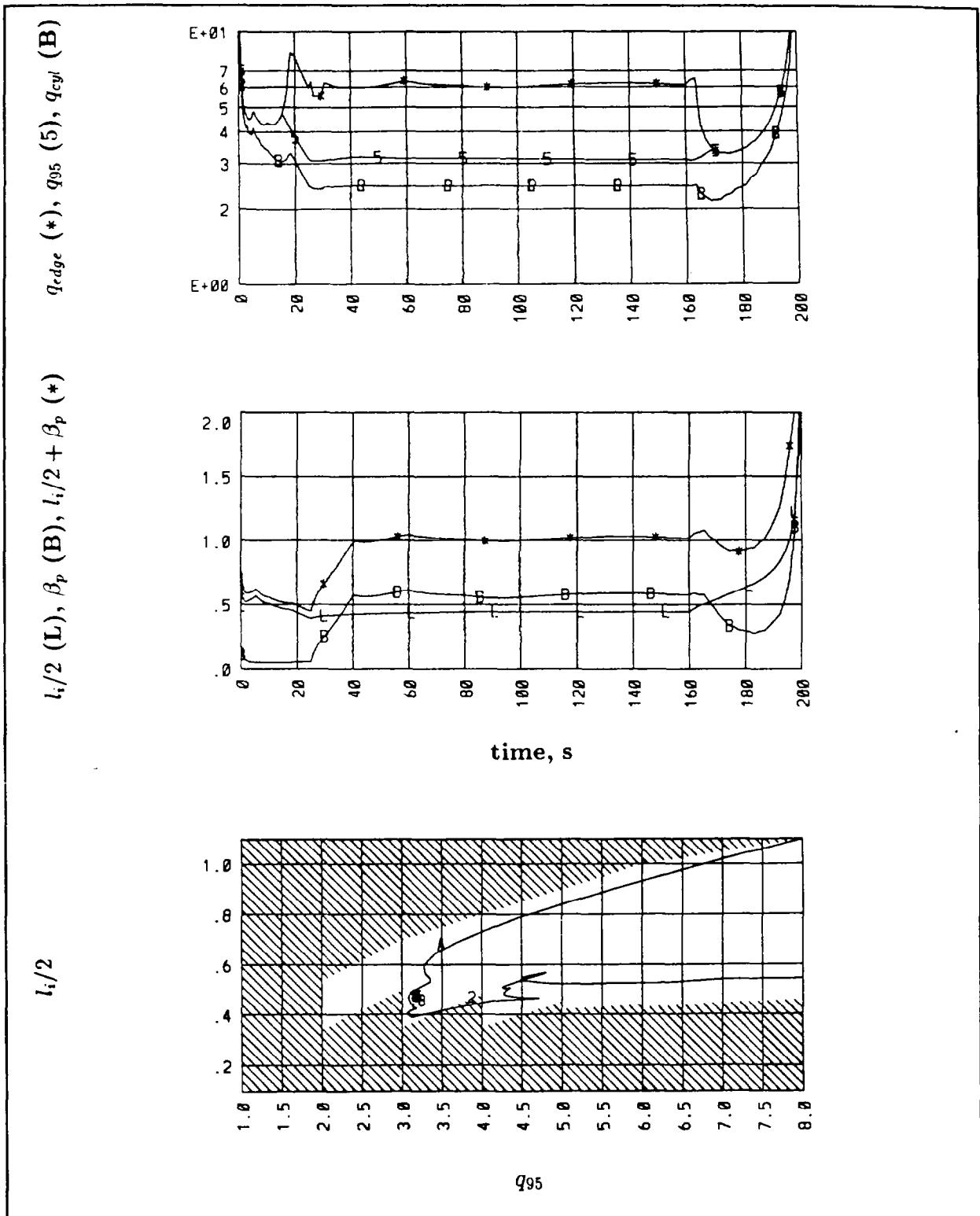


Fig. 3. Time histories of the safety factor, poloidal β and internal inductance (l_i), and $l_i/2(t)$ versus $Q_{95}(t)$ throughout the discharge for the density-ramp scenario.

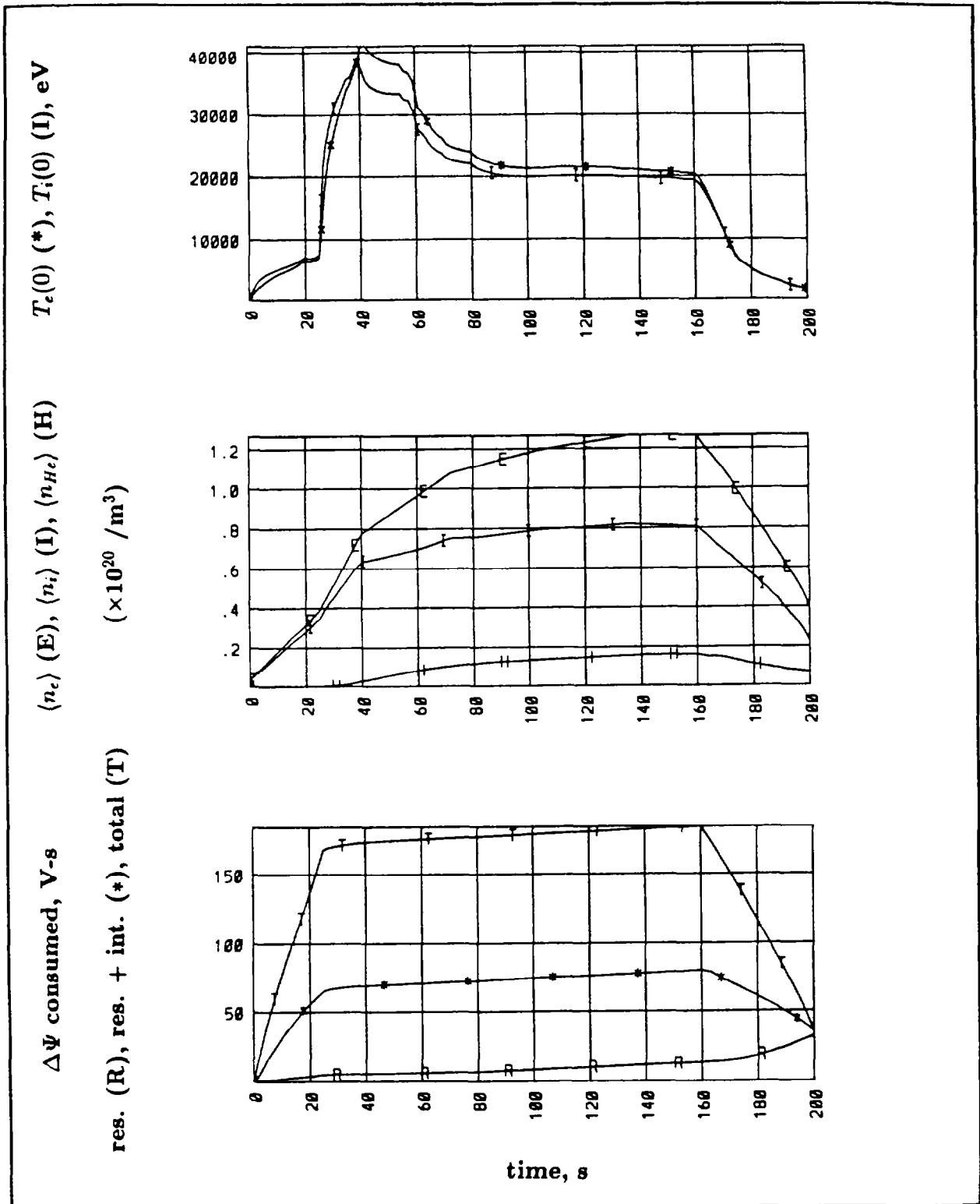


Fig. 4. Time histories of the plasma peak temperatures, poloidal flux consumption, and value average densities (including helium) throughout the discharge for the density-ramp scenario.

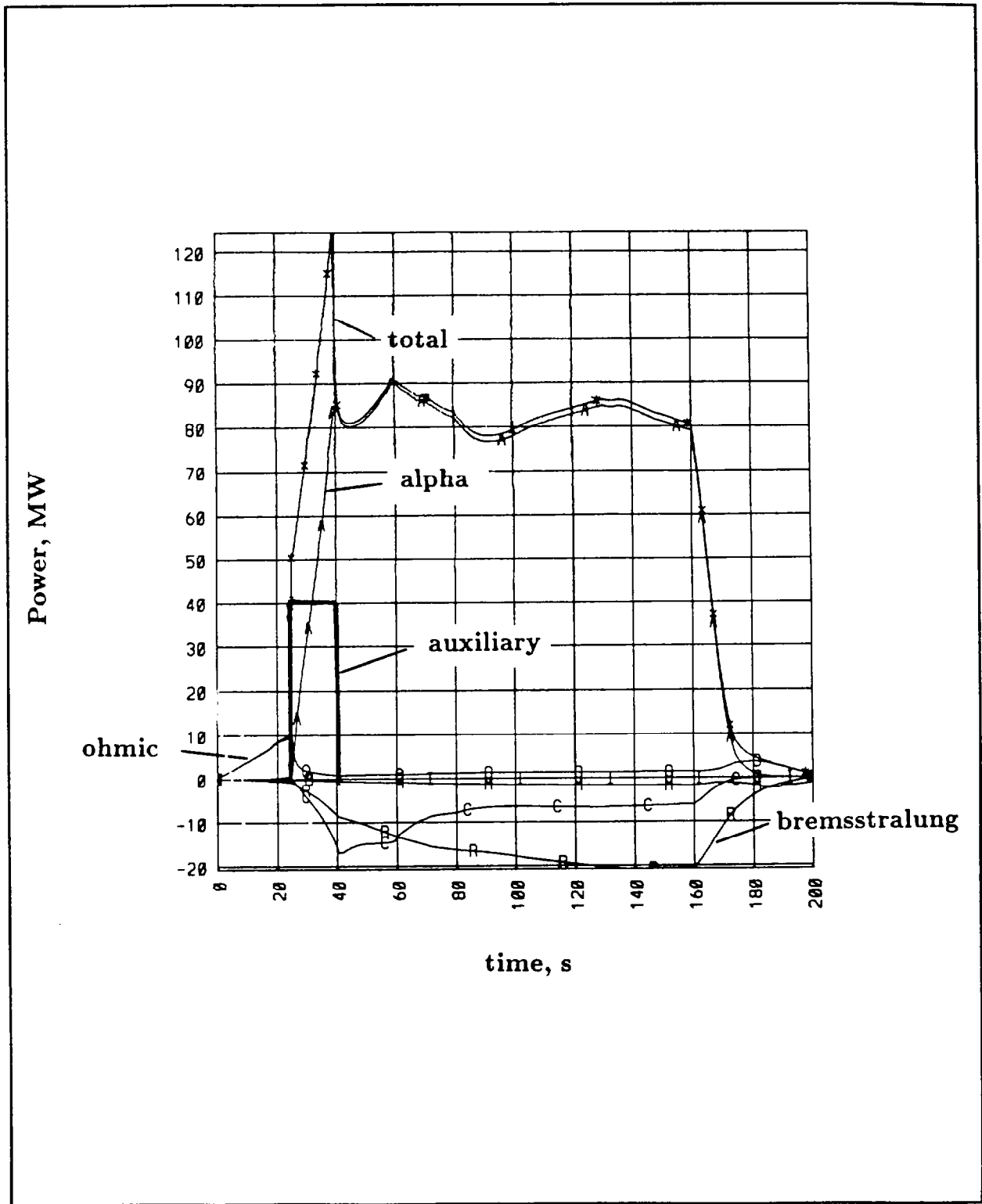


Fig. 5. Time history of the various powers throughout the discharge for the density-ramp scenario.

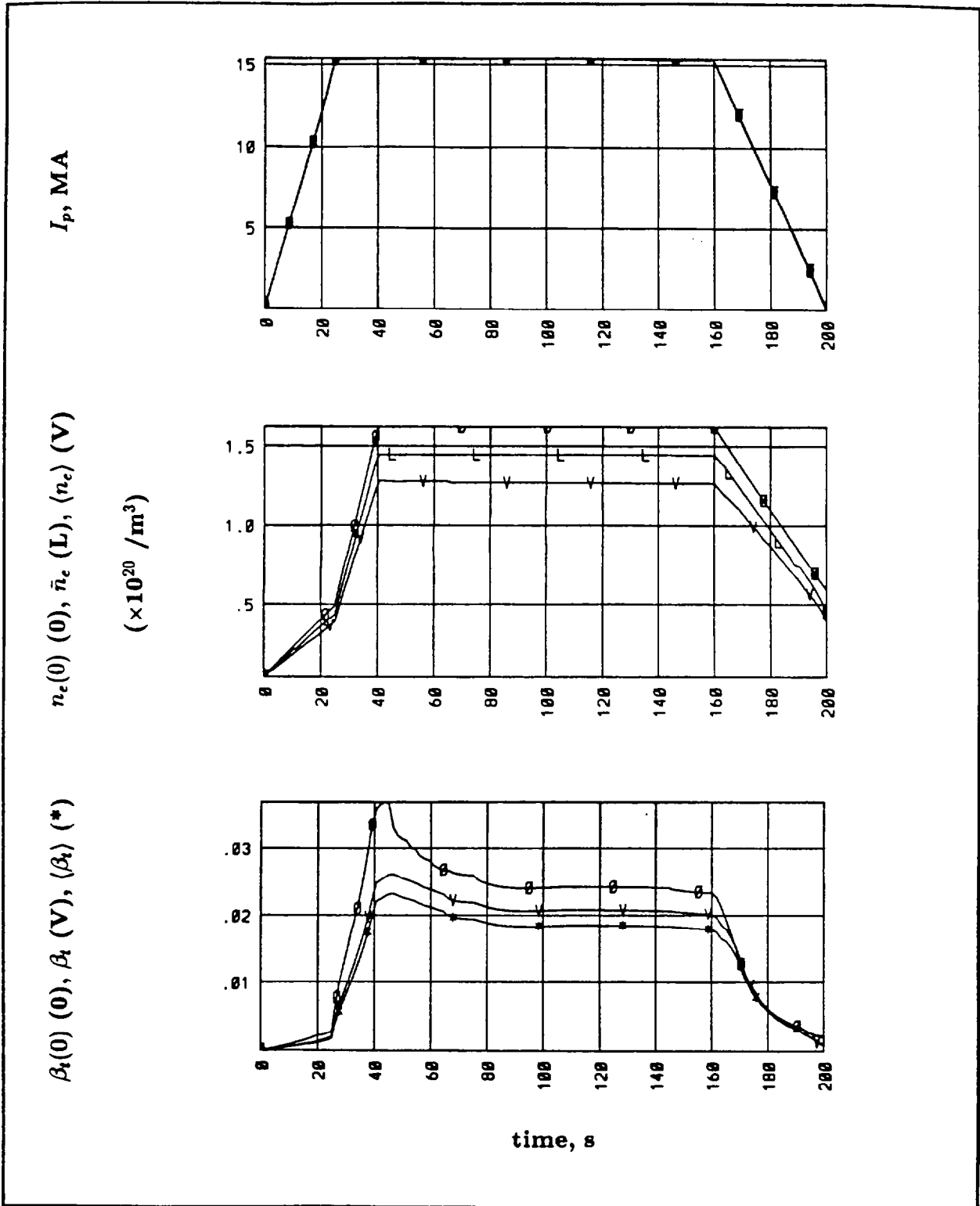


Fig. 6. Time histories of the total plasma current, toroidal β , and electron density throughout the discharge for the fuel-mixture ramp scenario.

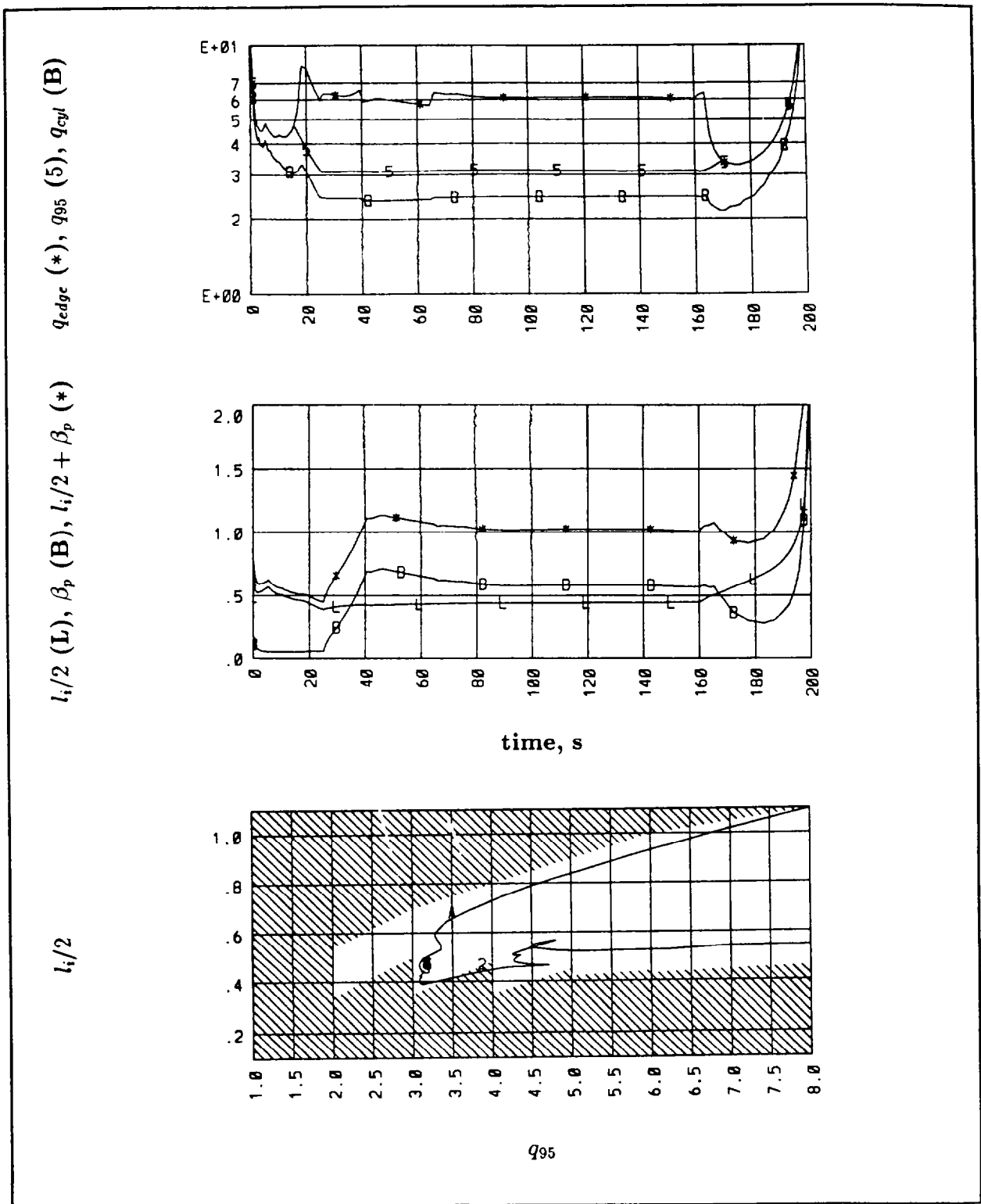


Fig. 7. Time histories of the safety factor, poloidal β and internal inductance (l_i), and $l_i/2(t)$ versus $Q_{95}(t)$ throughout the discharge for the fuel-mixture ramp scenario.

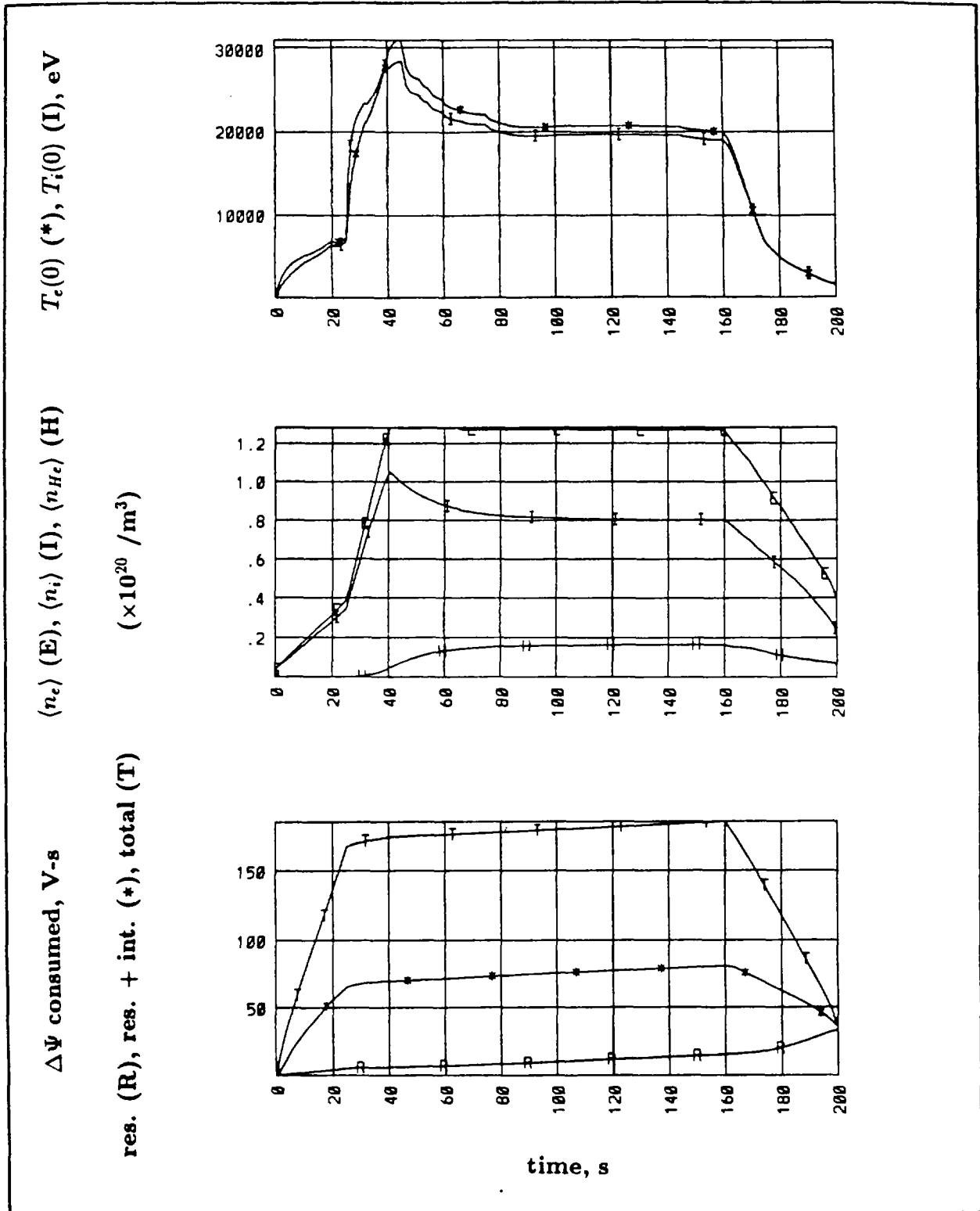


Fig. 8. Time histories of the plasma peak temperatures, poloidal flux consumption, and value average densities (including helium) throughout the discharge for the fuel-mixture ramp scenario.

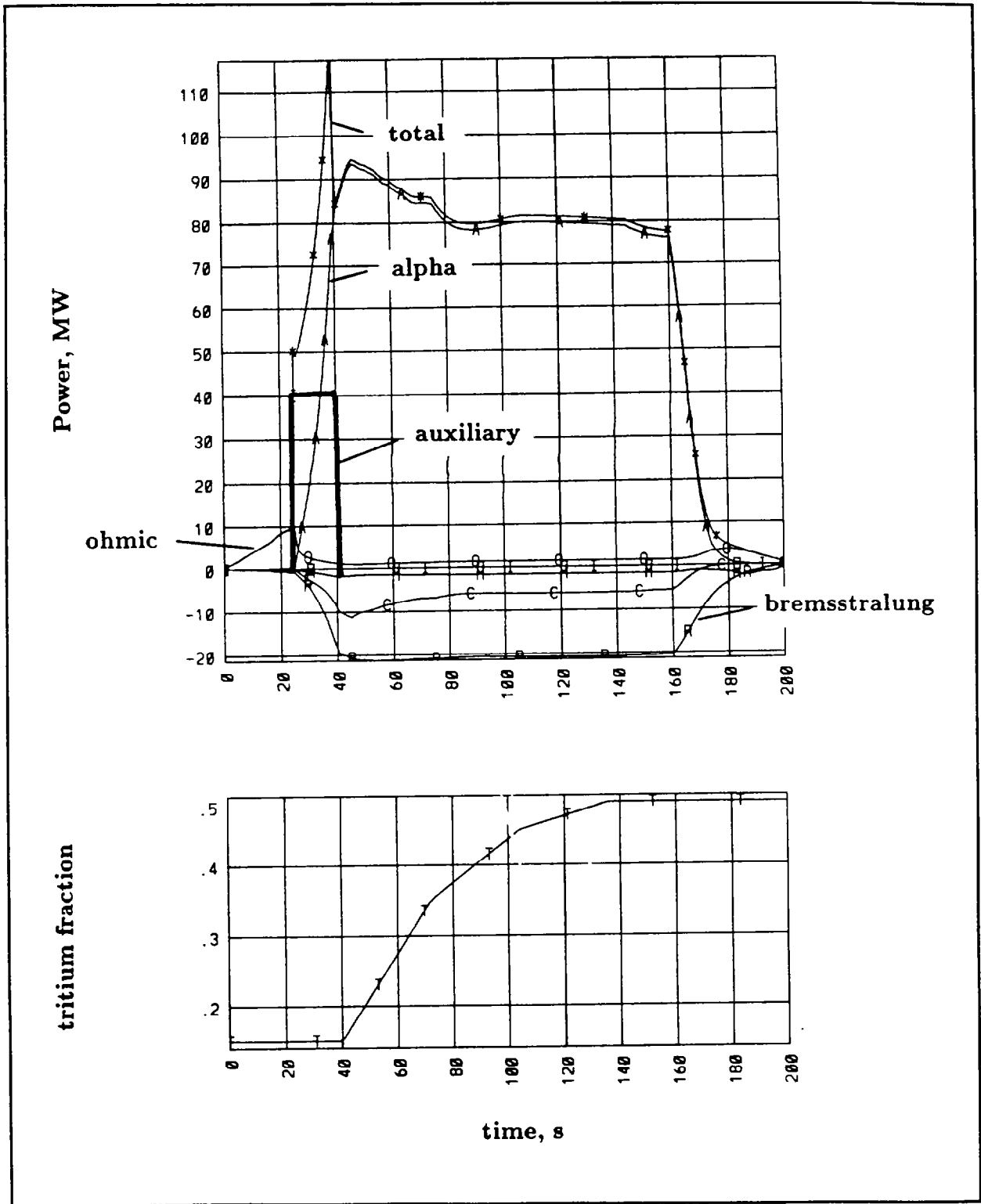


Fig. 9. Time history of the various powers throughout the discharge for the fuel-mixture ramp scenario.

1.2.6. Divertor and First Wall

D. Hill (LLNL)

1.2.6.1 PFC Configuration

Power and particle handling in this machine will be accomplished using a double-null poloidal divertor. The double-null configuration is compatible with the desire to have high triangularity to increase the plasma current and has the added benefit of reducing the power handling and particle control requirements at the inner strike point, where access is limited. Other components of the first wall include full toroidal inner and outer limiters for protection of the vessel walls and other components, and a set of three poloidal limiters for startup and protection of rf antennae Faraday shields. The limiter surfaces should see only radiative loads in the steady-state phase of the discharge. In the remainder of this Section we describe first the general features of the divertor and first wall components, then consider the likely operating point in terms of power and particle flux, and finally discuss helium ash exhaust and particle control.

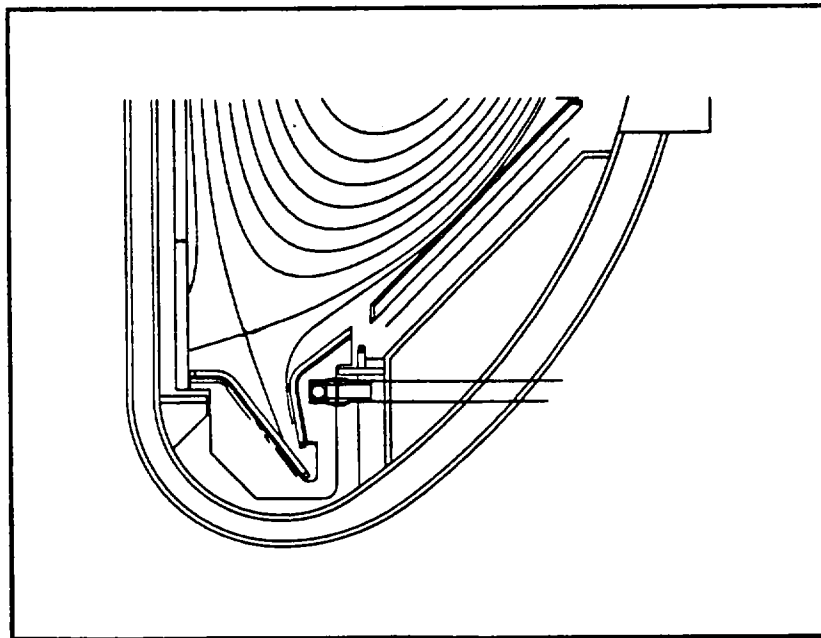


Fig. 1. Cross section of lower divertor region

The basic features of the proposed divertor are evident in Fig. 1. First, it has a deep Vee shape to help trap neutrals and reduce the electron temperature and sputtering at the target plate by allowing significant radial energy transport into the private flux region below the x-point. The distance between the x-point and the strike point along the outer divertor leg is 0.93m (nearly 2/3 the minor radius). Second, there is a relatively shallow angle of incidence between the magnetic flux surfaces and divertor surface (23°) to spread out the heat flux as much as possible. Third, the vertical target of the inner divertor uses minimal plasma volume for power handling, which is possible because of the large magnetic flux expansion and the greatly reduced power flow to the inner leg in double-null plasmas (10:1 out/in ratio of peak heat flux in present DN experiments). Fourth, the pumping ducts are closely coupled to the divertor plasma since they are situated opposite the strike point to best capture recycled neutrals and have a minimal cross sectional area facing the divertor plasma to reduce gas back flow.

The modest energy throughput of this device compared to its size (100 MW for R=5 m compared to 300+ MW for R=8 m in the EDA ITER or 40+ MW for R=3 m in JT-60U) allows for a divertor design compatible with standard high recycling, low temperature operation. The 120-sec pulse length will require water cooling during the discharge on all surfaces with power loading greater than 1 MW/m^2 . Most of the first wall components fall well below this limit, since they are heated only radiatively (0.2 MW/m^2 maximum steady load) except during the thermally transient start-up phase when the low power plasma is in contact with the outboard poloidal limiters. In the outer divertor leg, the expected peak heat flux of 6 MW/m^2 can be taken on actively-cooled, high thermal conductivity brazed macroblock graphite surfaces with swirl-tube cooling.

The short pulse length and low fusion power density of this tokamak mean that carbon-based plasma facing components should have adequate component lifetimes against plasma erosion and neutron damage. Carbon is an attractive material because of the extensive experience with it in existing tokamaks and because it is very tolerant of off-normal events such as disruptions. Expected neutron fluence is less than 0.1 dpA, so the thermal and mechanical properties of graphite should not be affected. With a peak particle flux at the outer strike point of 4×10^{23} ions/sec/m², the expected erosion rate at the operating temperature of 1000°C should be about 500-1000 Å/sec, or 0.5 cm per 1000 full power, full duration discharges. During disruptions, a peak thermal loading of about 2.4 MJ/m² may be expected, which is much less than that predicted for the EDA ITER. In-vessel tritium inventory will build up at 0.4 g/shot, which is compatible with a site limit of the order of 100 g using reasonable removal techniques.

The design requirements for the plasma facing components allow for either radiative divertor or radiative mantle operation. Gas puffing in the divertor modules will allow for increasing the local density of impurity or fuel ions to enhance radiative losses. The deep divertor configuration provides good isolation between the divertor and the core to help keep impurities entrained and provides plenty of distance for momentum loss via charge exchange. Adequate pumping should be available to help trap the injected impurity gas in the divertor region.

1.2.6.2 Expected Divertor and Scrape-off Layer Parameters

We expect that the divertor will operate normally in the high recycling regime with a peak heat flux at the outer target in the range of 6 MW/m². This is based on both numerical simulation of the 2-d scrape-off layer plasma using the UEDGE code and on simple extrapolations from present experiments based on

observed scaling. In terms of power density (either perpendicular to the separatrix at the midplane or normal to the target plates) this machine will operate in a regime similar to presently operating or proposed tokamaks, as shown in Table 1. Here, A_{div} is the wetted area on the divertor and P_{div} is the total power reaching all the target plates assuming a 40% total radiative loss. It is clear that a strongly radiating or detached divertor operating regime will not be required to meet the power handling requirements in this machine.

Table 1.

Comparison of power loading parameters for various tokamaks.

Machine (power)	JT-60U (40MW)	AUG (10 MW)	DIID-D (20 MW)	JET (40 MW)	TPX (18 MW)	PCAST (100MW)	ITER (300MW)
Shape	SN	SN	SN	SN	DN	DN	SN
$\frac{P_{in}}{V_p} \left(\frac{MW}{m^3} \right)$	0.46	0.8	1.0	0.48	1.5	0.25	0.15
$\frac{P_{in}}{A_p} \left(\frac{MW}{m^2} \right)$	0.25	0.23	0.4	0.27	0.30	0.25	0.27
$\frac{P_{div}}{A_{div}} \left(\frac{MW}{m^2} \right)$	6.5	3.5	7	7	4-6	5	20
Density	JT-60U	AUG	DIID-D	JET	TPX	PCAST	ITER
$n_e(10^{20}m^{-3})$	0.1-0.7		0.6-1.4	0.6	0.55	1.6	0.7-1.5

The peak divertor heat flux and target-plate erosion rate are the primary concerns for the divertor design, followed by impurity control and helium ash exhaust. The peak heat flux depends on the power balance, the magnetic flux expansion between the plasma midplane and divertor target, and the width of the scrape-off layer:

$$\hat{q}_d = \frac{P_{SOL}}{2\pi R \times 0.7 \lambda_{q,d}} \quad (1.)$$

where R is the major radius of the strike point, $\lambda_{q,d}$ the width of the heat flux profile on the target (taking into account the inclination of the target plate). and the factor of 0.7 represents the effect of diffusion into the private flux region inside the separatrix. As shown the width of the scrape-off layer is crucial to predicting the peak divertor heat flux.

In the most simple 2-point scrape-off layer models, the width of the heat flux profile at the midplane, λ_q , varies as either $(\chi_e / q_{sep})^{1/2}$ or $(\chi_e L_{||} / \sqrt{T_d})^{1/2}$, depending on whether the SOL parallel thermal conductivity or the plasma sheath at the target plate limits the parallel heat flux. Here q_{sep} is the average power density across the separatrix, χ_e is the electron radial thermal diffusivity, $L_{||}$ is the parallel connection length, and T_d is the electron temperature at the target plates. The radial transport coefficient χ_e may be assumed a constant, or to vary in a Bohm-like manner (T/B). The present edge physics database is unable to resolve this scaling conclusively and for the modest change in parameters going from present experiments to the PCAST machine, it does not much matter what is chosen (i.e., the uncertainty in the values is larger than the difference between the scaling relations). Applying this approach to the present concept results in a midplane scrape-off layer thickness for the heat flux, λ_q , of about 1–1.5 cm.

Using the scrape-off width from above, and typical assumptions for the radiative power balance and distribution of heat flux in double-null discharges, we arrive at a very simple estimate of 6 MW/m² for the peak divertor heat flux, as tabulated in Table 2. Here we have taken into account the expected Bremsstrahlung (25 MW) and line radiation (10%) losses in the core, and have assumed an up/down and in/out distribution of scrape-off layer power flow that is

consistent with the experimental database from ASDEX, PDX, and DIII-D double-null operation.

Table 2: Simple Estimate of Peak Divertor Heat Flux

P_{heat} (MW)	100
f_{rad,core} (line+Bremss)	0.35
f_{SOL}(up/down)	1:1.2
f_{SOL}(out/in)	4:1
P_{SOL}(down and out)	$100 \times (1-0.35) \times 0.55 \times 0.8 =$ 28.6
λ_{q} at midplane (m)	0.01
flux expansion/target angle	4:1 / 23°
f_{rad,div}	0.3
P_{div} (MW)	$(1-0.3) \times 28.6 = 20$
$\lambda_{q,d}$ at divertor (m)	0.094
R_{div} (m)	4.1
$q_{\max} = \frac{P_{\text{div}}}{2\pi L_{q,\text{div}}} \text{ (MW/m}^2\text{)}$	8.2
with correction for diffusion into private flux region (0.5 - 0.7) (MW/m²)	$0.7 \times 8.2 = 5.8$

A more complete (though not necessarily more reliable) prediction of the scrape-off layer and divertor conditions requires the application of a 2-d model for scrape-off layer plasma transport and neutral recycling in the divertor. We have used the UEDGE code to simulate the edge plasma for this machine and arrive at the predicted SOL thickness, and the heat and particle flux profiles along the outboard divertor target plate. The UEDGE code solves the energy and particle transport equations for the SOL plasma on a 2-d mesh derived from the reference MHD equilibrium, using boundary conditions (SOL input power and upstream plasma a density on the separatrix) appropriate for the particular problem and

relatively standard anomalous radial transport coefficients. Classical energy and particle transport along field lines is assumed, with heat flux limits applied if the collisionality drops too low due to high temperatures or low density in the SOL plasma. For these simulations, we used $\chi_e = 1.5 \text{ m}^2/\text{s}$, $\chi_i = 1.0 \text{ m}^2/\text{s}$, $D_{\perp} = 0.5 \text{ m}^2/\text{s}$, an upstream density of $3 \times 10^{19} \text{ m}^{-3}$ ($=0.2 \times \langle n_e \rangle$) and a power flow across the separatrix (24 MW) consistent with the power balance assumed for Table 2 (That is, we reduced the SOL power somewhat for the simulation since we did not allow for impurity radiation in the UEDGE simulation-only hydrogenic losses were included). Finally, a recycling coefficient of 0.99 was assumed at the target plates.

Generally, the UEDGE simulations show a cold ($T_e = 10\text{--}20 \text{ eV}$), dense ($3\text{--}5 \times 10^{20} \text{ m}^{-3}$) plasma at the divertor target, with modest plasma temperatures upstream at the midplane. Fig. 1 shows the outboard midplane profiles; the electron temperature at the separatrix is only about 150 eV and the profile 1/e width is just over 1 cm. The ion temperature and density profiles are broader. However, since the parallel thermal conductivity is largely governed by the electron temperature, the heat flux profile most closely follows the electron temperature. Therefore, the simple estimate used in Table 2 is a valid approximation. Indeed, the target plate heat flux profile and peak heat flux, Fig. 2, agree quite well with the more simple estimate. We also show the target plate plasma density and temperature profiles in Fig. 3.

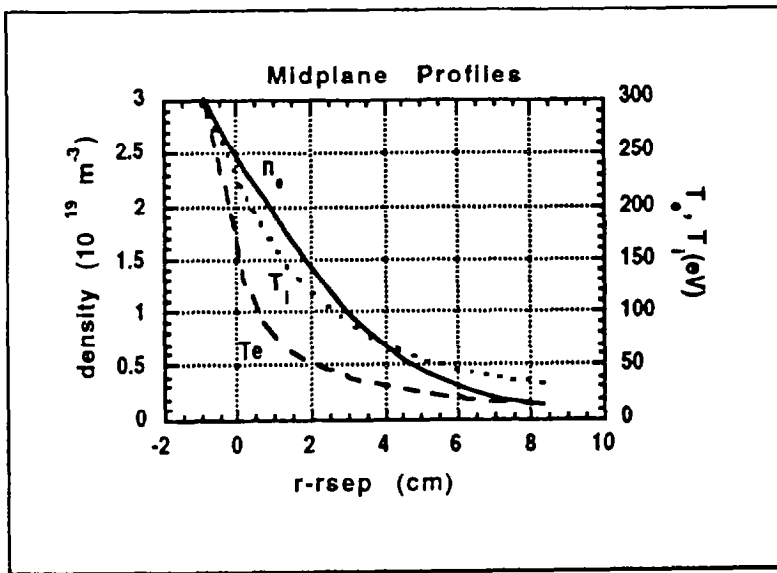


Fig. 1: Midplane density and temperature profiles based on UEDGE simulation # pcast8.

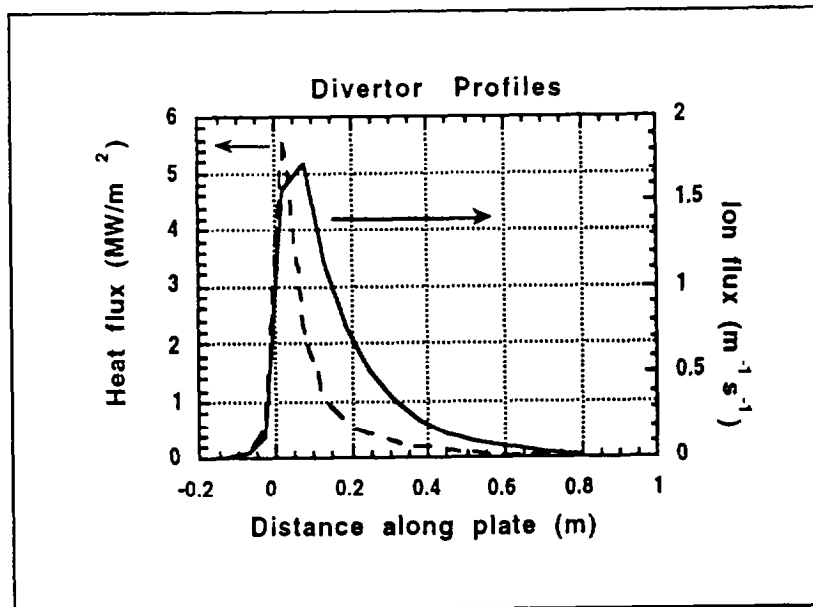


Fig. 2: Divertor heat and particle flux profiles from the UEDGE code.

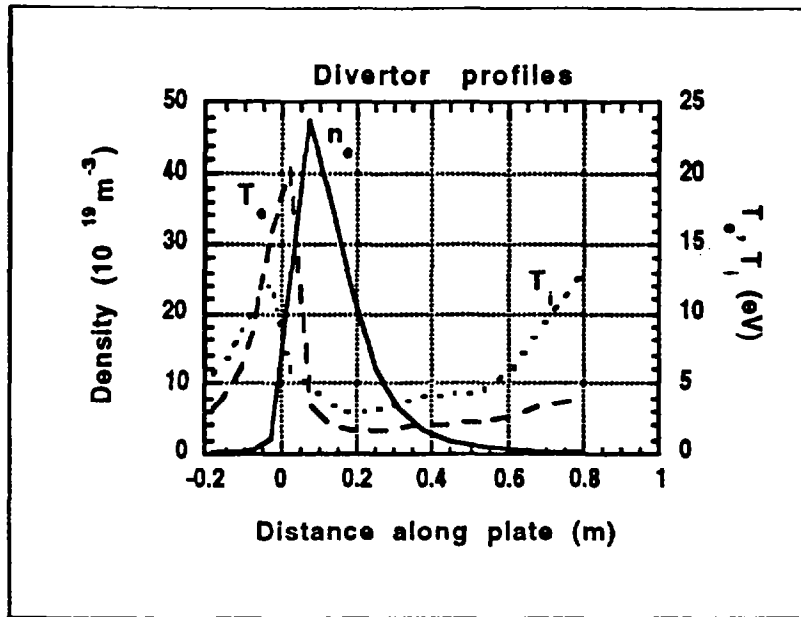


Fig. 3. Divertor density and temperature profiles from the UEDGE code.

In these simulations and simple estimates, we have not tried to enhance the radiative losses over those naturally expected to occur in a carbon-based machine. The addition of deuterium gas puffing in the divertor has been shown to be effective in reducing the peak divertor heat flux and target plate plasma temperature by increasing the divertor density and radiative losses there. We would expect the same to be feasible in this machine because the plasma temperatures and power densities are very similar to those in existing machines. Presently there is no solid experimental evidence that the detailed shape of the divertor structure plays a strong role in attaining such operating regimes, but we believe that the deep Vee design presented here provides adequate volume for radiating a significant fraction of the incoming energy and sufficient poloidal distance for trapping neutrals to maintain high divertor gas pressure.

1.2.6.3 Particle Control

Divertor pumping during each plasma pulse will be the primary method for particle control, though the relatively short pulse length will mean that a well-conditioned graphite wall will play an important role in the particle balance. Divertor pumping will be provided by 8 radial pumping ducts at the outer targets of both the upper and lower divertors. The total pumping speed will be 50 m³/sec at a 2 mTorr operating pressure (limited by the pumps, not the conductance), provided by turbopumps. Between shots, HeGDC can be applied as needed to recover from disruptions or from too much impurity puffing during radiative divertor experiments.

The divertor pumping system must provide adequate exhaust efficiency for density control and helium ash removal, yet still allow enough particle recycling in the divertor to keep the density high and electron temperature down. The required helium exhaust rate is 4Torr-l/sec based on high-Q driven operation with $P_{fus}=400\text{MW}$, and the pumping efficiency must be such that the core helium concentration can be maintained below 10%. Following the ITER Expert Group, we use a helium enrichment factor (pump duct helium concentration / core helium concentration) of 0.2. That is,

$$\frac{n_{\text{He,d}}}{n_{\text{He,d}} + 2n_{\text{D}_2,\text{d}}} / \frac{n_{\text{He,c}}}{n_{\text{e,c}}} = 0.2,$$

where the factor of 2 on the deuterium density takes into account the fact that the D/T gas is diatomic and He is not. Solving for the deuterium pressure above, and multiplying by the pumping speed to obtain throughput, we find that to exhaust the 4 Torr-l/sec of helium will require a D/T exhaust rate of ~100 Torr-l/sec at the stated enrichment factor. With a working pressure of 2 mTorr divertor pressure (also

typical of present experiments) a total effective divertor pumping speed of 50,000 l/sec is adequate. This is easily achievable given the planned size of the pumping ducts and speed of the external pumps.

Of course, an important issue for helium exhaust is the particle confinement time in the core plasma, which is somewhat independent of external inputs. Recent experiments are showing that high confinement plasmas do not preferentially confine helium compared to the fuel particles, and that exhaust rates are largely governed by the divertor pumping efficiency rather than core transport. We expect that this machine will be no different in this regard.

Particle control also involves fueling, which will be accomplished by pellet injection. The proposed neutral beam injection heating will provide a negligible particle source compared to that needed to sustain the plasma. If we assume that the global particle confinement time is about twice the energy confinement time, then about 100 Torr-l/sec of D/T fueling will be needed to sustain the plasma density at $1.6 \times 10^{20} \text{ m}^{-3}$. During the current ramp up, when the density is building and the tokamak walls are pumping gas efficiently, a maximum fueling rate of up to 300 Torr-l/sec will be needed at the end of the ramp ($dN/dt + N/\tau_p$ with a 30% fueling efficiency). Much of this can be obtained by simple gas puffing.

Radiative divertor operation may also require additional gas puffing in the divertor to help entrain impurities in the divertor region. At present, only very simple estimates of the additional gas flow exist and there is some healthy disagreement over them because experiments have not shown clearly that gas *flow* is the key for improving entrainment (as opposed to just raising the divertor density by gas puffing). If the additional gas flow needed is less than five times the fueling

rate needed to sustain the density, then adequate particle exhaust is possible given the number and size of the proposed pump ducts, though an increase in pump speed might be needed.

1.2.7. Physics Basis: Diagnostics

K. M. Young (PPPL)

Introduction

The diagnostic requirements for the PCAST device closely mirror those proposed for ITER. There is a stronger requirement for real-time control based on plasma parameters to provide capability for achieving optimum tokamak performance and ignition, but all the necessary diagnostic systems are included in the proposed set for ITER and the feedback implementation only involves additional computer hardware and speedier analysis. The ITER diagnostics at this point in the EDA are fully described in the ITER Diagnostic Design Description Document (WBS 5.5) and in Ref. [1]. In recent years, there have been enormous advances in core-plasma diagnostics and there is a very rapidly evolving field of divertor-plasma diagnostics. Hence the diagnostic plans for BPX are outdated. There are comprehensive descriptions of the TPX set of diagnostics, which meet the requirements for achieving advanced tokamak plasmas, in two reports of diagnostics review meetings among community experts, Ref. [2] and [3]. These two documents enhance the earlier TPX diagnostic descriptions Ref. [4,5].

The integration requirements of the diagnostics with the tokamak, the relatively high neutron fluxes and fluences and the scale of the device make the diagnostic implementation very similar to that being developed for ITER. The lower neutron source strength of the PCAST device is somewhat offset for the in-vessel diagnostic components by the absence of the blanket shielding. For most diagnostic components, noise background or performance changes created by high neutron fluxes have greater impact on the diagnostic implementation than permanent damage created by high fluence, so

diagnostic implementation on the PCAST device will not be significantly easier than for ITER.

Diagnostic Configuration

The categorization of diagnostics into three levels, as done by the ITER Joint Central Team (JCT) in conjunction with the ITER Diagnostic Expert Group, should be followed for the PCAST device (ITER Diagnostics Description Document). The categories are:

- i) those necessary for machine protection and plasma control;
- ii) those necessary for optimizing and evaluating the plasma performance;
- iii) those required for understanding important physical phenomena which may limit ITER performance.

Category (i) measurements are selected to assure safe operation of the tokamak and to provide the necessary control signals, in real-time, for operation of the tokamak. These measurements will required some redundancy and a very high level of reliability. The category (ii) measurements are necessary for the physics understanding of the plasma performance to allow optimization and to be able to push the performance to higher levels. Category (iii) provides a set of physics measurements aimed at providing information on the underlying physics which may limit the performance.

Table 1 duplicates the list of plasma measurements proposed for ITER. In the ITER Diagnostics Description Document there are also lists of the precision and resolution required of each of these measurements and a listing

of the diagnostic techniques which might be implemented to achieve these goals. It is essential that the measurement capability of categories (i) and (ii) should be provided before the tokamak becomes significantly activated so that necessary changes may be made relatively quickly. The PCAST plasma is sufficiently different in size, density and temperature from present-day plasmas that the physics issues of the measurements must be resolved early, as well as developing an understanding of the physics of the plasmas themselves. Table 2 lists the set of diagnostics proposed to be included in a start-up set of diagnostics which is intended to permit completion of the physics mission of the start-up phase of the device. This set is under review by the ITER Expert Groups at this time.

The implementation of a complex control system should be evaluated and a start was made for this for TPX. The proposed matrix of diagnostic and control interface is shown in Table 3. This list includes diagnostics, such as the Motional Stark effect diagnostic for measurement of the current density distribution, not included in the ITER category (i) set, or the ITER start-up set.

Table 1: Plasma Measurement Requirements

Category (i): Measurements for Machine Protection and Plasma Control

#	Plasma Parameter to be measured	Purpose
1	Plasma Current	Total current required for control
2	Plasma Position and Shape	Poloidal field feedback
3	Loop Voltage	I_i , plasma startup
4	Beta	Disruption avoidance
5	Total Radiated Power	Disruption avoidance
6	Plasma Line-averaged Density	Plasma operation, disruption avoidance
7	Total Neutron Flux and Emission Profile	Burn control, fueling control
8	Locked-modes	Disruption avoidance
9	$m=2$ MHD Modes, Sawteeth	Disruption avoidance
10	Plasma Rotation	Disruption avoidance, confinement optimization
11	nT/nD in Plasma Core	Fueling control
12	Impurity Species Monitor	Impurity control, wall protection
13	Z_{eff} (line-averaged)	Impurity control, He accumulation
14	ELMs, L/H Mode Indicators	H-mode realization, optimization control, divertor protection
15	Runaway Electrons	Runaway avoidance
16	Key Divertor Parameters	
	Divertor Plate Temperature*	Protection of divertor structure
	Divertor Radiated Power	Divertor operation
	Divertor Plate Ablation	Divertor plate erosion
	Ionization Front Position	Divertor optimization
	Divertor Gas Pressure*	Divertor operation
17	Edge Light & First Wall Temperature*	Startup, position and hot spot monitor (360° Coverage?)
18	Base Pressure*	Tokamak readiness
19	Gas Pressure in Duct*	Divertor functionality
20	In-vessel Inspection*	Inspect for internal damage
21	'Halo' Currents*	Monitor forces on in-vessel components
22	Toroidal Magnetic Field*	Cyclotron resonance position, q -value
	* Indicates a machine diagnostic	

Category (ii): Measurements for Performance Evaluation and Optimization

#	Plasma Parameter to be measured	Purpose
23	Electron Temperature Profile†	Profile control by aux. heating; transport
24	Electron Density Profile†	Transport, fueling optimization
25	q(r) profile†	Plasma stability, transport
26	Zeff profile†	Impurity transport
27	Fishbones, TAE Modes†	Burn optimization, beta limit indication
28	Ion Temperature Profile	Burn optimization and transport
29	Helium Density in Plasma Core	Burn optimization and transport
30	Confined Alpha-Particles (r)	Alpha particle transport, heating profile
31	Escaping Alphas	Performance evaluation
32	Impurity Density	Condition, high-Z use in radiative loss
33	Edge nT/nD, nH/nD	Fueling optimization, plasma dilution
34	Long-term Neutron Fluence	Calibration of neutron dets., blanket data
35	Impurity and D,T Influx in Divertor	Divertor optimization
36	ISat in Divertor†, ne, Te at target	Divertor optimization
37	Rad. Profiles (Core, X-pt./MARFE, Div.)	Divertor optimization
38	Heat Loading Profile in Divertor	Divertor optimization
39	Divertor Helium Density	Divertor optimization, He pumping physics
40	nT/nD, nH/nD in Divertor	Fueling optimization, plasma dilution
41	ne and Te in Divertor	Divertor optimization
42	Ion Temperature in Divertor	Divertor optimization
43	Divertor Plasma Flow	Divertor optimization
44	nH/nD in Plasma Core	Plasma dilution
45	ICRF Antenna Coupling	Heating optimization
	† Potential Category (i) measurement	

Category (iii): Additional Measurements for Physics Understanding

#	Plasma Parameter to be measured	Purpose
46	Pellet Penetration	Fueling optimization
47	Plasma Facing Material Erosion	Erosion physics
48	Density Fluctuations	Instabilities (e.g., TAE mode)
49	Edge Turbulence	Understanding of edge transport
50	MHD Activity in Plasma Core	Instability studies
51	Te Fluctuations	Transport understanding
52	E Field and E Fluctuations	Transport understanding
53	ICRF Physics Measurements	Wave-plasma interaction

Table 2. ITER Diagnostics Start-Up Set

Magnetic Diagnostics

- Ex-Blanket Magnetics
- In-Blanket Magnetics
- Divertor Magnetics
- Continuous Rogowski Coils
- Diamagnetic Loop

Neutron Diagnostics

- Radial Neutron Camera
- Vertical Neutron Camera
- Neutron Flux Monitors (Ex-Vessel)
- Lost Alpha Detectors

Optical/IR Systems

- Thomson Scattering (Core)
- Toroidal Interferometric/Polarimetric System

Bolometric System

- Bolometric Array For Main Plasma
- Bolometric Array For Divertor

Spectroscopic and NPA Systems

- H Alpha Spectroscopy
- Impurity Monitoring (Main Plasma)
- Impurity Monitoring (Divertor)
- Visible Continuum Array
- Soft X-Ray Array

Microwave Diagnostics

- ECE Diagnostics for Main Plasma
- Reflectometers for Main Plasma

Plasma-Facing Components and Operational Diagnostics

- IR Cameras (Divertor)
- Thermocouples
- Pressure Gauges
- Residual Gas Analyzers
- Hard X-Ray Monitor
- Visible/IR TV (Main Plasma)
- Langmuir Probes/ Tile Shunts

Table 3. Proposed TPX Diagnostic/Control Matrix

CONTROL COMPONENT	DIAGNOSTIC	MEASURED PARAMETER	CONTROLLED PARAMETER	FEED BACK ELEMENT	ACTUATOR
Fast Plasma Position Control	Rogowski Coils	Plasma current	Radial position, Vertical position	IC Coil Current	IC Coil Power System
	Poloidal Magnetic Flux Loops/Voltage Loops	Poloidal flux			
	Poloidal Magnetic Field Probes, Discrete Br/BZ Coils	Magnetic field			
Plasma shape & equilibrium control	Rogowski Coils	Plasma current	Plasma-antenna gap, Plasma-passive stabilizer gap, Plasma-limiter gap, Outboard strike points, Inboard strike points, Plasma current	PF coil current	PF coil power system
		Passive stabilizer currents			
	Poloidal Magnetic Flux Loops/Voltage Loops	Poloidal flux			
	Diamagnetic Loop	Toroidal flux			
	Thomson Scattering	Electron density			
		Electron temperature			
Poloidal Magnetic Field Probes, discrete Br/BZ Coils	Magnetic field				
Kinetic profile control	Thomson Scattering	Electron density	Beta, Beta poloidal, Pressure, Temperature, Density	FW,LH,NB	FW source and antenna LH source and antenna, Neutral beams
		Electron temperature			
	Millimeter wave interferometer	Plasma density			
	Charge exchange spectroscopy	Rotational velocity, Ion temperature			
	Visible bremsstrahlung	Impurity constant			
Current profile control	Rogowski coils	Plasma current	Inductance, Current density, Quality factor,	FW,LH,NB	FW source and antenna LH source and antenna, Neutral beams
	Poloidal Magnetic Flux Loops/Voltage Loops	Poloidal flux			
	Diamagnetic Loop	Toroidal flux			
	Saddle loops	Loop voltage			
	Motional Stark effect	Current distribution			
		Thomson Scattering	Electron density		
	Electron temperature				
	Poloidal Magnetic Field Probes, discrete Br/BZ Coils	Magnetic field			
	Millimeter wave interferometer	Plasma density			
	Infrared TV	Surface temperature			

Table 3. Proposed TPX Diagnostic/Control Matrix (continued)

Divertor Control	Visible H-alpha TV	Position, detachment	Throat density, Throat temperature, SOL density, SOL temperature Plate temperature	Cryopump valves, Injection valves	Vacuum pumping, Gas injection
	Fast pressure gauges	Gas flow, pressure			
	Divertor bolometer arrays	Position, power loss			
	H-alpha monitors	H-neutral density			
	Edge plasma probes	SOL density, temp.			

Access and Interface Issues

The access to this device is very good for diagnostics. Many large horizontal ports are available for diagnostics, but the diagnostic access must not compromise the integrity of the device or its shielding. Figure 4 of Section 1.1 shows the first attempt to allocate diagnostics to the ports on the tokamak. Within each of the access ports an equivalent thickness of shielding to that of the vacuum vessel wall will have to be provided to prevent the radial streaming of neutrons outward into the cryostat volume surrounding the device. Also, as in ITER, the diagnostic penetrations in the shield wall must be created with labyrinths and compensatory shielding so as to limit the flux and fluence in the surrounding space to design levels. These requirements lead one to consider the mounting of the diagnostic components in modules, the concept developed during the ITER EDA study of "Generic Access". The first module would mount into the vacuum vessel port and would contain mirrors, collimators, other components and shielding labyrinths mounted off a large vacuum flange containing the relevant windows and feedthroughs. This module will be handled as one unit by the remote-handling equipment. A second module will provide alignment structures, necessary diagnostic components such as periscopes or optical fibers and the shield and secondary vacuum interface. It can be slotted into the shield wall by the remote-

handling equipment. As much as possible will be done to keep neutron/gamma-sensitive components and detectors beyond this shield wall and, where possible, in the diagnostic hall. The horizontal ports will be largely filled by diagnostic components and shielding while the top and bottom vacuum-pumping access ports will necessarily be kept lightly loaded with diagnostic components so as not to compromise the pumping capability.

This modular concept will be followed throughout except when straight-lines of sight are necessary for the quality of the measurement. Neutron camera arrays for a-source identification and ion temperature measurement may have to be contained in shielding blocks between the cryostat and the shield wall. (Their access, with the relatively thin first wall, is potentially very much better than for ITER.) These blocks will be large and special arrangements for access at the shield wall will be required. The small access window on the top of the tokamak, while mostly being useful for service supplies and waveguides, also provides collimated access for a vertical neutron camera, whose detailed interaction with the cryostat dome needs to be developed.

There are two kinds of horizontal access port. There are triad ports providing access ducts for two neutral beams and a large clear access port between them. The other ports are large rectangular ducts with excellent clear access except for those neighboring a neutral beam port and in the shadow of a neutral beam in place. These ports can be used for diagnostics but with the slight constraints that the diagnostic components (and shielding) outside the shield wall cannot be too bulky and no component inside the shield wall can be changed or maintained without removing part of the beamline.

Until some design work, involving the integration of systems together, has been done it will not be possible to determine the full needs for diagnostic space. There is considerable ITER design effort going toward determining whether many spectroscopic techniques can share windows and mirrors, and whether microwave techniques can share horns and waveguide without excessive compromise of the measurement quality. The results of these studies will be immediately applicable to the PCAST device.

R&D Requirements for Diagnostics

There is an aggressive ITER R&D program on the radiation effects of diagnostic components. Studies in the U.S. are looking at radiation-induced conductivity and radiation-induced electrical degradation for ceramics and mineral-insulated cables for use in diagnostics inside the vacuum vessel. Specific tests are also being made of a prototype Mirnov coil. These tests should be adequate for the initial design work for the diagnostics for the PCAST device and no further effort should be required, until specific components have been chosen, at which point validation of the choice will be required.

There will be a need for development of new techniques, or major enhancements of established techniques. These components will have to be developed and tested on an operational tokamak. There is such a program for ITER, with an undetermined need for further work during the Construction Phase.

References

- [1] A.E. Costley et al. "Requirements for ITER Diagnostics", Proceedings of the International Workshop on ITER Diagnostics (Varenna, Italy, Sept. 1995).
- [2] "Presentations at the TPX Diagnostics Configuration Review" (TPX Document # 62- 941028-PPPL/SMedley-01).
- [3] "Presentations at the TPX Divertor Diagnostics Workshop" (TPX Document # 62- 950522-PPPL-SMedley-04).
- [4] S.S. Medley, "Tokamak Physics Experiment Diagnostic Plans", Rev. Sci. Inst., **66**, 287 (1995).
- [5] S.S. Medley et al. "Diagnostic Design Description Document", TPX Document # 62-930319-PPPL/SMedley-01.